Estimating

Thermal Radiation Fields

from

3D Flame Reconstruction

A thesis
submitted in partial fulfilment
of the requirements for the Degree of
Master of Applied Computing

at

Lincoln University

by

Paul Mason

Lincoln University

2003

Abstract of a thesis submitted in partial fulfilment of the
requirements for the Degree of Master of Applied Computing

Estimating Thermal Radiation Fields from 3D Flame Reconstruction

by Paul Mason

Designing fire safety into a building requires a designer to think through issues that include fire ignition, growth and spread. The dominant mechanism of spread is radiative heat transfer from flames. Therefore, in order to understand how the fire might develop it is necessary to determine the thermal radiation field surrounding a fire. This requires being able to calculate the heat flux for any target location. The accuracy of heat flux calculations depends on the accuracy of its components, which are the flame's emissive power and the shape factor between the flame's surface and the target. The essential requirements for determining shape factor are to define the geometry of the flame surface, and to have a method for obtaining the shape factor for that geometry. Previous methods for predicting heat flux have modelled the flame as simple regular geometries because methods for calculating shape factors for other geometries were either too complex and error prone, or did not exist. Hankinson [7] overcame this limitation with a method for calculating shape factors that can be applied to multiple, irregular flame geometries. However, these geometries must be defined in order to apply the method. Therefore, until now Hankinson's method has been restricted in its use by an inability to define multiple, irregular geometries.

In this study we focus on accurately determining the shape factor by presenting a method to define flame geometry using image-processing techniques. The images of the fire are recorded using multiple cameras and the flame is reconstructed in 3D. Once the surface of the flame has been defined it is possible to calculate the shape factor at a given target. Then, using the shape factor and a suitable estimate for the emissive power of the flame, the heat flux at the target can be determined. Repeating this process for multiple targets builds a thermal radiation field. This can then be used to find out which adjacent objects are threatened and which are safe.

An introduction to some of the relevant aspects of radiative heat transfer is given, followed by a detailed description of the method. The method is first applied to a controlled flame, represented by a propane diffusion burner with an electronically regulated fuel supply. Next, the method is applied to an uncontrolled flame, represented by a burning item of upholstered furniture. For this experiment, the recorded heat flux data was graphed against calculated shape factors and the line of best fit was obtained. The slope of the line represents the emissive power of the flame, and values for Pearson's linear correlation coefficient were found to range between 0.955 and 0.998.

Keywords: Fire engineering, thermal radiation field, heat flux, emissive power, shape factor, image processing, flame geometry, 3D reconstruction, diffusion burner, upholstered furniture, fires.

Contents

List of Tables

List of Figures

Chapter 1

Introduction

1.1 Context and Motivation

1.1.1 Fire engineering

The study is carried out in collaboration with the Fire Engineering section of the Civil Engineering Department at Canterbury University. Fire Engineering is the art and science of designing buildings that allow people to escape before being overcome by the effects of fire [24]. It relies on the principles of fire science, human behaviour and risk management. In modern times the emphasis on fire control has focused on understanding and predicting the growth and spread of fires. Designing fire safety into a building requires a designer to think through issues that include:

- Fire ignition, spread and growth – where spread refers to flame velocity over a burning object, and growth refers to the development of a fire in a room.
- How the fire might develop.
- How the building materials will respond to the fire.

1.1.2 Quantifying heat transfer

Heat energy is transferred by convection, conduction and radiation. Since radiation is the dominant mechanism of spread for a fire with diameter greater than 200mm [10],

this work considers only radiated heat energy. Therefore, when *heat flux* is mentioned during this study, we are referring to only *radiative heat flux.*

Heat flux is a measure of the rate at which heat energy flows into or out of a surface. It is expressed as the amount of energy flowing through unit area in unit time. Heat flux is a vector quantity and has units of watts per square metre (W/m^2)[1]. The point at which the heat flux is calculated or measured is referred to as a target. A target has a position, an orientation, and an area. The magnitude of heat flux at a target is the intensity of the *thermal radiation field* at that point.

Another quantity that is important to the prediction of the spread of the fire is the *heat release rate* (HRR). The heat release rate is a measure of the actual 'size' of the fire and usually has units of kilowatts (kW) or megawatts (MW).

1.1.3 The threat of upholstered furniture fires

Recent studies at the University of Canterbury have focused on upholstered furniture fires, since studies have identified them to be the most deadly [43]. Some furniture that uses foam cushions can burn very rapidly. A small flame in upholstered furniture can turn into a disastrous fire in only a few minutes. There are very few other items in the home that have the potential to cause such severe damage so quickly. A burning armchair could have a heat release rate of 1MW. A burning couch could have a heat release rate two or three times as high as an armchair. In these situations adjacent objects can ignite quickly and it is not surprising that fires heat up rooms so quickly and cause so much damage. Radiation from flames also causes issues for occupants exiting burning buildings since most people have to move past a flame.

[1] Although, the quantities encountered in most applications can usually be expressed more simply as kilowatts per square metre (kW/m^2).

1.2 Purpose of this Study

1.2.1 Aim

As a result of our collaboration with the University of Canterbury, this study shares their focus on the unique threat presented by upholstered furniture fires. Understanding the growth and spread of a fire requires determining the thermal radiation field that surrounds the fire, since this is the dominant mechanism of spread. The thermal radiation field can be quantified by being able to determine the heat flux at any location surrounding the fire. Therefore, the purpose of this study is to develop a model that enables us to predict the heat flux at any location. Having defined the thermal radiation field, it can be used to help understand how a fire spreads from one object to another in a room.

1.2.2 Method

The model for predicting heat flux is derived from video of the fire recorded by multiple cameras. Frames from the videos are processed using techniques, based on image calibration, that derive quantitative information. An underlying motivation for this approach is to develop video as a tool for analysing fires.

1.3 Background

1.3.1 Compartment fires

Fire-tight compartments are separated from adjacent spaces and each other by fire resistant elements of construction [21]. They are designed to contain an outbreak of fire or to guard against an external fire attack. An upholstered furniture fire in a room can be considered as a compartment fire. Compartment fires produce a zone of hot gas in the upper layer and raise the temperature of all elements in the compartment including the walls, floor and ceiling. These heated elements radiate energy back to the fire, which can increase the temperature of the flame [21]. Closed doors and windows may restrict the flow of oxygen to the fire and also limit the escape of products of combustion.

1.3.2 Couch composition

The spread of a fire depends on the combustion characteristics of the burning object. These characteristics depend largely on the materials used in the object's construction (see Figure 1-1). Often the composition of a couch is not known. Although the foam may be polyurethane[2], the additives are generally unknown. Hence, when making assumptions about the combustion characteristics of a piece of upholstered furniture, it is necessary to adopt a 'consistent level of crudeness' [4].

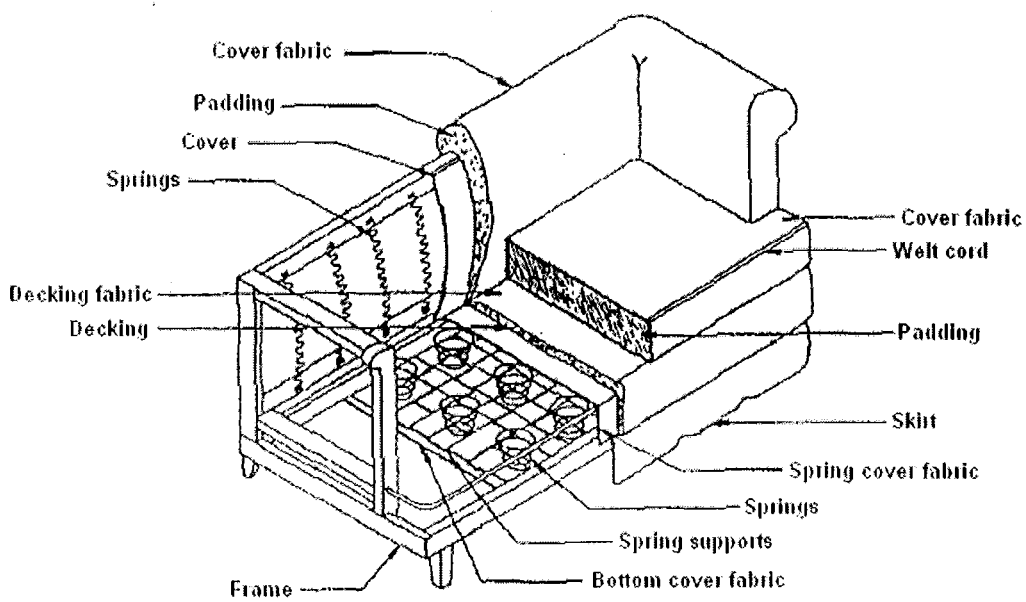

Figure 1-1: Construction details of a typical couch.

1.3.3 Pool fires

A pool fire is a flame over a puddle of liquid fuel. After ignition the combustion of the fuel vapour supplies the energy to vaporize more fuel. Heat flux calculations for pool fires typically include variables that refer to the diameter of the fire and the distance from the centre of the pool. The assumption is that a pool fire is circular or, if it is not circular, has a length to width ratio of approximately one. Heskestad [8] showed that the equivalent diameter for a non-circular pool can be found, provided the ratio of length to width is approximately one, using

[2] The wooden frame is ignored because it poses little threat compared to the polyurethane foam.

$$D = \sqrt{\frac{4A}{\pi}} \tag{1-1}$$

where

A = the surface area of the non-circular pool.

1.3.4 Typical couch burn

The burning process is a continuous chemical reaction between fuel particles and oxygen. The fuel particles are released as heat breaks the bonds in the burning material. The fuel vaporizes and it is the gas that burns. Heat is essential to the burning process: if fresh fuel is not heated, then a fire cannot spread.

A typical couch fire has two phases (see Figure 1-2). In the first phase the flame spreads to engulf the entire couch. The second phase exhibits pool fire characteristics as the synthetic materials melt and drip down to form a burning pool on the floor beneath the couch. Much of this pool comes from the foam that forms the back and the seat of the couch. The size of the flame and the heat release rate reach a peak during each phase and are often significantly smaller between phases.

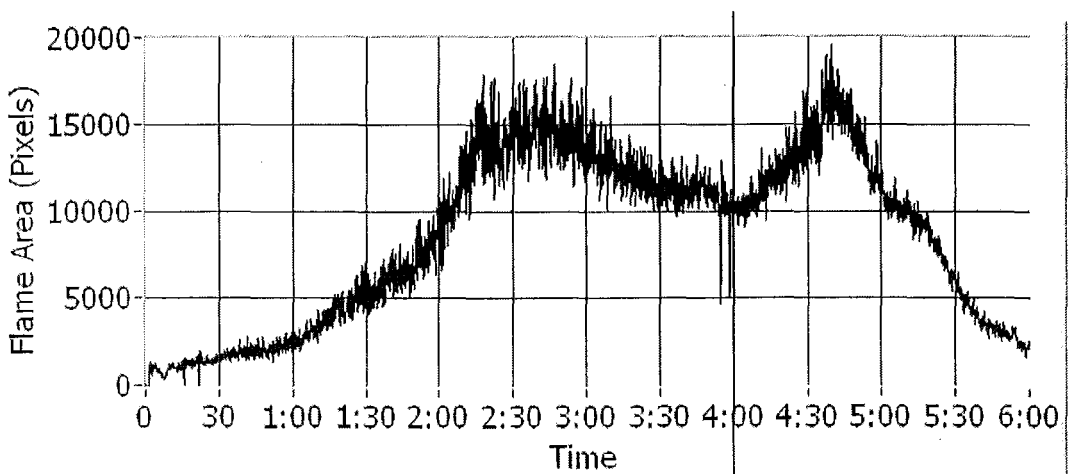

(a) Phase I (b) Phase II

Figure 1-2: Illustrating the two phases of a couch fire using flame area.

1.4 Thermal Radiation

1.4.1 Radiative heat flux

The emissive power E of a non-black body with emissivity ε is dependent on the temperature of that body, according to the Stefan-Boltzmann law [6]:

$$E = \varepsilon\sigma T^4, \tag{1-2}$$

where

- E is the power (in watts) radiated from $1m^2$ of any surface,
- ε is emissivity – defined in the following section *1.4.2*,
- σ is the Stefan-Boltzmann constant, 5.67×10^{-8} [$W/(m^2 \cdot K^4)$]
- T is the temperature in degrees Kelvin [°K].

Equation (1-2) gives the heat energy radiated from one square metre of a body at a temperature T °K in one second. The main radiating constituents in hydrocarbon flames are soot, water vapour and carbon dioxide [42]. Soot emits in a continuous spectrum in the visible and infrared regions, while water vapour and carbon dioxide do not emit visible radiation. Markstein [35] showed that the radiation from non-visible gases represents less than 10 percent of the mean radiation from a visible fire.

1.4.2 Emissivity

A blackbody is a perfect radiator, however many objects are not. Emissivity ε is the property of an object that describes how well it radiates compared to a blackbody [42]. For a blackbody the emissivity $\varepsilon = 1$, otherwise $\varepsilon < 1$.

A flame absorbs, emits and scatters radiation. Since soot is the dominant radiating product of combustion, determining the emission characteristics of a flame requires knowing the concentration and distribution of soot, and its radiative properties. Soot distribution is too complicated to determine from basic principles and its radiative

properties are only approximately known, so some empirical knowledge of the flame is required to establish its properties and emission [42].

1.4.3 Transmissivity

Transmissivity τ depends upon the atmospheric conditions and the mean path length from the target to the flame surface [7]. It describes the fraction of radiation leaving the flame that passes through the intervening atmosphere to arrive at the target. Losses in transmitted radiation may be due to reflection, scattering and absorption [42].

1.4.4 Shape Factor

The total energy referred to in equation (1-2) is radiated in all directions, so a target of finite size can receive only a fraction of that energy. The fraction of radiation leaving one surface that strikes another surface directly is defined as the *shape factor, F*. Its value lies between zero and one, and it is used to take into account the relative position and geometry of the source and the receiving target.

The shape factor is also referred to as the *configuration* factor, *view* factor, or *form* factor and has its roots in the work of Hottel and Sarofim [9]. Our key reference for this work has been *Thermal Radiation Heat Transfer* by Siegel and Howell [42].

Adding transmissivity and shape factor to the Stefan-Boltzmann law provides an equation suitable for describing radiant heat transfer for our purposes.

$$Q' = \varepsilon\sigma\ T^4 F\,\tau \tag{1-3}$$

where Q' is the radiation received per unit area of the target in unit time.

1.5 Limitations

Although, upholstered furniture fires invariably occur in rooms of buildings and can be considered as compartment fires, this study does not consider the influence of the compartment. Therefore, the heat flux calculated at target locations is considered to be entirely due to radiation arriving directly from the burning item of furniture. Radiation

from other sources that are characteristic of compartment fires, such as the hot gas layer and the walls, are not included.

There are regions above the flame where the total heat flux has a large convective component [4]. Therefore, since we are considering only radiative heat flux, caution should be exercised when interpreting values obtained in this region.

Chapter 2

Literature Review

Existing research into turbulent diffusion flames has produced methods for estimating thermal radiation to targets surrounding pool fires. The goal of existing methods is usually to calculate safe separation distances between fire sources and potential targets that would be damaged or adversely affected by radiation from the fire. All methods are based to varying degrees on empirical data rather than being developed from basic principles. The simplest methods require inputs such as pool diameter and distance from the centre of the pool. Methods that produce better results are generally more complex. Complex methods rely on determining the radiative properties of the flame and the size and shape of the flame. The accuracy of heat flux predictions therefore depends on the accuracy with which these two quantities can be determined. Literature has been selected for review if it addresses either of these issues.

2.1 Methods for Estimating Heat Flux from Pool Fires

For reasons discussed in Chapter1, an upholstered furniture fire may not always resemble a pool fire. However, since research involving pool fires accounts for nearly all of the most closely related work, it is included to provide a suitable background for subsequent work.

The four methods presented here are included in the SFPE Engineering Guide, *Assessing Flame Radiation to External Targets from Pool Fires* [41]. All methods are

based on data from experiments involving a wide range of fuels and pool sizes. Although this may reduce the correlation between derived estimates and recorded data, it makes the results more generally applicable. A safety factor of two is recommended in all cases. Using the safety factor allows estimates to over-predict the recorded data in nearly all cases. The safety factor should not be used if a realistic estimate of the heat flux at a target is required. First, two simple methods are summarised. They are the Shokri and Beyler Correlation [41] and the Point Source Model [41]. Following these is a more detailed method by Shokri and Beyler [41], and a method by Mudan and Croce [41].

2.1.1 Shokri and Beyler Correlation [41]

The incident heat flux for a vertical target at ground level is given by

$$\dot{q}'' = 15.4\left(\frac{L}{D}\right)^{-1.59} \quad [\mathrm{kW/m^2}] \tag{2-1}$$

where

D = the diameter of the pool fire [m]

L = the distance from the centre of the pool fire to the target [m]

Limitations

This method acknowledges that the maximum heat flux will be recorded at a target height that is half the flame height. Therefore, at heights above the ground, it is expected that the heat flux given by the equation will be exceeded.

2.1.2 Point Source Model [41]

The Point Source Model provides a simple relationship that varies as the inverse square of the distance.

$$\dot{q}'' = \frac{\dot{Q}_r \cos\theta}{4\pi R^2} \quad [\mathrm{kW/m^2}] \tag{2-2}$$

where

$\dot{Q}_r$ = Total radiative output of the fire [kW],

θ = Angle between the normal to the target and the line of sight from the target to the point source location,

R = the distance from the point source to the target [m].

This requires the total radiative output of the fire and the location of the point source to be known. The total radiative output is given by multiplying the total heat release rate by the radiative fraction, χ_r. Based on experimental data from a variety of fuel types the authors derive the following linear relation that gives the radiative fraction as a function of diameter

$$\dot{Q}_r = \chi_r \dot{Q} = (0.21 - 0.0034 D)\dot{Q} \qquad \text{[kW]} \qquad (2\text{-}3)$$

where

D = the diameter of the pool.

The maximum heat release rate of the fire, $\dot{Q}$, is given by

$$\dot{Q} = \dot{m}''_{\infty} \Delta H_c A, \qquad (2\text{-}4)$$

where

$\dot{m}''_{\infty}$ = Mass volatisation rate per unit area [kg/m^2 sec],

ΔH_c = Heat of combustion [kJ/kg],

A = Pool fire area [m^2].

The height of the flame is approximated by the Heskestad correlation [18]

$$H = 0.23 \dot{Q}^{0.4} - 1.02 D \quad \text{[m]} \qquad (2\text{-}5)$$

Limitations

The data upon which the point source model was based consisted mainly of heat fluxes below 5 kW/m^2, so it should not be applied to heat fluxes greater than that. The height of the target is valid between ground and the height of the flame.

2.1.3 Shokri and Beyler [41]

The pool fire flame is assumed to be a right circular cylinder, a black body, and a homogeneous radiator with an average emissive power. This method uses the form

$$\dot{q}'' = E\,F \quad \left[\mathrm{kW/m^2}\right], \tag{2-6}$$

where

E = the emissive power of the flame.

F = the shape factor between the target and the flame.

The emissive power, E, is based on published pool fire radiation data and is given by

$$E = 58 \times 10^{-0.00823\,D} \quad [\mathrm{kW/m^2}] \tag{2-7}$$

The shape factor is found using the following equations for a plane element to a right circular cylinder of finite length and radius. Examples of how to derive this type of equation are given in Siegel and Howell [42].

For a vertical target use

$$F_H = \frac{\left(B - \frac{1}{S}\right)}{\pi\sqrt{B^2 - 1}} \tan^{-1}\sqrt{\frac{(B+1)(S-1)}{(B-1)(S+1)}} - \frac{\left(A - \frac{1}{S}\right)}{\pi\sqrt{A^2 - 1}} \tan^{-1}\sqrt{\frac{(A+1)(S-1)}{(A-1)(S+1)}} \tag{2-8}$$

And for a horizontal target

$$F_V = \frac{1}{\pi\,S} \tan^{-1}\left(\frac{h}{\sqrt{S^2 - 1}}\right) - \frac{h}{\pi\,S} \tan^{-1}\sqrt{\frac{(S-1)}{(S+1)}} + \frac{Ah}{\pi\,S\sqrt{A^2 - 1}} \tan^{-1}\sqrt{\frac{(A+1)(S-1)}{(A-1)(S+1)}} \tag{2-9}$$

where

$$A = \frac{h^2 + S^2 + 1}{2S}, \quad B = \frac{1 + S^2}{2S} \tag{2-10}$$

$$S = \frac{2L}{D}, \quad h = \frac{2H}{D} \tag{2-11}$$

and

L = the distance between the centre of the cylinder and the target [m],

H = the height of the cylinder [m], found using Heskestad's correlation [18],

D = the diameter of the cylinder [m].

These equations for shape factor are valid for a target where a line from the centre of the target to the cylinder axis is perpendicular to the cylinder axis and passes through an end of the cylinder (see Figure 2-1). Therefore, if the target lies between the ground and the height of the flame, two cylinders must be used. One cylinder represents the flame above the target and the other cylinder represents the flame below the target. The result is obtained by summing the shape factors for each cylinder.

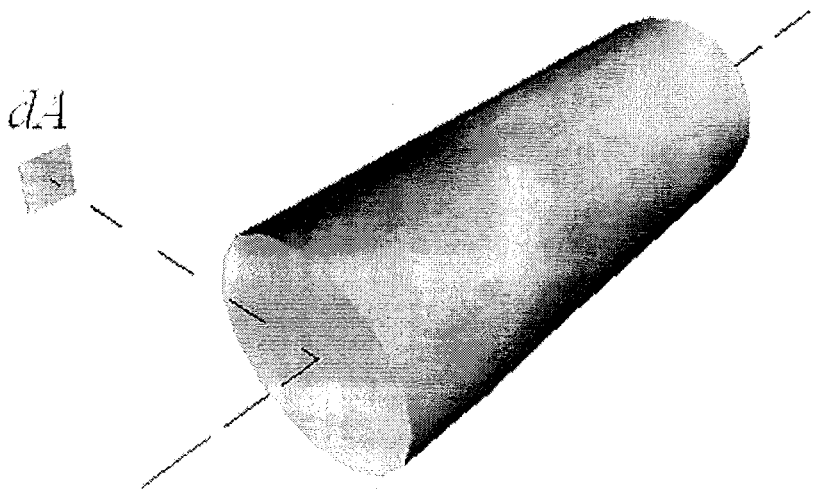

Figure 2-1: Location of target relative to the cylinder.

This method also introduces the idea of *maximum* shape factor as the vector sum of the horizontal and vertical components

$$F_{\max} = \sqrt{F_H^2 + F_V^2} \tag{2-12}$$

Shokri and Beyler [41] observed that the major uncertainty is in the definition of the emissive power and not in the shape factor model. This suggests that, for a pool fire, the cylinder model predicts shape factors well.

Limitations

The method is valid for targets between the ground and the height of the flame. Targets are restricted to two orientations, horizontal or vertical. The right cylinder of circular cross section cannot be tilted to model the effects of wind. Pool diameters range from 1 to 50m, and values of L/D were limited to the range 0.7 to 15. Using the recommended

safety factor of 2, this method over predicted almost all the recorded data for heat fluxes greater than 5 kW/m^2. This was not so for heat fluxes less than 5 kW/m^2, so it is recommended for use with heat fluxes greater than that.

2.1.4 Mudan and Croce [41]

Mudan and Croce add a correction τ to equation (2-6) to account for absorption of radiation by the atmosphere. When absorption is negligible, the transmissivity of the intervening atmosphere $\tau = 1$.

$$\dot{q}'' = E F \tau \qquad [\text{kW/m}^2] \tag{2-13}$$

In this method, the emissive power of the flame is adjusted using the extinction coefficient s and the pool diameter D. The effective emissive power is given by

$$E = E_{\max} e^{(-sD)} + E_s \left(1 - e^{(-sD)}\right) \quad [\text{kW/m}^2] \tag{2-14}$$

where

$E_{\max}$ = equivalent black body emissive power, 140 kW/m^2,

s = extinction coefficient, 0.12 m^{-1},

D = equivalent pool diameter [m],

E_s = emissive power of smoke, 20 kW/m^2.

The equations used for calculating the shape factor allow the cylinder to be inclined to model wind-blown flames. When wind is present, the equations include the angle of tilt of the wind-blown flame. In the case of no wind, these equations reduce to those for a right circular cylinder as used in the previous method. The distance from the centre of the pool to the target at ground level is used. Instead of using Heskestad's equation, height estimates are based on Thomas' [44] correlation of the mean visible height of turbulent diffusion flames for a circular flame in the absence of wind.

$$\frac{H}{D} = 42 \left(\frac{\dot{m}''_\infty}{\rho_a \sqrt{gD}} \right)^{0.61} \tag{2-15}$$

where

D = the pool diameter [m],

$\dot{m}''_{\infty}$ = the mass burning rate per unit pool area [kg/m^2 sec],

ρ_a = the ambient air density [kg/m^3],

g = gravitational acceleration, 9.8 m/sec^2.

For wind-blown flames another of Thomas' correlations is used to find flame length

$$\frac{H}{D} = 55\left(\frac{\dot{m}''}{\rho_a\sqrt{gD}}\right)^{0.67}(u^*)^{-0.21} \tag{2-16}$$

where

u^* = wind velocity given by

$$u^* = \frac{u_w}{\left(\frac{g\,\dot{m}''_{\infty}\,D}{\rho_v}\right)^{1/3}} \tag{2-17}$$

where

u_w = wind speed [m/sec],

ρ_v = fuel vapour density [kg/m^3].

The angle of tilt is given by Thomas' correlation for flame tilt based on data from two dimensional wood crib fires.

$$\cos\theta = 0.7\left[\frac{u_w}{(g\,\dot{m}''_{\infty}\,D/\rho_a)^{1/3}}\right]^{-0.49} \tag{2-18}$$

where

θ = angle of tilt.

Limitations

This method assumes the fire is circular or nearly circular.

2.1.5 Summary

The Shokri and Beyler Correlation is only valid for targets at ground level. There is little difference between the performance of the Point Source Model and the Mudan and Croce model for heat flux values less than 5 kW/m^2, so the point source model is generally preferred for its simplicity. The second Shokri and Beyler method is preferred for heat fluxes above 5 kW/m^2. With the exception of the Point Source Model, all methods impose restrictions on the target position and orientation. The correlation between estimates and recorded data is not very good with any of the methods, hence the recommended safety factor of 2. The best correlation coefficient reported in [41] was 0.53 for the Mudan and Croce method when it is limited to heat fluxes less than 5 kW/m^2. In all cases the pools were assumed to be circular or near circular. The geometry of the flame was modelled simply as a point, a right circular cylinder, or an inclined circular cylinder.

2.2 Extending Shape Factor Calculations to Irregular Flame Geometries

2.2.1 Hankinson's Work

Hankinson [7] developed a method that allows the shape factor to be calculated for any flame shape. When calculating the heat flux at some location surrounding a fire, he states that four major steps are involved:

1. Specification of the thermal radiation properties of the flame.
2. Determination of the transmissivity of the intervening atmosphere.
3. Specification of the size and shape of the flame.
4. Calculation of the shape factor.

Hankinson [7] observes that regular geometrical shapes have been used to approximate flame shapes in previous studies. He suggests that the range of geometries imposed can depend on techniques available for calculating the shape factor. The contour integral method [42], for example, can become extremely complex for irregular flame geometries. Contour integration applies Stoke's theorem to reduce the multiple integration over a surface to a single integration around the boundary of an area. Hankinson [7] cites area integral methods including a technique developed by Rein et

al. [39], where the surface of a cylinder contained within the field-of-view of a target is divided into small parallelograms. He notes that inaccuracies using this method increase as the flame tilt increases and when targets are located crosswind of the fire.

Hankinson [7] overcomes the difficulties and errors associated with the technique [39] and extends its application to cover any geometrical shape by dividing the entire surface into triangular area elements. Once the triangles have been defined, their contributions to the shape factor are calculated and summed. His method for doing this is derived from the equation for the radiative interchange between two differential area elements [42] as described in section 2.2.2.

2.2.2 Shape factor between two differential area elements

Equation 2-19 gives the shape factor for energy transfer from one differential area element to another, per unit area of the source. In this case the source of the energy is the i^{th} triangle dS_i of the flame surface S, and the target is dT [42].

$$dF_{dS_i \to dT} = \frac{\cos\theta_{S_i} \cos\theta_{T_i}}{\pi r^2} dT \qquad \text{[no units]} \qquad (2\text{-}19)$$

Figure 2-2 illustrates the components of this equation.

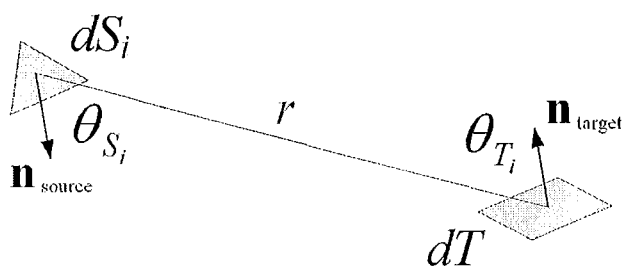

Figure 2-2: Radiative exchange between two differential area elements.

When considering radiative exchange, energy travelling in both directions must be taken into account. In Figure 2-2, the net total energy leaving dS_i is $\sigma\,(T_S^4 - T_{dT}^4)\,dS_i$ [W]. Therefore, the net total energy received at dT can be written [42]

$$d^2Q'_{dS_i \Leftrightarrow dT} = \sigma\,(T_S^4 - T_{dT}^4)\,F_{dS_i \to dT} dS_i \qquad \text{[W]} \qquad (2\text{-}20)$$

The quantity $d^2Q'_{dS_i \Leftrightarrow dT}$ is a second differential to denote the dependence on two differential quantities dS_i and dT, and the prime indicates a quantity applied in a single direction. This is consistent with notation used in Siegel and Howell.

To find the shape factor for the entire flame surface, the contributions of all triangles must be summed.

2.2.3 Radiative interchange between a finite surface and a differential area element

The shape factor for radiant heat transfer from the entire surface to the target element is, as used by Hankinson [7], given by

$$dF_{S \to dT} = \sum_{i=1}^{N} \frac{\cos\theta_{S_i} \cos\theta_{T_i}}{\pi r_i^2} dS_i \qquad \text{[no units]} \qquad (2\text{-}21)$$

Note that the shape factor in equation (2-21) is now *per unit area* of the target since it has been divided by dT. The net radiation received at the target from the entire flame surface is

$$Q'_{S \to dT} = \sigma\left(T_S^4 - T_{dT}^4\right) \sum_{i=1}^{N} \frac{\cos\theta_{S_i} \cos\theta_{T_i}}{\pi r_i^2} dS_i \quad [\text{W/m}^2] \qquad (2\text{-}22)$$

where

N = the total number of triangles in the surface that represents the flame.

We are considering *hemispherical* emissivity, which means that a surface element emits equally in all directions. The emissivity is hemispherical because the element is contained in a surface, whereas a point source in space has spherical emissivity. Hence, the contribution of an area element to the total shape factor is zero if either $\cos\theta_{S_i} \leq 0$ or $\cos\theta_{T_i} \leq 0$. This is because either the target is not contained in the field-of-view of the area element, or the area element is not contained in the field-of-view of the target.

Hankinson [7] applied his method to calculate the shape factor for an oblique conical frustum of elliptical cross section. By adjusting its parameters this model could be made to represent a wide range of flame shapes associated with large-scale fires. Included in his method is a technique for dividing the surface of the conical frustum into triangular elements from which the shape factor is determined. This involves defining the three surface points that are the vertices of each triangle. His technique is a general method that can be applied to any solid shape without restricting either the regularity or the number of shapes.

Limitations

One must be able to define the shape and therefore define the triangles that represent the surface in order to apply the method. This can be difficult for multiple irregular shapes and may be why Hankinson trialed his method on a surface with regular geometry, similar to many other pool fire representations.

2.3 Summary

The simple geometry used for modelling pool fires works well. Shokri and Beyler [41] pointed out that the uncertainty in this application was in the definition of the emissive power. However, simple geometries such as points and cylinders are not appropriate for modelling complex irregular shapes. Hankinson [7] provides a method that can successfully determine shape factors for complex irregular shapes; however the application of his method has been restricted by the absence of techniques for defining irregular flame geometries.

2.4 Specific Objectives for this Study

To accurately determine the heat flux at a given target it is necessary to accurately determine the radiative properties of the emitting surface and the shape factor between that surface and the target. The focus of this study is to accurately determine the shape factor. Determining the shape factor accurately depends on how well the flame

geometry has been defined. Therefore, the essential component of our task is to accurately define the size and shape of the flame.

Our specific objectives are then to:

- Develop a method that can accurately define irregular flame geometries.
- Calculate shape factors at targets without imposing restrictions on location or orientation.
- Accurately determine the thermal radiation field surrounding the flame from heat flux calculations based on shape factors derived from the flame's geometry.

Chapter 3

Heat Flux Predictions from Video of Fires (Development of Techniques)

This chapter presents the techniques that we have developed to make heat flux predictions from the video of fires. These techniques are explained and their use is justified.

3.1 Flame Properties – Assumptions

The following assumptions are made concerning the properties of the flame:

1. The flame is a *diffuse* emitter, which means that the intensity of emitted radiation is uniform over all directions.

2. The flame is a *gray* emitter, which means that the intensity of emitted radiation does not depend on wavelength. It can, however, depend on temperature. At each surface temperature the emitted radiation will be the same fraction of blackbody radiation for all wavelengths. A *diffuse-gray* surface therefore emits radiation that is a fixed fraction of blackbody radiation for all directions and wavelengths [42].

3. A given flame surface will have uniform temperature and, following from the second assumption, will have uniform emittance over the entire surface.

4. We will also assume the flame to have emissivity $\varepsilon = 1$, which means it emits as much radiation as a black body. This assumption is made tentatively in the interests of simplicity and is reviewed during the investigation

3.2 Recording the Fire

Data required from the experiment can be categorised as:

- Video of the flame – from each camera position.
- Heat flux gauge readings.
- Reconstruction information.

3.2.1 Video

There are two types of information that can be considered for extraction from the video of the fires:

1. Flame intensity.
2. Flame location.

Each type of information has special requirements for recording, image processing, and for reconstructing the flame in 3D. Accurate flame intensity data was found to be unattainable with a standard "consumer grade" camera, so methods have been employed that pertain to flame location information.

3.2.1.1 *Why flame intensity is not attainable*

In digital imaging, *dynamic range* is a term given to the ratio between the brightest and darkest recordable parts of a scene [22]. A compartment fire presents an extreme dynamic range that is often beyond a camera's linear operating range. It is the linear

range that measures how well the camera functions as a radiometric detector and produces quantitative results [31].

Factors affecting a camera's linear range

The purpose of a video camera is to convert light input into electrical output signals. The key to this operation is a type of semiconductor that is sensitive to light called a *charge-coupled device* (CCD). A CCD consists of a 2D array of individual elements, each of which is, in essence, a capacitor [19]. Charge is created in each CCD detector, or pixel, when photons strike the semi-conducting material and generate electrons. A transfer function describes how the resulting pixel intensities vary with the amount of light going into the lens [16].

The amount of charge an individual pixel can hold before saturating is called *full well capacity* (FWC). If each individual pixel can be thought of as a well of electrons, then saturation refers to the condition when the well is full. As a well approaches saturation, the accumulated charge tends to repel further electrons causing the linear relationship between light intensity and accumulated charge to degrade. The point at which this degradation exceeds an acceptable level is defined as *linear full well* (LFW). The LFW is lower than the total non-linear FWC and should be used for dynamic range calculations [32].

Dynamic Range = (Linear Full Well [electrons] / Read Noise [electrons]),

Read noise, also called Preamplifier noise, is generated by the on-chip output amplifier and is associated with a single readout event.

When pixels are saturated and can hold no additional charge, this charge spills into neighbouring pixels causing them to either report erroneous values or also saturate. This spread of charge to adjacent pixels is known as *blooming* and appears as a white streak or a blob in the image. For this reason, if the CCD is overexposed, the image will wash

out quickly. When overexposure occurs, the CCD produces signals that are above the dynamic range of the analogue-to-digital converter. The output is then clipped to the maximum of the A/D converter. At low light intensities the CCD does not respond well and is again non-linear. In this case, output will either taper off to a tiny value or be lost in low-level noise [17]. Therefore, the transfer function is not a straight line but sigmoid in shape as the example for a Sony DCR-TRV900 Camcorder shows in Figure 3-1 [1].

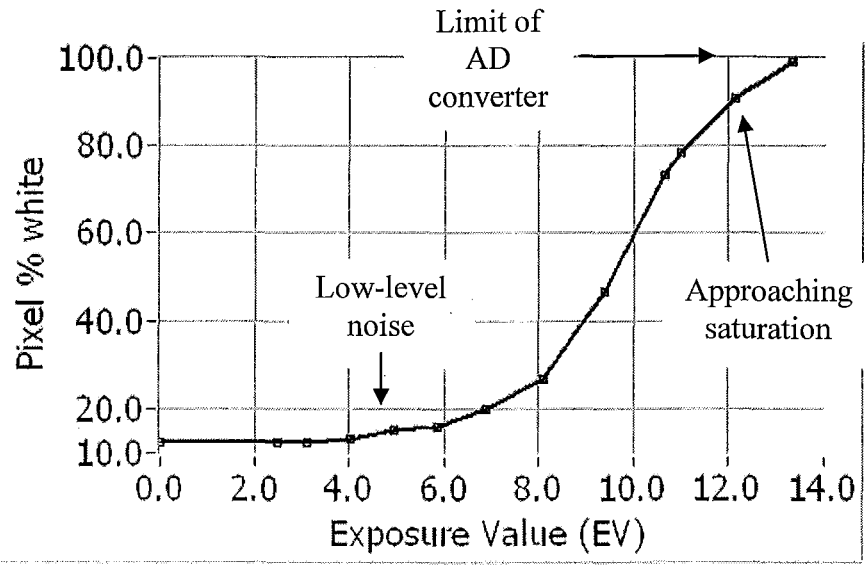

Figure 3-1: Transfer function for a Sony DCR-TRV900 Camcorder.

Gamma correction

All devices that are used in digital image manipulation like digital still cameras, scanners, monitors, video grabbers and printers each have their own transfer function or transmission characteristics. They alter the intensity distribution of the image data, some in a highly non-linear manner [20].

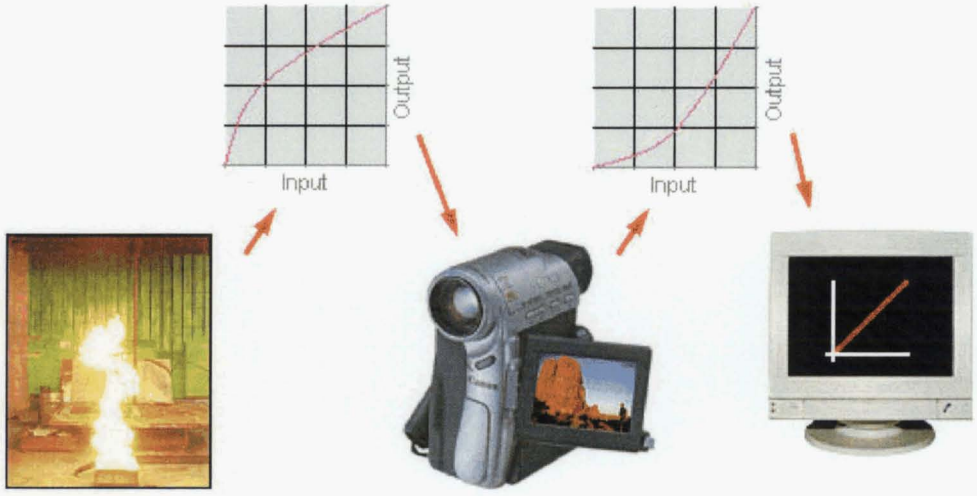

Figure 3-2: Camera with built-in gamma to compensate for display devices.

When viewing an image generated by a CCD camera, what is seen has been altered by the camera's transfer function and the transfer function of the display device (see Figure 3-2). Cathode ray tube (CRT) monitors have a non-linear, *gamma*, response to their input signal. In the early days of the television industry it was decided that it would be cheaper to apply an inverse transfer function to the video-signal in order to compensate for the CRT gamma. This way expensive non-linear signal processing was not needed in TV receivers so the cost of the receivers was kept at minimum [14]. As a result, there is gamma compensation built into many products including inherently linear devices like scanners and digital cameras.

Some cameras allow the gamma correction to be turned off [20], which allows them to better approximate a linear recording system. Often however, gamma correction is fixed by the manufacturer and is not specified. Also, consumer grade CCD cameras often have a transfer function that does not follow the gamma well [14]. This requires one to measure the transfer function and calibrate the camera if the intention is to extract intensity measurements.

Summary

At high light intensities, as the pixel approaches saturation, the camera's transfer function becomes non-linear. At higher intensities, overexposure can occur. At low light intensities the output can be lost in low-level noise. An, often unspecified, gamma function is present without the means to shut it off. Commercial CCD cameras usually operate on a "point and shoot" scheme where most functionality is automatic and hidden. The manufacturer may not publish detailed specifications and it may not be possible to manually set the desired camera parameters. These factors can make a camera unsuitable for quantitative imaging where linearity is a stringent requirement. For these reasons we have chosen not to attempt to record intensity data, and have focused on capturing flame location information.

3.2.1.2 *Camera settings and placement*

Following the discussion in 3.2.1.1, our goal is to capture the location of the flame. This requires us to determine, for each frame of video, whether or not the flame's image is present at a pixel location. The required data can be easily extracted from frames of a video if the entire flame is clearly distinguished against its background. This can be achieved by suitably adjusting the camera parameters and by ensuring there are no bright or reflective surfaces within the cameras' view that could interfere with the flame.

Placement of the cameras is subject to physical constraints imposed by the geometry of the laboratory. That is, the distance from the flame to the walls, the location and size of the windows, etc. Within these constraints there is some flexibility provided that the entire flame can be seen in the camera's field of view.

3.2.2 Heat flux data

The recorded heat flux information is necessary for validating the model. The serial numbers of the heat flux gauges should be recorded along with calibration information. For example, gauge #124100 may read 20 mV at 100 kW/m^2. A numbering scheme is

required for all gauge positions used in the experiment, along with the (x, y, z) coordinates for their positions.

If the gauges are moved during the experiment, a record of which gauge is used in which position and at what time is required so that values in the data file can be correctly attributed to time and place.

3.2.3 Reconstruction information

In addition to heat flux data, it is necessary to accurately specify the relative positions and geometry of essential objects. This is required in order to determine the geometric projection used to reconstruct the flame. Defining a coordinate system, by specifying the location of its origin and the direction of its coordinate axes, achieves this. Then, the (x, y, z) positions of all relevant objects are recorded using this coordinate system. In addition to the heat flux gauges and cameras, two reference points for each camera position are also required. How this information is used is explained in the section on Flame Reconstruction.

Whether to use a left-handed or right-handed coordinate system is a matter of choice. We adopted a right-handed system because it is the convention used by OpenGL [13]. Figure 3-3 shows the positive direction of each axis.

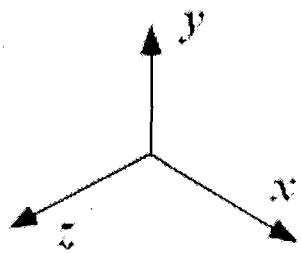

Figure 3-3: Right-handed coordinates.

3.3 Image Processing

The goal of image processing is to separate the flame from its surroundings. This is done for each frame of the video in three steps:

1. Extract a colour plane to produce a greyscale image.
2. Threshold the extracted colour plane.
3. Average the resulting series of consecutive images.

3.3.1 Extracting a colour plane

The objective is to extract a greyscale image that has most contrast between the flame and its background.

An image in RGB format uses 24 bits for each pixel, which means that each respective value for red, green and blue is represented by a byte (or 8 bits). Similarly, the HSL colour space uses a byte each for representing hue, saturation and luminance. Any one of these colour planes can be easily extracted and displayed as a greyscale image. Algorithms for converting between RGB and HSL, and other colour spaces are well known [5].

Colour video of the flame is processed, frame-by-frame, as a series of RGB images. From each frame we can extract a greyscale image prior to applying a threshold. One method could be to convert each colour frame to greyscale, which is done by averaging the red, green and blue components for each pixel. However, by choosing a more appropriate colour plane the success of the subsequent threshold operation can be enhanced. A number of colour planes that can be chosen:

RGB – Red Plane	HSL – Hue Plane
RGB – Green Plane	HSL – Saturation Plane
RGB – Blue Plane	HSL – Luminance Plane

It is wise to try each plane to see what works best for a given video.

3.3.2 Thresholding

The next step in isolating the flame is to threshold the extracted greyscale image based on a specified range of intensities. All pixels having intensities within this range are given the value 1, while pixels having intensities outside this range are given the value 0. The image in Figure 3-4b shows the result of applying a threshold to the video frame in Figure 3-4a. The upper limit of the threshold range is fixed at 255, while the lower limit will need to be adjusted by trial.

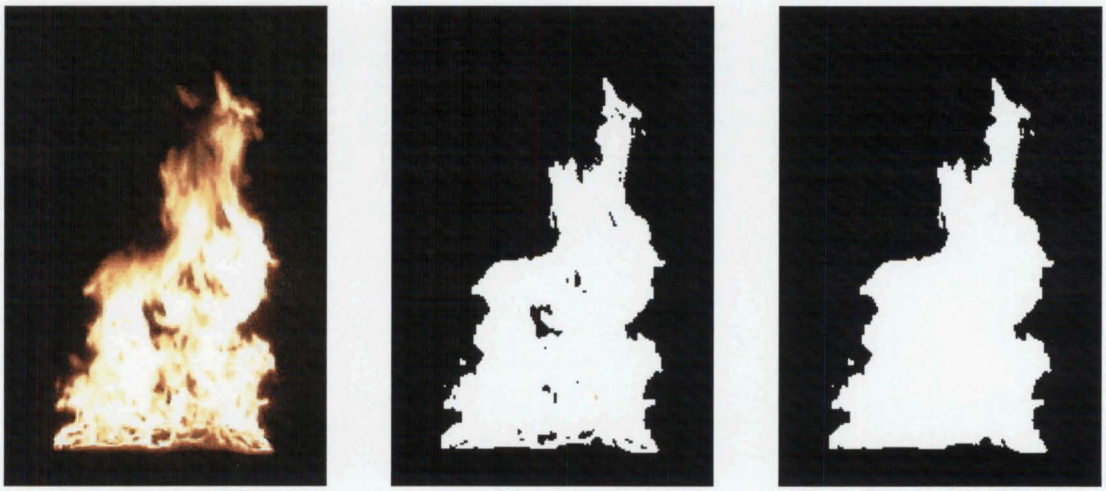

(a) Frame (b) Threshold (c) Fill holes

Figure 3-4: Thresholding and filling holes.

3.3.2.1 *Checking the Success of the Threshold Range*

The best value to use for the lower limit can be decided by comparing the images before and after thresholding (for example, compare Figure 3-4a with Figure 3-4b). Judgement is required to determine whether the entire flame has been successfully isolated from its background. Here is another way to check that image processing has successfully isolated the flame [40]. Invert the binary image, produced by applying a threshold, and use this to mask the original video frame. The result is the rejected portion of flame. It should be minimal as in Figure 3-5c.

(a) Frame (b) Mask (c) Rejected portion

Figure 3-5: Verifying the success of image processing.

3.3.2.2 *Filling Holes*

Notice the holes present in Figure 3-4b after thresholding. If a video is dark and has failed to capture areas of flame that are thin and have low intensity, then holes can appear in the flame. This type of image does not provide reliable flame probability information since regions of the flame are missing. Applying a *fill holes* algorithm [29] can improve the quality of the data. Figure 3-4c shows the results of its use:

3.3.3 Averaged image

3.3.3.1 *Temporal average to suppress noise*

The turbulent flame produces a large component of random noise in each frame of the video. A noise suppression technique is required so that reliable location information can be obtained. The sequence of thresholded images $\{a_p[m,n] \mid p = 1,2,\ldots,P\}$, with pixel dimensions $m \times n$, can be considered to contain exactly the same object, which differs only in the sense of independent noise realizations. Then, since the noise is additive, an averaged image $\hat{a}[m,n]$ can be produced from a sequence of images where the mean value of each pixel is unchanged. For each pixel, however, the standard deviation will decrease from σ to $\sigma/\sqrt{P}$.

Temporal averaging:
$$\hat{a}[m,n] = \frac{1}{P}\sum_{p=1}^{P} a_p[m,n] \qquad (3\text{-}1)$$

A black and white thresholded image shows whether the flame occupies a pixel. Therefore, an averaged pixel value represents the proportion of time a flame occurs at that location.

3.3.3.2 *Example using two frames*

Figure 3-6 illustrates the averaging of two video frames. The result is an 8-bit greyscale image in which the white region represents pixels occupied by the flame 100% of the time (i.e. the flame is there in both images). The grey area represents the pixels occupied by the flame 50% of the time (i.e. the flame is there for 1 frame only), and the black area represents the pixels where the flame never occurred.

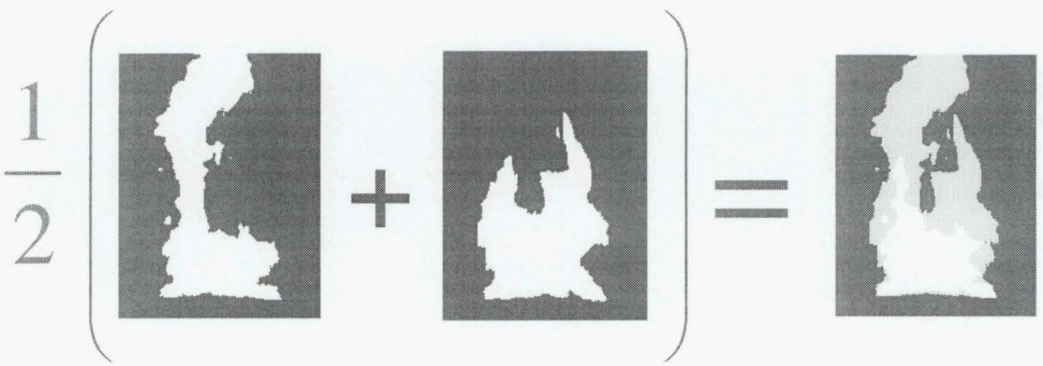

Figure 3-6: Averaging two video frames.

3.3.3.3 *Determining the averaging period*

Averaging over too short a time period will not give a true picture of flame probability, while averaging over too long a time period can cause problems with an uncontrolled flame, since the sequence of images cannot be considered to contain exactly the same object. Therefore, a suitable time period needs to be established. The following investigation addresses this problem.

A series of average images was produced from a video of a controlled flame. The series begins with a single frame, followed by an average of two frames, followed by an

average of three frames, and so on up to an average of 255 frames[3]. Then a threshold was applied to each of the averaged images and the number of white pixels in each was counted. An example of this is shown in Figure 3-7. Figure 3-7a is an average of 12 video frames and Figure 3-7b has had a 75% threshold applied. There are 6626 white pixels in Figure 3-7b.

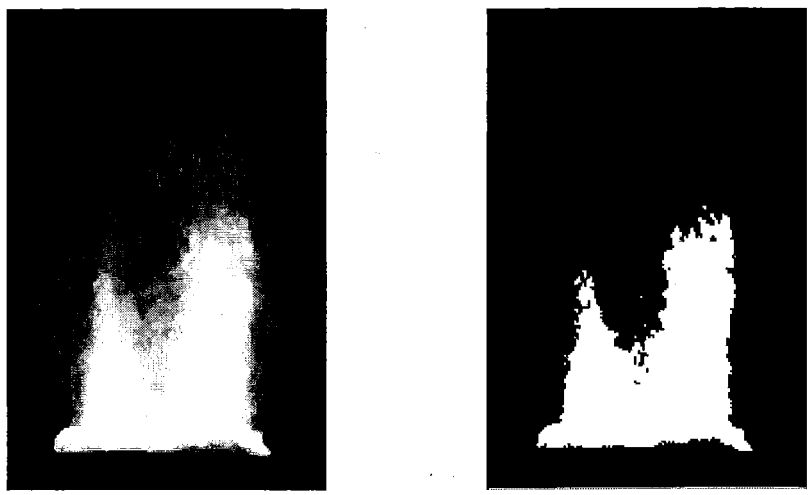

(a) Average of 12 frames (b) 75% threshold

Figure 3-7: Investigating the stability of averages.

The white pixel count was graphed against the number of frames comprising the average for all images. Figure 3-8 shows the results for a 75% threshold along with a 50% and a 25% threshold. This graph provides an indication of when the averaged image becomes stable and therefore suggests a suitable time period for averaging. Notice that prior to about 150 frames (that is 5 seconds at 30fps) the graph has almost stabilised, which indicates that one should accumulate an average over at least this time period. 180 frames (6 seconds) would be a better choice. We assume that this result can also be applied to an uncontrolled flame.

[3] This number (255) was arbitrarily chosen and has no significance except that it uses all greyscale values.

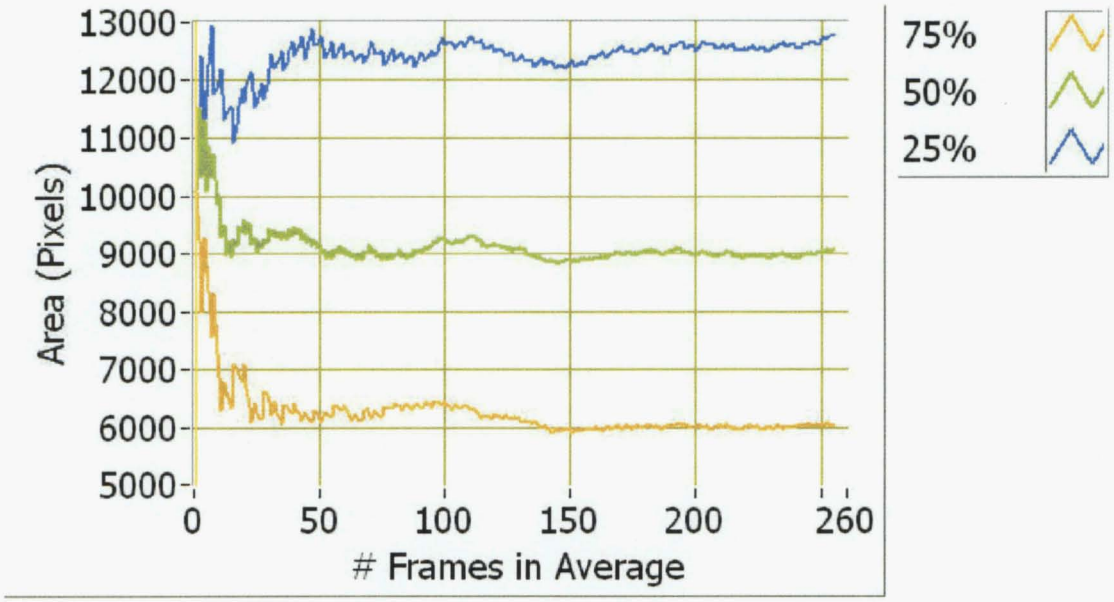

Figure 3-8: Number of Pixels vs. Number of Frames becomes stable around 180 frames.

3.3.4 Changing from image coordinates to world coordinates

The convention for 2D image and screen coordinates is to have the origin in the top-left corner with x-values increasing to the right and y-values increasing downwards (see Figure 3-9a for a 6×6 pixel example). A pixel's value occupies a finite area in an image and on the screen, but we require a pixel to be referenced as a distinct point. This point is the taken to be the centre of the pixel as illustrated in Figure 3-9b. Recall that we have assumed the centre of the image is located at the origin of viewing coordinates. Therefore, pixel coordinates must be rewritten. For an image with dimensions $N \times M$ (width × height), the conversion from screen to viewing coordinates is:

$$x_V = x_S - \frac{N}{2} + 0.5$$

$$y_V = (M-1) - y_S - \frac{M}{2} + 0.5$$

For example, a pixel in 3-9a with screen coordinates $(x_S, y_S) = (3, 4)$ and $N = M = 6$ corresponds to the point $(x_V, y_V) = (0.5, -1.5)$ in viewing coordinates, found thus:

$$x_V = 3 - \frac{6}{2} + 0.5 = 0.5$$

$$y_V = (6-1) - 4 - \frac{6}{2} + 0.5 = -1.5$$

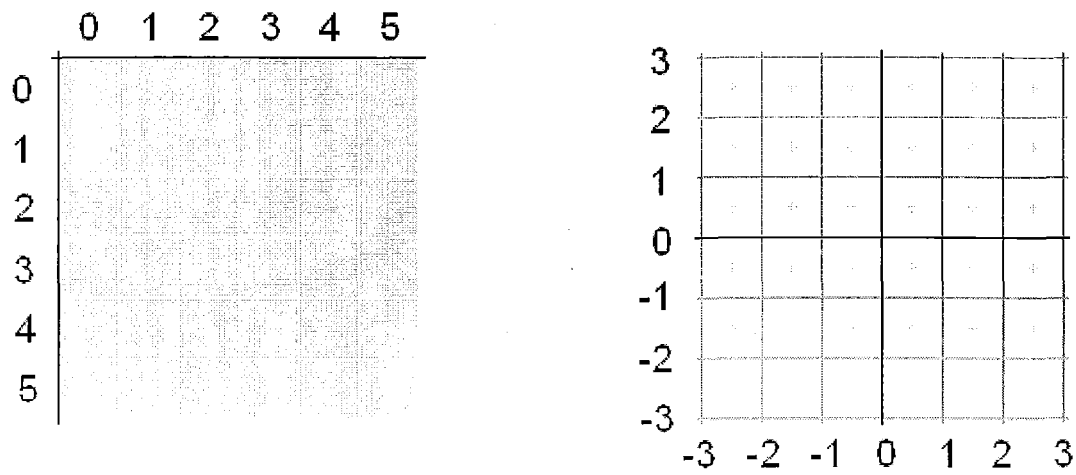

(a) Image and screen pixels (b) Viewing coordinates

Figure 3-9: Changing pixel coordinates to viewing coordinates.

3.4 Flame Reconstruction

3.4.1 Producing a point cloud

We need to establish flame probability information in 3D space. This can be done by initialising a cloud of points in the region of the flame and then projecting the flame probability data contained in the averaged images to these points. The values assigned to the points will refer to the probability of the flame occurring at that location.

3.4.1.1 *Image calibration*

To define the correspondence between pixels and real world units, the image must be calibrated. For example, in Figure 3-10a, the base of the flame is 107 pixels wide, and was known to be 600mm wide in real world units. Therefore, 5 pixels correspond to 28mm. Since the pixels are square, the vertical calibration will be the same as the horizontal calibration.

3.4.1.2 *Establishing Point Cloud Boundaries*

The point cloud must be established in a region that contains the entire flame. This may require a suitable margin to be added on all sides. For example, the flame in Figure 3-10 has base dimensions of 600mm × 300mm. 100mm was added on all sides and the height was estimated to be about 1200mm. This worked for the front view, but the side view revealed the flame was leaning to the left. For the left side, a margin of 200mm is established. These boundaries are indicated in Figure 3-10.

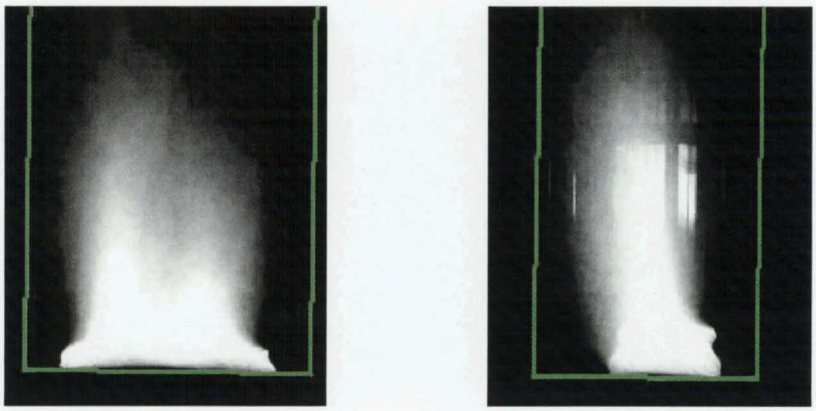

(a) Front view (b) Side view

Figure 3-10: Boundary of the reconstruction space.

3.4.1.3 *Random Points vs. Regular Grid*

The points in the cloud can be considered as samples of the flame probability information that is contained in the averaged images and is projected from the camera positions. It is preferable that these samples are taken in a way that avoids aliasing. Aliasing occurs when a reconstruction produced from the samples does not accurately represent the underlying information. The Nyquist sampling theorem says the sampling rate should be at least twice the highest frequency in order to have the information uniquely reconstructed without aliasing [23].

Generally, sampling on a regular grid can lead to aliasing if the grid spacing is too wide, whereas random sampling can leave large unsampled regions [12]. However, if the reconstruction space is filled with a sufficiently large number of points, so that the risk of aliasing is insignificant, then the choice between random or regular becomes arbitrary. It remains to decide what constitutes a "sufficient number of points".

3.4.1.4 *Establishing Point Cloud Density*

The greater the density of points in the cloud, the greater is the sampling frequency. In producing the averaged images a temporal smoothing has been applied, which has the effect of spatially smoothing the flame position in these images. Where turbulence (i.e. noise) was greatest in the flame, lower frequencies dominate in the averaged image.

Here, lower frequencies are characteristic of an area in an image where transitions from light to dark are gradual. Conversely, higher frequencies are characterised by abrupt changes from light to dark. For example, notice the sharp flame boundary near the base of the flame in Figure 3-11.

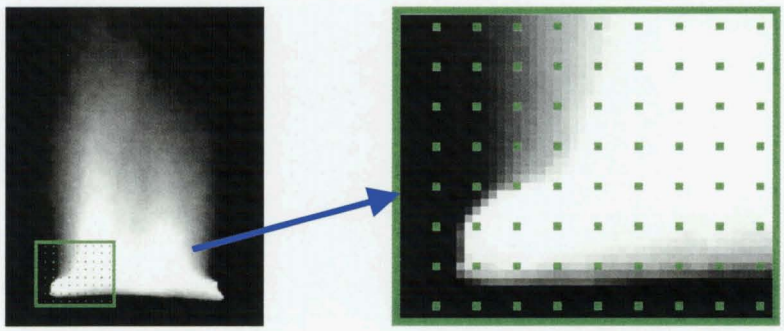

(a) Average image (b) Density of point cloud

Figure 3-11: Establishing the number of points in the cloud.

By inspecting the averaged images a suitable density for points can be estimated. For example, Figure 3-11b represents a point cloud with five pixels between points. We need to establish whether this, somewhat arbitrary, estimate provides an acceptable sampling frequency.

3.4.1.5 *Verification of Proposed Point Cloud Density*

Aliasing can be avoided if the bandwidth of the signal (the image) is limited to below one-half the sample rate with a low-pass filter [15]. This can be achieved in the frequency domain using a Butterworth Low-Pass Filter (BLPF). This filter is used because it gives a continuous monotonic response that can reduce ringing effects in image space [11]. The attenuation of frequencies in frequency space is described by

$$H(u,v) = \frac{1}{1+\left(\frac{D(u,v)}{D_0}\right)^{2n}}, \tag{3-2}$$

where:

$D(u,v) = \sqrt{(u^2 + v^2)}$ = Distance from the origin,

D_0 = Cut-off distance (from the origin),

n = order – the larger the order, the steeper the cut-off will be.

Both the distance $D(u,v)$ and the cut-off distance D_0 have a maximum that is half the length of a diagonal.

The procedure is:

- Create an image with the same dimensions as the averaged images to be used in the flame reconstruction.
- Make a pattern that repeats vertically and horizontally with half the pixel frequency that equates to the proposed point cloud density. That is, it repeats every 10 pixels for the example we have been using since the proposed point cloud density is equivalent to 5 pixels.
- Adjust the parameters of the Butterworth filter until the repetitive pattern has just been filtered out.
- Apply the Butterworth filter, with the chosen parameters, to the averaged images.

As an example, Figure 3-12a shows the test pattern produced to repeat every 10 pixels. Figure 3-12b shows the same pattern after being filtered with the low-pass Butterworth filter. Figure 3-12c shows the averaged image from the front camera position, and Figure 3-12d shows this image after being filtered with the same Butterworth filter.

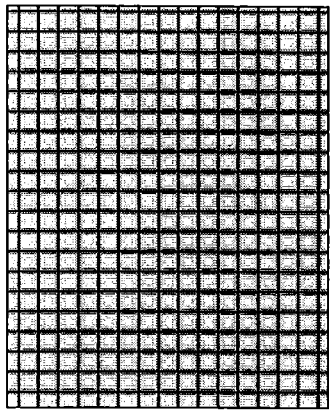

(a) Test pattern.

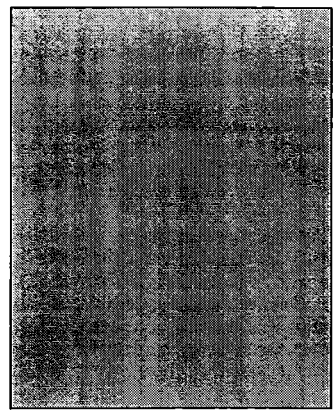

(b) Filtered test pattern.

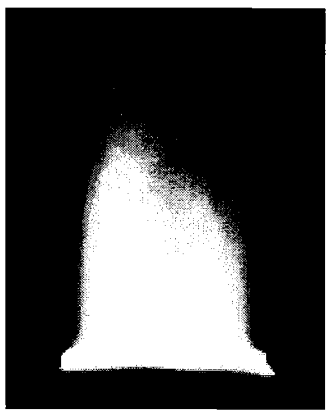

(c) Image

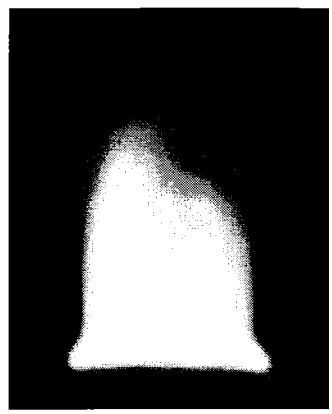

(d) Filtered image

Figure 3-12: Low-pass filter to avoid aliasing.

Comparing the images, before and after filtering, it is apparent that very little change has occurred in the main body of the flame. This is due to the spatial smoothing inherent in the temporal averaging. The only significant change occurs at the base of the flame where higher frequencies are present. It is difficult to say whether the error resulting from this is better or worse than what might have been caused by aliasing. Since the base constitutes a very small portion of the total flame, this error is not considered to be significant.

3.4.1.6 *Reconstruction Techniques*

There are two main categories of reconstruction methods to obtain a 3D image from 2D projections. There are direct methods that employ the Fourier Slice Theorem and there are iterative methods that seek to solve the reconstruction problem by solving a set of simultaneous linear equations [37]. Filtered Back Projection (FBP) is the most prominent of the Fourier space methods and the Algebraic Reconstruction Technique (ART) is the major iterative method. Both methods solve the problem for intensity information, which makes them unsuitable for this application. As a result, we have developed a technique called *Minima Reconstruction*.

3.4.1.7 *Minima Reconstruction Technique (MRT)*

Description

In this method the images are projected back through a cloud of points whose values are initially set to 1.0 (100%). If the intensity projected to a point is less than the point's current value, then the current value is overwritten by the lower projected value. The final value of a point becomes the minimum of all values projected to it. If, at any time, a value of zero is projected to a point, that point is removed from the cloud.

This process is illustrated in Figures 3-13a, b and c for the case of parallel 2D projections. Figure 3-13a shows the reconstruction space; a rectangle initialised to 1.0 (white)[4], and an intensity profile that will be projected from the right. Figure 3-13b shows the result of the first projection and an intensity profile that will be projected from below. Finally, Figure 3-13c shows the result of both projections.

[4] This corresponds to 255 for an 8-bt image.

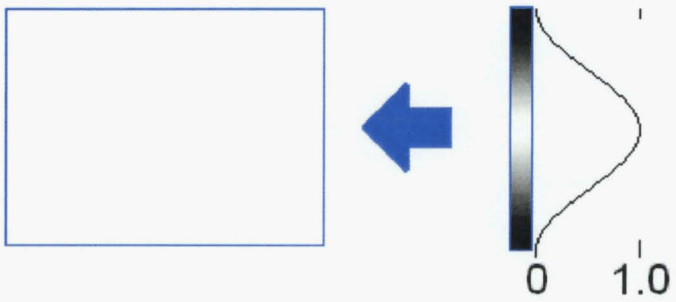

(a) Parallel MRT – maximum initial values.

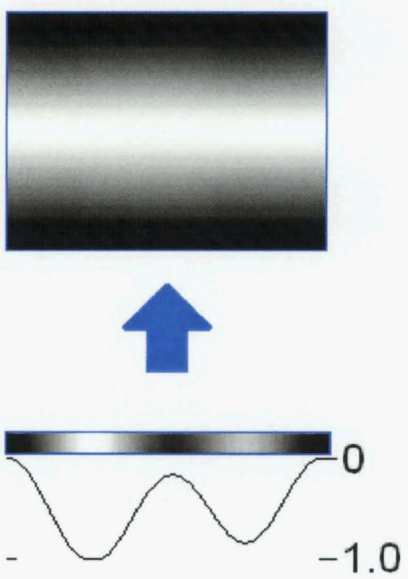

(b) Parallel MRT – after 1st projection.

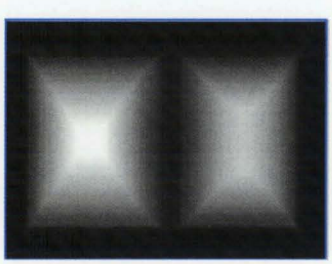

(c) Parallel MRT – after 2nd projection.

Figure 3-13: Parallel Minima Reconstruction Technique.

3.4.1.8 *Perspective Projection: Issues and Implementation*

Light rays received by a camera cannot be assumed parallel unless the distance between the object and the camera is sufficiently large. This is not always the case so the perspective nature of incoming light must be accommodated if we hope to accurately reconstruct the flame.

Every point in an image represents a possible line of sight of an incoming light ray. Any 3D point along the ray projects to the same image point, so only the direction of the ray is relevant, not the distance of the point along it [25]. Light travels along these rays to the camera when an image is captured and, for an accurate reconstruction, the same rays must be used by a projection. The diverging rays of a perspective projection can introduce error into a reconstruction as shown in Figure 3-14. Errors will occur even without perspective if there are not enough projections.

Two projections

In Figure 3-14a, it can be seen how error can occur in the case of the 2D circle reconstruction from two orthogonal projections. Notice how, in Figure 3-14b, the error increases rapidly as the angle between the cameras moves away from 90°. These diagrams exaggerate this effect with a field-of-view of 34°. For two cameras, orthogonal projections produce minimum error.

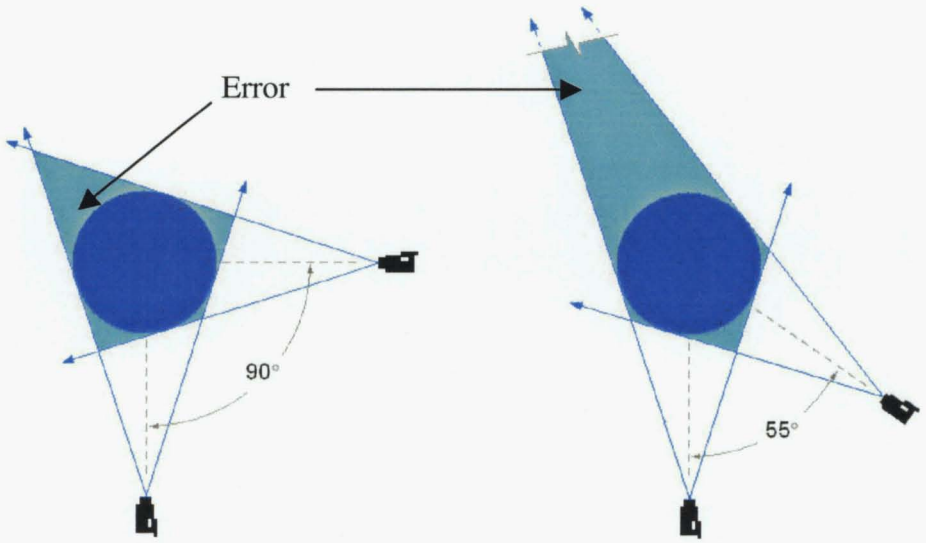

(a) 2 orthogonal cameras. (b) 55° between projections.

Figure 3-14: Error in minima reconstruction due to perspective.

More than two projections

Referring again to the reconstruction of the circle in 2D, as the number of projections increases the circle will become smoother. This is shown for the case of three equally spaced projections in Figure 3-15a. Generally, a better reconstruction is obtained if the number of projections is increased.

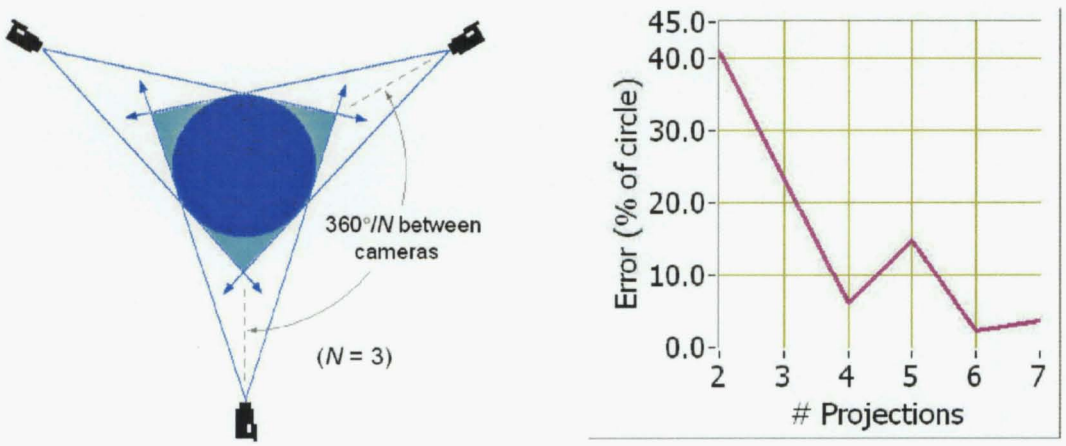

(a) *N* cameras equally spaced. (b) Increase projections to reduce error.

Figure 3-15: Increasing the number of projections reduces the error in minima reconstruction.

Figure 3-15b graphs the results of a calculation investigating how the reconstruction error decreases as the number of projections increases. Data for this graph is taken from the diagrams in Figure 3-14a, Figure 3-15a and four more diagrams based on these. In these diagrams the circle has a diameter of 124 pixels and the cameras are placed at a distance of 203 pixels from the centre of the circle. The error (the grey region) is expressed, on the vertical axis, as a percentage of the area of the circle. The error drops from 41% for two orthogonal projections to 6% for four projections equally spaced. The rise at five projections is peculiar to the geometry of this scenario (180°/5 = 36°) and the similarity with the field-of-view of 34°. This phenomenon recurs in a much lesser way at seven projections. Despite these aberrations, this illustrates how rapidly the error decreases.

Although in general it is best to space cameras at equal angles, there will be times when knowledge of the geometry of the object will give rise to a better camera placement plan.

Implementation in 3D

Our task is to implement minima reconstruction including perspective views in 3D. To accomplish this it is necessary to find, for each projection, the transformation that maps points in world coordinates to pixels in image coordinates. Then, projecting backwards, flame probabilities can be mapped to points in world coordinates. This process is repeated for every point in the cloud.

The geometry of this task is shown in Figure 3-16. The Object (the flame) exists in the real world and the Image is the picture produced by the camera. The origin of a world coordinate system has been established at the centre of the base of the flame. Its x, y and z-axes are in a right-handed configuration. The camera, **C**, is located at the *centre of projection* (COP). The COP is the point at which all projection rays converge. The Image lies in the viewing plane and the origin of the viewing plane, the *view reference point* (**VRP**), is the centre of the image. The **VRP** is specified in world coordinates and locates the origin of the viewing plane. The orientation of the viewing plane is defined by the direction of its normal **n**, which is given by the vector from the camera to the

VRP. The vector **v** is the viewing plane's *up* vector, and the vector **u** is calculated as the cross product of **n** and **v**. The orthogonal vectors **u**, **v** and **n** define the axes of the viewing coordinate system. Notice that, unlike the world coordinate axes, the viewing coordinate axes constitute a left-handed system, since it is more intuitive to have distance increasing positively as one moves forward from the camera towards the **VRP**. In the work that follows, the subscript *W* indicates a quantity expressed in world coordinates and the subscript *V* indicates a quantity expressed in viewing coordinates.

The reference points $\mathbf{P}_1$ and $\mathbf{P}_2$ appear in the image as $\mathbf{P}_1'$ and $\mathbf{P}_2'$ respectively. Initially, the locations of $\mathbf{P}_1'$ and $\mathbf{P}_2'$ are known only in viewing coordinates. In viewing coordinates the viewing plane is defined by the equation $z = 0$. Therefore, since the image lies in the viewing plane, the z components of $\mathbf{P}_{1V}'$ and $\mathbf{P}_{2V}'$ are equal to zero.

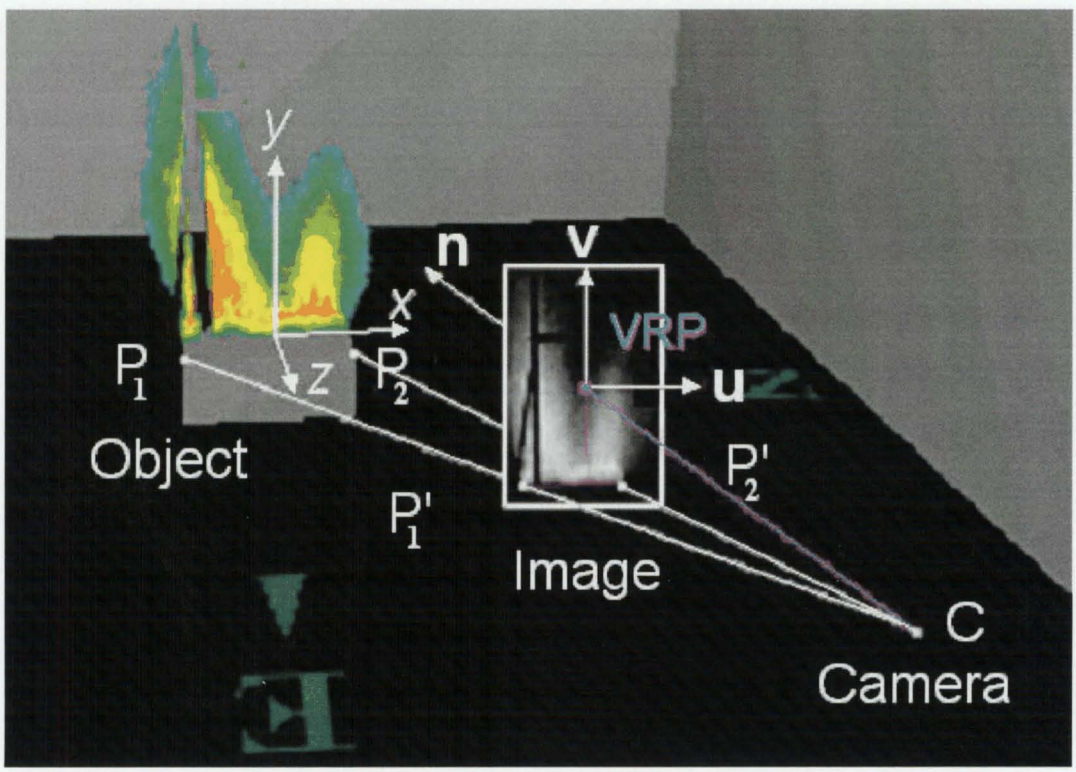

Figure 3-16: Constructing the transformation matrix.

The transformation is a combination of two matrices:

1. A *change of coordinates* matrix (M_{view}), which maps a point in 3D world coordinates to a point in 3D viewing coordinates.

2. A *scaling* matrix (M_{scale}), which accounts for perspective and maps a point in 3D viewing coordinates to 2D image coordinates.

The change of coordinates combines a rotation and a translation and can be written [5]:

$$M_{view} = R\,T, \tag{3-3}$$

where the rotation is defined as

$$R = \begin{bmatrix} u_x & u_y & u_z & 0 \\ v_x & v_y & v_z & 0 \\ n_x & n_y & n_z & 0 \\ 0 & 0 & 0 & 1 \end{bmatrix}, \tag{3-4}$$

and the translation is defined as

$$T = \begin{bmatrix} 1 & 0 & 0 & -VRP_x \\ 0 & 1 & 0 & -VRP_y \\ 0 & 0 & 1 & -VRP_z \\ 0 & 0 & 0 & 1 \end{bmatrix}, \tag{3-5}$$

Notice that the first three elements in the first three rows of the rotation matrix, R, are taken from the normalised direction vectors that define the axes of the viewing coordinate system. Notice also that the first three elements of the fourth column of the transformation matrix, T, are taken from the **VRP**, which locates the origin of the viewing plane. Therefore, to define the change of coordinates transformation it is necessary to determine **VRP**, **n** and **v**.

The general form of the scaling transformation is given by equation [3-6]:

$$M_{scale} = \begin{bmatrix} 1 & 0 & -x_{CV}/z_{CV} & 0 \\ 0 & 1 & -y_{CV}/z_{CV} & 0 \\ 0 & 0 & 1 & 0 \\ 0 & 0 & -1/z_{CV} & 1 \end{bmatrix} \tag{3-6}$$

In this matrix, the values x_{CV}, y_{CV} and z_{CV} are taken from the camera position as it is expressed in viewing coordinates. That is, $\mathbf{C}_V = (x_{CV}, y_{CV}, z_{CV})$. We assume that the camera is located on the z-axis of the viewing coordinate system. This allows us to rewrite the camera position in viewing coordinates as $\mathbf{C}_V = (0, 0, z_{CV})$. Further, to accommodate the change from a right-handed world coordinate system to a left-handed viewing coordinate system it is necessary to remove the negative sign from row four column three. The scaling matrix becomes:

$$M_{scale} = \begin{bmatrix} 1 & 0 & 0 & 0 \\ 0 & 1 & 0 & 0 \\ 0 & 0 & 1 & 0 \\ 0 & 0 & 1/z_{CV} & 1 \end{bmatrix} \tag{3-7}$$

The unknowns in these transformation matrices can be found using a sequence of five steps that will be explained in detail:

1. Locate the camera $\mathbf{C}_V$ in viewing coordinates.

2. Find $\mathbf{P}'_{1W}$ and $\mathbf{P}'_{2W}$ in world coordinates.

3. Find **VRP** in world coordinates.

4. Find the *up* vector, **v**.

5. Assemble the matrices and multiply them together to get the transformation.

Step 1: Locate the camera in viewing coordinates

A change of coordinates is an affine transformation that does not alter angles or lengths. Therefore, the angle $\mathbf{P}_{1W} \cdot \mathbf{C}_W \cdot \mathbf{P}_{2W}$ is the same as angle $\mathbf{P}'_{1V} \cdot \mathbf{C}_V \cdot \mathbf{P}'_{2V}$.

Equating the cosine of these angles and using the dot product form gives

$$\frac{(\mathbf{P}_{2W} - \mathbf{C}_W) \bullet (\mathbf{P}_{1W} - \mathbf{C}_W)}{\|\mathbf{P}_{2W} - \mathbf{C}_W\| \|\mathbf{P}_{1W} - \mathbf{C}_W\|} = \frac{(\mathbf{P}'_{2V} - \mathbf{C}_V) \bullet (\mathbf{P}'_{1V} - \mathbf{C}_V)}{\|\mathbf{P}'_{2V} - \mathbf{C}_V\| \|\mathbf{P}'_{1V} - \mathbf{C}_V\|} \tag{3-8}$$

There is just one unknown, z_{CV}, which refers to the position of the camera along the z-axis in viewing coordinates. Since both $\mathbf{P}'_{1V}$ and $\mathbf{P}'_{2V}$ have z-components equal to zero, the solution reduces to a quartic equation, which can be regarded as a quadratic in z^2_{CV}:

$$A z^4_{CV} + B z^2_{CV} + D = 0 \tag{3-9}$$

The equation (3-9) can be solved giving the solution, $\pm z^2_{CV}$. Taking the square root of the positive solution gives $\pm z_{CV}$. Since the viewing coordinate system is left-handed, the negative value of z_{CV} is used to define the camera position, $\mathbf{C}_V = (0, 0, z_{CV})$.

Step 2:Finding $\mathbf{P}'_{1W}$ and $\mathbf{P}'_{2W}$ in world coordinates

Knowing $\mathbf{C}_V$ defines the distances from the camera to the points $\mathbf{P}'_{1V}$ and $\mathbf{P}'_{2V}$. We also know the distance from the camera $\mathbf{C}_W$ to the points $\mathbf{P}_{1W}$ and $\mathbf{P}_{2W}$. Therefore, the ratio of these lengths can be found. Let these ratios be the parameters t and s in the following equations that specify $\mathbf{P}'_{1W}$ and $\mathbf{P}'_{2W}$ in world coordinates.

$$\mathbf{P}'_{1W} = t\,\mathbf{P}_{1W} + (1-t)\,\mathbf{C}_W \tag{3-10}$$

$$\mathbf{P}'_{2W} = s\,\mathbf{P}_{2W} + (1-s)\,\mathbf{C}_W \tag{3-11}$$

where $$t = \frac{\left\| \mathbf{P}'_{1V} - \mathbf{C}_V \right\|}{\left\| \mathbf{P}_{1W} - \mathbf{C}_W \right\|}, \tag{3-12}$$

and $$s = \frac{\left\| \mathbf{P}'_{2V} - \mathbf{C}_V \right\|}{\left\| \mathbf{P}_{2W} - \mathbf{C}_W \right\|}. \tag{3-13}$$

Step 3:Finding **VRP** *and* **n**

From the image we know the distance from **VRP** to $\mathbf{P}'_{1V}$, which is the length 'a' in Figure 3-17. Similarly, the distance from **VRP** to $\mathbf{P}'_{2V}$ is the length 'b', and the distance from **VRP** to the camera $\mathbf{C}_V$ is 'c' (or $\left| z_{CV} \right|$).

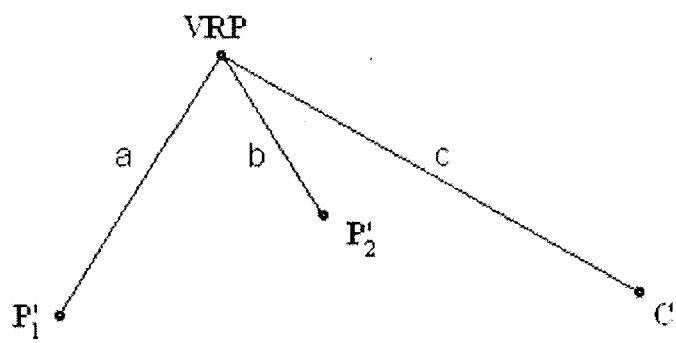

Figure 3-17: Find VRP.

Knowing the three distances, and the three points in world coordinates allows us to define **VRP** by solving three equations:

$$\left\| \mathbf{P}'_{1W} - \mathbf{VRP} \right\| = a \tag{3-14}$$

$$\left\| \mathbf{P}'_{2W} - \mathbf{VRP} \right\| = b \tag{3-15}$$

$$\left\| \mathbf{C}_W - \mathbf{VRP} \right\| = \left| z_{CV} \right| \tag{3-16}$$

Newton's method can be used to solve the 3×3 non-linear system, $F(\mathbf{x}) = 0$. Here, $\mathbf{x} = (x_1, x_2, x_3)$ is initially an approximation and converges on **VRP** with each iteration of the method.

Once the **VRP** has been calculated, we obtain the vector **n** as

$$\mathbf{n} = \frac{\mathbf{VRP} - \mathbf{C}_W}{\| \mathbf{VRP} - \mathbf{C}_W \|} \tag{3-17}$$

Step 4:Find the vector **v**

In viewing coordinates we can find the point where the line through $\mathbf{P}'_{1V}$ and $\mathbf{P}'_{2V}$ crosses the $\mathbf{u} = \mathbf{0}$ plane. Let this point be $\mathbf{Q}_V$. In the viewing plane $\mathbf{u} = \mathbf{0}$ corresponds to the vertical line through the centre of the image (see Figure 3-18). If possible, pick $\mathbf{P}_{1W}$ and $\mathbf{P}_{2W}$ so that $\mathbf{P}'_{1V}$ and $\mathbf{P}'_{2V}$ are placed at approximately equal distances on either side of the vertical centre-line of the image to obtain maximum accuracy. The point **Q** is defined by the parameter q, which expresses $\mathbf{Q}_V$'s distance from $\mathbf{P}'_{1V}$ as a multiple of the vector $\mathbf{P}'_{2V} - \mathbf{P}'_{1V}$. Only the u-coordinates of $\mathbf{P}'_{1V}$ and $\mathbf{P}'_{2V}$ are needed to find the ratio q.

In viewing coordinates

$$q = \frac{-\mathbf{P}'_{1Vu}}{(\mathbf{P}'_{2Vu} - \mathbf{P}'_{1Vu})} \tag{3-18}$$

In world coordinates

$$\mathbf{Q}_W = \mathbf{P}'_{1W} + q(\mathbf{P}'_{2W} - \mathbf{P}'_{1W}) \tag{3-19}$$

Knowing $\mathbf{Q}_W$ and **VRP** gives **v** as

$$\mathbf{v} = \frac{\mathbf{VRP} - \mathbf{Q}_W}{\| \mathbf{VRP} - \mathbf{Q}_W \|} \tag{3-20}$$

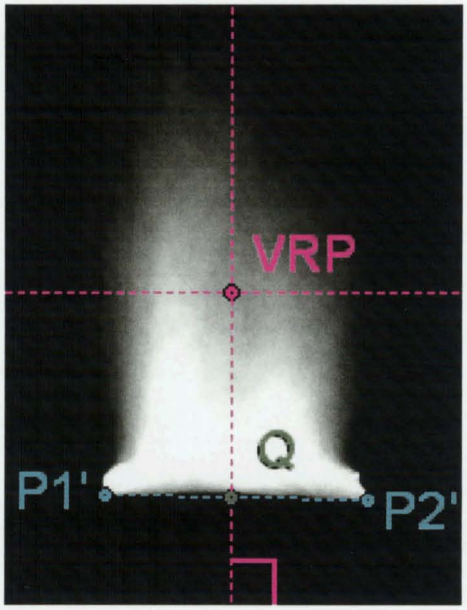

Figure 3-18: Locate the point Q.

Note: This method of finding the point **Q** will fail if $\mathbf{P}'_{1V}$ and $\mathbf{P}'_{2V}$ lie on the same vertical line in the image.

The vector **u** is then: $\mathbf{u} = \mathbf{n} \times \mathbf{v}$ (3-21)

Step 5:Assemble the matrices and produce the transformation

The elements of the VRP define the translation matrix T according to equation (3-4), the elements of u, v and n define the rotation matrix R according to equation (3-5), and the distance of the camera from the VRP, z_{CV}, defines M_{scale} as given in equation (3-7).

The combined transformation matrix $M_{combined}$, that converts 3D world coordinates to 2D image coordinates, is given by

$$M_{combined} = M_{scale} \cdot R \cdot T \tag{3-22}$$

The point cloud – a 3D field of flame probabilities

Figure 3-19b shows a point cloud resulting from perspective minima reconstruction from two orthogonal views. The point cloud is rendered from the viewpoint that corresponds to the camera position that recorded the video from which the averaged image in Figure 3-19a was produced. This visualization was realized using the OpenGL graphics library, called from LabVIEW. The values of each point represent flame probabilities and are in the range (0, 1], since all points with value zero have been removed. In this visualisation, points where the flame exists with probability 100% are also 100% opaque. Opacity then decreases as probability decreases making it easier to view the interior of the flame.

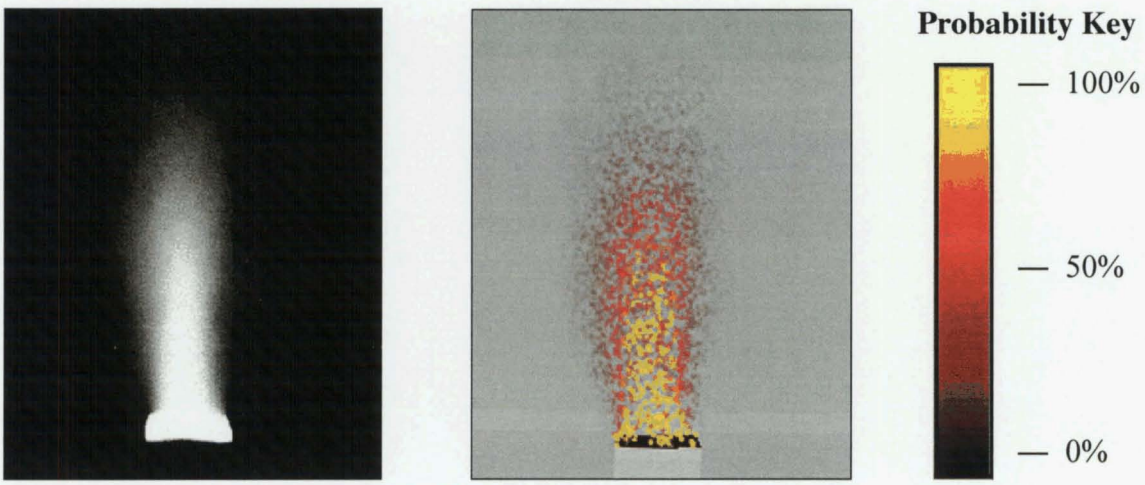

(a) Averaged image (b) Point cloud

Figure 3-19: Producing a point cloud.

3.4.2 Finding surfaces of constant flame probability

Flame probabilities have been determined at the points in the cloud that fills the reconstruction space. From this 3D field of values, we now wish to extract surfaces of constant probability. We considered both *Marching Cubes* and *Radial Basis Functions* to determine these isosurfaces. Radial Basis Functions were chosen because they were more convenient.

3.4.2.1 *What is a Radial Basis Function (RBF)?*

RBFs are density functions and, in our case, they relate the probability of a flame occurring to points in 3D space. All our work with RBFs was facilitated by the *FastRBF Toolbox* [3], which is a library of functions related to the fitting and evaluating of radial basis functions.

RBFs have been employed in a large number of areas, including geophysics, hydrology and signal processing [2]. Their wide application is largely due to the mild conditions placed on the location of data points and, usually, results are better than competing techniques [3]. Points are not required to lie on a regular grid and the FastRBF Toolbox requires only that the data are not linearly dependent.

An RBF is a function of the form

$$s(\mathbf{x}) = p(\mathbf{x}) + \sum_{i=1}^{N} \lambda_i \Phi(\mathbf{x} - \mathbf{x}_i), \tag{3-23}$$

where:

s = the *radial basis function* (RBF for short),

p = a low degree polynomial, typically linear or quadratic,

λ_i's = the RBF *coefficients*,

Φ = a real valued function called the *basis function*,

$\mathbf{x}_i$'s = the RBF *centres*.

FastRBF uses a *surface following tetrahedral* isosurfacer, which has $\vartheta(n^2)$ computation time rather than marching cubes' $\vartheta(n^3)$ [3]. The tetrahedral lattice also ensures a more even spatial sampling, and the built-in mesh optimisation improves the aspect ratio of triangles. These features are an advantage when calculating heat flux from the resulting surfaces and are discussed in Chapter 4. Notes on using the FastRBF Toolbox are included in Appendix D.

3.4.3 Determining heat flux

The following assumptions are made concerning the radiative properties of the flame.

3.4.3.1 *Assumptions*

- *The flame is a Diffuse Emitter*. The intensity of emissions is independent of direction and is uniform over a hemisphere.
- *The flame is a Gray Body*. The intensity of emissions does not vary with wavelength. In other words, the total energy is considered.
- *Transmissivity is 1*. This is justified by considering that the products of combustion are removed from the laboratory by an extractor fan and therefore cannot affect the transmissivity of the intervening atmosphere. We also assume that the absorption in certain spectral bands by water vapour and carbon dioxide does not significantly diminish the total transmitted radiation.
- *Emissivity is 1*. This is an initial assumption made for the sake of simplicity. The effect this has on the accuracy of heat flux predictions is not known at the outset, so the assumption is reviewed during the course of the investigation.

Using these assumptions, equation (1-3) becomes

$$I = \sigma T^4 F \tag{3-23}$$

3.4.3.2 *Calculating the Shape Factor*

The FastRBF Toolbox can export an isosurface as a VRML file. As an example, Figure 3-20 shows a VRML representation of a flame surface as it is viewed with a browser.

Figure 3-20: Triangulated flame surface.

These triangles are the area elements dS_i referred to in equation (2-21) and are defined in a VRML file as an *IndexedFaceSet.* An IndexedFaceSet first lists all the points, followed by the indices that link these points to make triangles (or faces). Figure 3-21 gives an example of a VRML2.0 text file:

```
#VRML V2.0 utf8
   :
Shape {
      :
   geometry IndexedFaceSet {
   #
   # 13064 points:
   #
      coord Coordinate {
      point [
         102.528 437.874 289.871,
         95.953 447.634 289.237,
         88.9566 437.692 289.251,
            :
         -129.25 1.62554 -167.094 ]
   }
   #
   # 25804 faces:
   #
      coordIndex [
      0, 3, 4, -1,
      0, 4, 5, -1,
      0, 5, 6, -1,
         :
```

Figure 3-21: VRML2.0 file showing an IndexedFaceSet.

In computer graphics the convention is that polygons whose vertices appear in a counter-clockwise (CCW) order are, by default, called *front facing* [38]. The polygon's normal vector (or *normal*, for short) is perpendicular to the surface of the polygon and is on the front-facing side. For example, the points of Figure 3-22 must be indexed 0, 1, and 2 for the triangle to appear facing as it does in the diagram. Since the normal defines the orientation of its surface, it is used to help decide if and how much a triangle contributes to the shape factor.

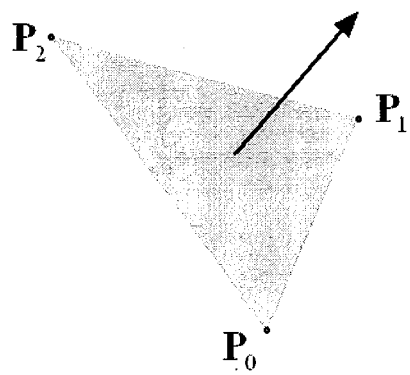

Figure 3-22: CCW triangle with normal vector.

From equation (2-21) we can consider the contribution to the total shape factor of a single triangle on the flame surface as:

$$dF_{dS \to dT} = \frac{\cos\theta_S \cos\theta_T}{\pi r^2} dS \tag{3-24}$$

Evaluating this requires the following information:

1. dS = the area of the triangle,
2. r = the distance from the target to the centroid of the triangle,
3. θ_S = the angle between the triangle's normal and the vector directed along the line connecting the triangle to the target,
4. θ_T = the angle between the target's normal and the vector directed along the line connecting the target to the triangle.

Methods for determining these quantities are provided as follows [7]:

Area

The area of the triangle, and its normal, can be obtained from the cross product of the vectors **u** and **v** that form two sides of the triangle. Referring to the illustration in Figure 3-22, these vectors are found thus:

$$\mathbf{u} = (u_x, u_y, u_z) = \mathbf{P}_1 - \mathbf{P}_0 = (P_{1x} - P_{0x}, P_{1y} - P_{0y}, P_{1z} - P_{0z}) \tag{3-25}$$

$$\mathbf{v} = (v_x, v_y, v_z) = \mathbf{P}_2 - \mathbf{P}_0 = (P_{2x} - P_{0x}, P_{2y} - P_{0y}, P_{2z} - P_{0z}) \tag{3-26}$$

Their cross product is

$$\mathbf{u} \times \mathbf{v} = (u_y v_z - u_z v_y,\ u_z v_x - u_x v_z,\ u_x v_y - u_y v_x) \tag{3-27}$$

The triangle's normal vector $\hat{\mathbf{n}}_S$ is the normalised cross product

$$\hat{\mathbf{n}}_S = \frac{\mathbf{u} \times \mathbf{v}}{\|\mathbf{u} \times \mathbf{v}\|} = \frac{(u_y v_z - u_z v_y,\ u_z v_x - u_x v_z,\ u_x v_y - u_y v_x)}{\left[(u_y v_z - u_z v_y)^2 + (u_z v_x - u_x v_z)^2 + (u_x v_y - u_y v_x)^2\right]^{\frac{1}{2}}} \tag{3-28}$$

The triangle's area is half the magnitude of the cross product

$$dS = \frac{\|\mathbf{u} \times \mathbf{v}\|}{2} = \frac{\left[(u_y v_z - u_z v_y)^2 + (u_z v_x - u_x v_z)^2 + (u_x v_y - u_y v_x)^2\right]^{\frac{1}{2}}}{2} \tag{3-29}$$

Distance

Let the position of the target be given by $\mathbf{T} = (T_x, T_y, T_z)$, and let the target's orientation be specified by the normal $\hat{\mathbf{n}}_T = (n_{Tx}, n_{Ty}, n_{Tz})$. Also, let **S** be the centroid of the triangle, which is given by the average of the triangle's three vertices.

$$\mathbf{S} = (S_x, S_y, S_z) = \tfrac{1}{3}(\mathbf{P}_0 + \mathbf{P}_1 + \mathbf{P}_2)$$

$$= \tfrac{1}{3}(P_{0x} + P_{1x} + P_{2x},\ P_{0y} + P_{1y} + P_{2y},\ P_{0z} + P_{1z} + P_{2z}) \qquad (3\text{-}30)$$

The distance, r, between the target and the triangle is defined as the magnitude of the vector from the target to the centroid of the triangle.

The vector from the target to the triangle is

$$\mathbf{r} = (r_x, r_y, r_z) = \mathbf{S} - \mathbf{T} = (S_x - T_x, S_y - T_y, S_z - T_z), \qquad (3\text{-}31)$$

and the distance r is

$$r = \|\mathbf{r}\| = (r_x^2 + r_y^2 + r_z^2)^{\frac{1}{2}} \qquad (3\text{-}32)$$

Angles

To determine the values of $\cos\theta_S$ and $\cos\theta_T$ it is necessary to find the unit vectors, $\hat{\mathbf{r}}_{ST}$ and $\hat{\mathbf{r}}_{TS}$, that lie along the vector $\mathbf{r}$ and are directed from $\mathbf{S}$ to $\mathbf{T}$ and from $\mathbf{T}$ to $\mathbf{S}$ respectively.

$$\hat{\mathbf{r}}_{ST} = \left(\frac{T_x - S_x}{r}, \frac{T_y - S_y}{r}, \frac{T_z - S_z}{r}\right) \qquad (3\text{-}33)$$

$$\hat{\mathbf{r}}_{TS} = \left(\frac{S_x - T_x}{r}, \frac{S_y - T_y}{r}, \frac{S_z - T_z}{r}\right) \qquad (3\text{-}34)$$

Using that the dot product of unit vectors gives the cosine of the angle between them, therefore:

$$\cos\theta_S = \hat{\mathbf{r}}_{ST} \cdot \hat{\mathbf{n}}_S = \frac{n_{Sx}(T_x - S_x)}{r} + \frac{n_{Sy}(T_y - S_y)}{r} + \frac{n_{Tz}(T_z - S_z)}{r} \qquad (3\text{-}35)$$

$$\cos\theta_T = \hat{\mathbf{r}}_{TS} \cdot \hat{\mathbf{n}}_T = \frac{n_{Tx}(S_x - T_x)}{r} + \frac{n_{Ty}(S_y - T_y)}{r} + \frac{n_{Tz}(S_z - T_z)}{r} \qquad (3\text{-}36)$$

Visibility

The surface element must be visible from the target and the target must be visible from the surface element for it to contribute to the shape factor. This requires that both $\cos\theta_S > 0$ and $\cos\theta_T > 0$, else the contribution is zero.

3.4.3.3 *Calculating the heat flux*

Since the receiving target is assumed to be at room temperature (20°C) and the source of a continuous flame region is around 900°C [21], observe that:

$$\frac{T_S^4 - T_T^4}{T_S^4} = \frac{1173^4 - 293^4}{1173^4} \approx 0.9961 \tag{3-37}$$

Therefore, ignoring the energy emitted from the target and received at the flame introduces an error of about 0.4%. Since this is considered to be negligible, equation (2-22) is simplified so that the *net* radiation from the flame to the target is approximated as:

$$Q'_{S\to dT} = \sigma T_S^4 \sum_{i=1}^{N} \frac{\cos\theta_{S_i} \cos\theta_{T_i}}{\pi r_i^2} dS_i \ [\mathrm{W/m^2}] \tag{3-38}$$

3.4.4 Determining the thermal radiation field

To determine a thermal radiation field in a region it is necessary to know the heat flux values at all points contained therein. Since the heat flux values comprise a density field, it is suitable for representation by a radial basis function. This is done similarly to the way we represented a flame from a field of probabilities.

3.4.4.1 *Maximum Shape Factor*

During validation, heat flux values are calculated at gauge positions using the known orientation of each gauge. When constructing a thermal radiation field it is important to find, at each point, the orientation that provides the maximum shape factor. Then, since emission is assumed to be uniform throughout the surface, this orientation will be subjected to the maximum incident heat flux for that location. This has been done using the method proposed by Hankinson [7].

For a given target, let F_{MAX} be the maximum shape factor, and let $\hat{\mathbf{n}}_{MAX}$ be the orientation that yields F_{MAX}. Then the shape factor for a particular location and orientation of target can be related to F_{MAX} at the same position by

$$F = F_{MAX} \cos\Phi, \tag{3-39}$$

where Φ is the angle between a particular orientation and the orientation that provides F_{MAX} for the given target.

This is true on the condition that the plane surface containing the target does not intersect the radiating surface. If it does, this equation does not hold because F is calculated using only that part of the surface that is visible from the target. However, if there are no restrictions placed on the field-of-view of the target then a quantity F^* is found that makes equation (3-39) true in all situations. Therefore, F^* places no conditions on $\cos\theta_T$ but still requires that $\cos\theta_S > 0$.

F^* can be considered to be a component of F_{MAX}. If F^* is calculated for three mutually orthogonal directions, say the x, y and z-axes of the coordinate system, then the magnitude F_{MAX} and the direction $\hat{\mathbf{n}}_{MAX}$ can be established.

$$F_{MAX} = \left(F_x'^2 + F_y'^2 + F_z'^2\right)^{\frac{1}{2}} \tag{3-40}$$

$$\hat{\mathbf{n}}_{MAX} = \left(\frac{F_x'}{F_{MAX}}, \frac{F_y'}{F_{MAX}}, \frac{F_z'}{F_{MAX}}\right) \tag{3-41}$$

3.4.4.2 *Constructing a Thermal Radiation Field*

A cloud of points is initialised in the region surrounding the flame. The accuracy of shape factor calculations, which is discussed in Chapter 4, is prone to error if the target is very close to the flame surface. For this reason it is advisable to add a suitable margin on all sides of the flame and keep this region clear of points. This also ensures that no points are initialised within the flame, where calculations will yield a false shape factor value since nearly all surface elements will not satisfy the requirement $\cos\theta_S > 0$.

Once the cloud has been initialised, the maximum shape factor is found for each point using the method previously described. Points on the surface of the flame are added to the cloud and their shape factors are set to one. These points will allow the RBF to interpolate the region close to the flame where shape factor data is not provided.

3.4.4.3 *Extracting a Heat Flux Isosurface*

An RBF is fitted to the shape factor data using the commands outlined in Appendix D. The resulting RBF is a function that defines the thermal radiation field by mapping any 3D point within the region to a shape factor value. The equation, $Q = \sigma T^4 F$, relates shape factors to heat flux values. The constant in this linear relationship, σT^4, is provided by experimental data. Extracting an isosurface with a specific heat flux value requires the corresponding shape factor value for use with FastRBF's *–threshold* argument. This shape factor value is given by

$$F = \frac{Q}{\sigma T^4} \tag{3-42}$$

Chapter 4

Application to a Diffusion Burner (Controlled Flame)

In this chapter the techniques for data collection and analysis presented in Chapter 3 are applied to an experiment using a diffusion burner. The objective is to see if the proposed model correctly predicts heat flux.

4.1 Experiment

4.1.1 Background

The burns were performed at the Fire Laboratory at the University of Canterbury. A plan of the Fire Laboratory appears in Figure 4-1. The laboratory has two observation windows, one facing the garage and one facing the control room. Henceforth, these directions will be referred to as the *front* and the *side* respectively as labelled in the diagram. Most of the reconstructions were done with two cameras pointing in orthogonal directions using views from the front and the side.

The focus of this chapter is on an experiment performed on the July 29, 2002. In this experiment heat flux data were recorded at 96 locations and video was recorded from six camera positions.

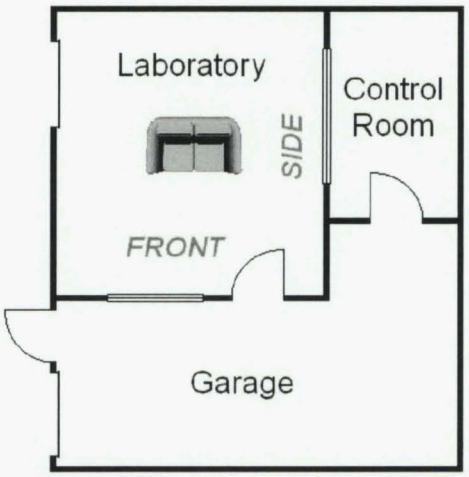

Figure 4-1: Diagram of the laboratory floor plan.

The dimensions of the diffusion burner were 300mm × 600mm. The burner was placed near the centre of the laboratory and aligned so the longer, 600mm, side of the burner faced the front. The supply of propane was set to produce a heat release rate of 150 kW. This was the largest flame we could use without losing sight of the flame tips in the cameras' fields of view. At this flame size we could comfortably work in the laboratory and place the cameras where we wished without them being at risk. Two trolleys were set on rails that were directed towards the front and side of the flame respectively. Heat flux gauges were attached to each trolley. The height of the gauges could be adjusted on the trolley, and the trolley could be moved horizontally (see Figure 4.2).

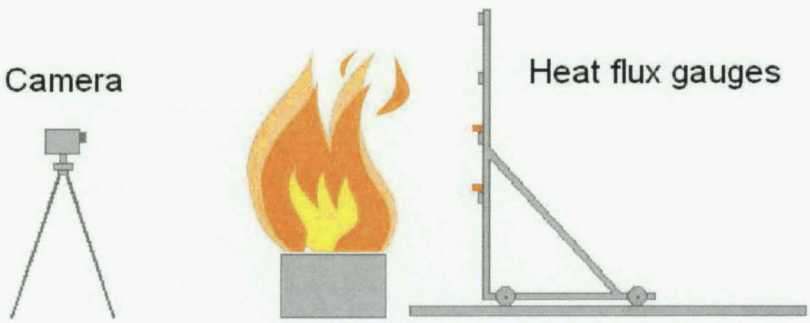

Figure 4-2: Fire laboratory set-up.

A coordinate system was established with the origin set at the centre of the base of the flame, which may also be described as the centre of the top of the diffusion burner. The

direction of positive x was towards the side, the direction of positive z was towards the front, and the direction of positive y was vertically upwards. This constitutes a right-handed coordinate system as illustrated in Figure 3-3. Millimetres were chosen as the basic unit of measurement for the laboratory and the virtual space where the flame is reconstructed.

4.1.2 Video

A single Canon Elura, which is a standard commercial CCD camera, was used to record this burn.

4.1.2.1 *Camera placement*

Camera positions outside the laboratory introduced reflections to the image from the window through which the burn was observed. These positions also required care to ensure the window frame did not obscure part of the flame.

While filming from inside the laboratory, the cameras were constrained to be less than three metres from the centre of the flame. At this distance, with the *zoom* set to obtain the widest possible field of view, it was still difficult to capture the entire flame.

Ideally, the video and the heat flux data ought to be recorded simultaneously. However, when attempting this, the trolley upon which the heat flux gauges were mounted obscured the camera's view of the flame. Placing the camera on the side of the fire opposite the heat flux gauges was considered. The symmetry of the controlled flame makes this option possible. This could not be done however because, after positioning the gauges on one side of the fire, there was not enough distance on the opposite side to place the camera so that it could capture the entire flame.

This meant that video data from the different camera positions were not recorded simultaneously. This has implications that will be discussed at the end of the chapter.

Figure 4-3 illustrates a plan view of the six camera positions. Rather than shift the camera to every position, the camera was placed at two positions and the burner was rotated to provide the other orientations. For example, the camera was placed at 0° (the side) and then views equivalent to the 22.5° and 45° positions were obtained by rotating the diffusion burner counter-clockwise while the camera remained at 0°. Similarly, the camera was placed at 90° (the front) and then views equivalent to the 112.5° and 135° positions were obtained by rotating the diffusion burner counter-clockwise by 22.5° and 45° respectively.

Camera positions in the laboratory were as far from the flame as possible, although constrained by our desire to have all camera positions equidistant from the centre of the base of the flame (the origin). The side camera was the limiting factor and set the distance for all other cameras by being against the wall at a distance of 2950mm.

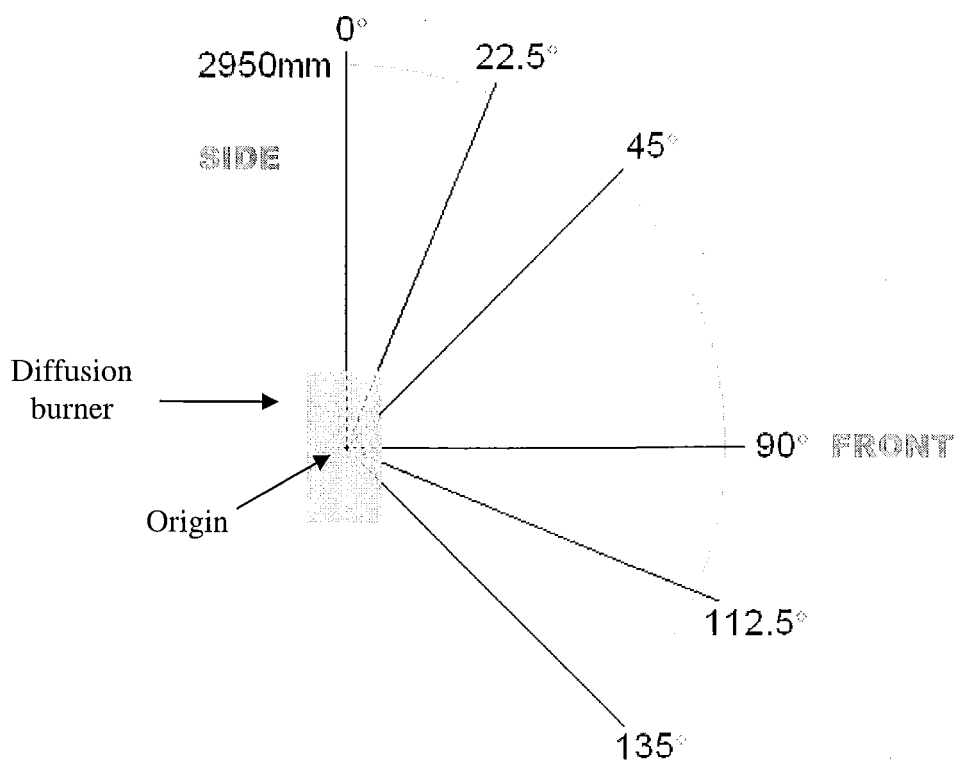

Figure 4-3: Plan view of camera positions.

In an effort to reduce potential errors due to perspective reconstruction, the height of the camera was set to be approximately mid-way between the base of the flame and the flame tip. Estimating the height of the flame to be approximately 1400mm, the camera height was set to be 700mm above the base of the flame.

Each camera position was specified in terms of the coordinate system described in *4.1.1 Background*. The coordinates of the camera positions are shown in Table 4-1:

Position	Coordinates
Side – 0°	(2950, 700, 0)
22.5°	(2725, 700, 1129)
45°	(2086, 700, 2086)
Front – 90°	(0, 700, 2950)
112.5°	(−1129, 700, 2725)
135°	(−2086, 700, 2086)

Table 4-1: Camera positions.

From each camera position at least six seconds of video was recorded in accordance with the findings of section *3.3.3.3 Determining the averaging period.*

4.1.3 Measuring heat flux

4.1.3.1 *Heat flux gauges*

The University of Canterbury provided four Gardon heat flux gauges for this experiment and their specifications appear in Table 4-2. This calibration information is necessary to convert the experimental data, recorded in milli-volts, to heat flux values with units of kilowatts per square metre.

Heat Flux Gauges	
Serial #	Calibration
124111	20.30 mV @ 100 kW/m^2
124112	19.23 mV @ 100 kW/m^2
124113	19.20 mV @ 100 kW/m^2
1241114	18.33 mV @ 100 kW/m^2

Table 4-2: Heat flux gauge specifications.

Heat flux gauges have one of two basic shapes – a flat, surface-attached, layered wafer (thermopile) or an insert-style cylinder. Cylinder type gauges are generally not as sensitive as the wafer type but can withstand higher operating temperatures and are more easily water-cooled [33]. The University of Canterbury's Gardon gauges are water-cooled, cylinder type gauges. Appendix E contains more information on cylinder type heat flux gauges.

4.1.3.2 *Gauge Positions*

The gauges were placed in the direction of the camera positions (see Figure 4-4). Since the trolleys upon which the gauges were mounted travel from the centre of the burner towards the side (0°) and towards the front (90°), data for the other orientations was gathered in the same way as the video data by rotating the burner. In each direction data was recorded at 16 points forming a regular grid in a vertical plane (see Figure 4-5). The horizontal spacing of the columns was 300mm, beginning at a distance of 600mm from the origin and ending at 1500mm as shown in Figures 4-4 and 4-5.

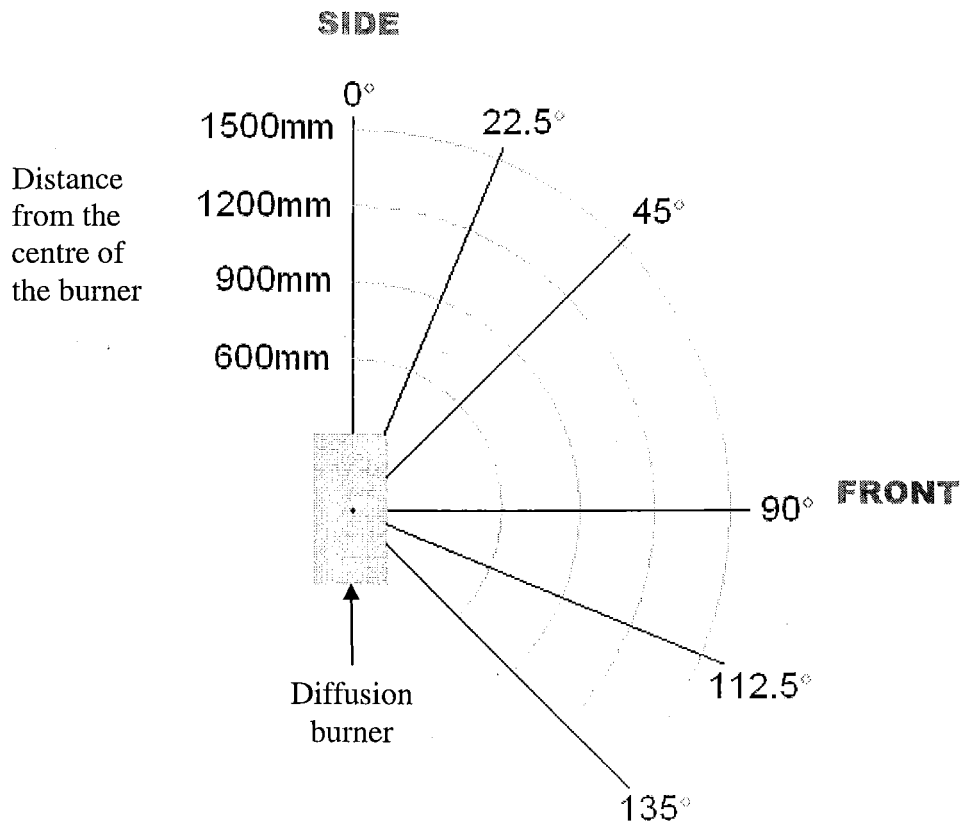

Figure 4-4: Plan view of heat flux gauge positions.

The horizontal spacing of the rows was also 300mm, beginning at a height of 300mm above the origin and ending at 1200mm as shown in Figure 4-5. The arrows in Figure 4-5 indicate that the orientation of the heat flux gauges is horizontal and they are directed towards the centre of the burner.

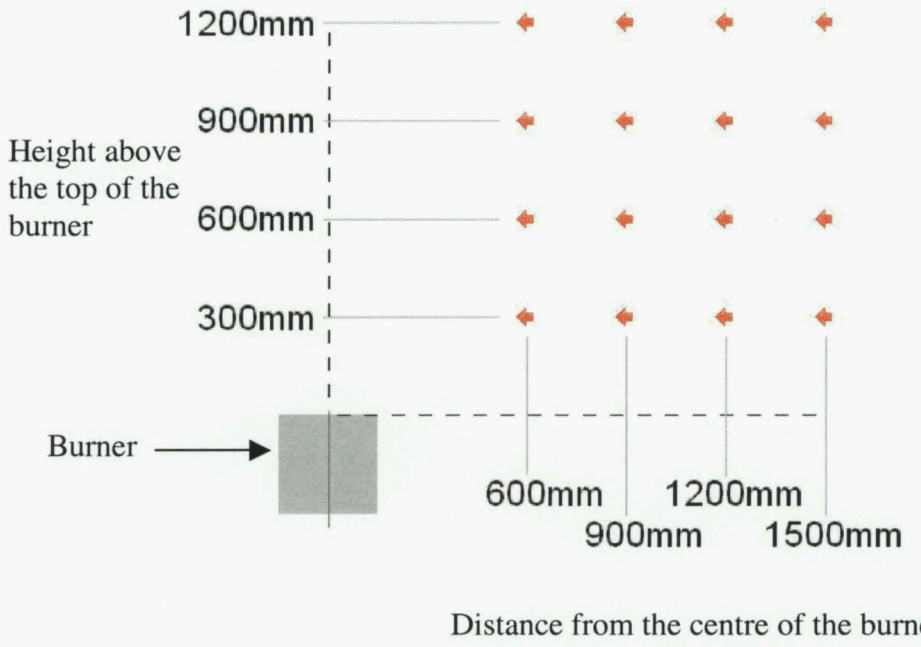

Figure 4-5: Heat flux gauge positions make up a grid in a vertical plane.

4.1.3.3 *Recording the Heat Flux Data*

A value is sampled from each gauge at a rate of 1Hz. The data was recorded in two runs. For the first run, gauges 124111 and 124113 were placed in front of the burner (90°) at heights 900mm and 1200mm respectively above the top of the burner. Gauges 124112 and 1241114 were put to the side of the burner (0°) also at heights 900mm and 1200mm respectively above the top of the burner. For the second run, the gauges were adjusted to heights 300mm and 600mm above the top of the burner. During each run the data were recorded continuously while moving the trolleys and rotating the burner at the prescribed time intervals, which were four minutes. Four minutes was chosen because it allowed us to retain two minutes of reliable data after discarding the first and the last minutes. Discarding this data was done to ensure the flame system had regained equilibrium at the new operating conditions after each transition of either the trolleys or the burner.

After initially running the fire for a few minutes to reach stable operating conditions, the first run of data collection was carried out in the following manner:

1. Data logging begins at time zero with the gauges at a distance of 600mm from the centre of the flame.

   - At 4 minutes, while still logging data, the gauges are shifted to a distance of 900mm from the centre of the flame.
   - At 8 minutes, the gauges are shifted to 1200mm from the centre of the flame.
   - At 12 minutes, the gauges are shifted to 1500mm from the centre of the flame.

2. At 16 minutes, the burner is rotated to an angle of 22.5°.

   - At 20 minutes, the gauges are shifted to 1200mm from the centre of the flame.
   - At 24 minutes, the gauges are shifted to 900mm from the centre of the flame.
   - At 28 minutes, the gauges are shifted to 600mm from the centre of the flame.

3. At 32 minutes, the burner is rotated to an angle of 45°.

   - At 36 minutes, the gauges are shifted to 900mm from the centre of the flame.
   - At 40 minutes, the gauges are shifted to 1200mm from the centre of the flame.
   - At 44 minutes, the gauges are shifted to 1500mm from the centre of the flame.

4. At 48 minutes, data logging is stopped.

The second run was organised in the same way, except that the burner begins at a 45° angle and the gauges begin at a distance 1500mm from the centre of the flame, since that was the set-up at the end of the first run.

All data logged during the burn was written to a file of comma-separated values (CSV). A sample of the raw data file appears in Table 4.3. Time appears in the first column and the next four columns contain gauge data.

Paul Mason's Experiment using 150 kW burner

C:\UDL2\FLUX1.CSV

########

	1	2	3	4
	MV	mV	mV	mV
47:00.4	0.532	0.42	0.364	0.308
47:01.4	0.448	0.392	0.336	0.28
47:02.5	0.448	0.28	0.28	0.308
47:03.6	0.56	0.392	0.42	0.364

Table 4-3: Excerpt from the heat flux gauge data file.

4.2 Analysis

4.2.1 Image processing

The objective is to produce, for each camera view, an image representing flame probability from which the 3D flame probability can be reconstructed. It was of particular interest to see how well a flame reconstruction from two orthogonal views predicts heat flux at points that were not located in the direction of a camera. For this reason just the side (0°) and front (90°) camera views were used.

4.2.1.1 *Capturing the Video*

The video was transferred from the camera to a PC via a *FireWire 1394* PCI interface card. After connecting the camera to the PC, the raw video is captured and saved as an uncompressed AVI file. These files can become very large. For example, here are the details of the raw video from the July 29 burn.

- File size: 277 MB
- Duration: 80.5 seconds
- Attributes: 24 Bits, 720×480
- Frame rate: 30 fps
- Audio: 16 Bit, Stereo, sampled at 32 kHz

The audio track is not required but no option was available to filter it out during capture. However, it can easily be discarded during subsequent video processing.

Exactly six seconds of video from each camera was saved as a new movie file. Since the movies are processed with LabVIEW, which utilizes a QuickTime Movie VI[5] library, the new movies are saved in QuickTime format. This is done with *Video only*

[5] In LabVIEW a program or subroutine is referred to as a Virtual Instrument (VI).

selected to remove the audio track, and without compression. The size of a six-second, uncompressed video clip was typically between 6.5 and 7 MB.

4.2.1.2 *Extract a Colour Plane*

In the July 29 experiment the video was recorded with the exposure adjusted manually to darken the image. This was because we were attempting to capture flame intensity information prior to reaching the conclusion that it was not possible. Therefore the video is dark, by comparison to later recordings, and thinner parts of the flame are barely visible. In these circumstances the HSL-Luminance plane was chosen because it provided best contrast between the flame and its surroundings. This allows our goal, which is to isolate the flame, to be more easily attained. Refer to Figure 4-6 for a comparison of the HSL-Luminance plane with the Blue colour plane.

(a) Frame (b) Blue plane (c) Luminance plane

Figure 4-6: Extract the HSL-Luminance plane.

4.2.1.3 *Thresholding and Filling Holes*

The threshold range that suits the July 29 video has a lower limit 130 and an upper limit of 255 as indicated on the histogram of pixel intensities shown in Figure 4-7.

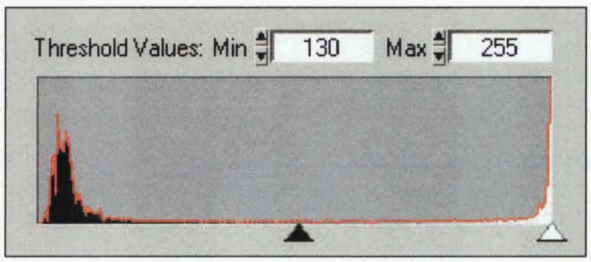

Figure 4-7: Histogram of an image showing the threshold values.

The video from the July 29 experiment was used in Chapter 3, Figure 3-4, to demonstrate filling holes. Figure 3-4c displays the results of its use. The section of LabVIEW code that achieves the image processing is given in Figure 4-8.

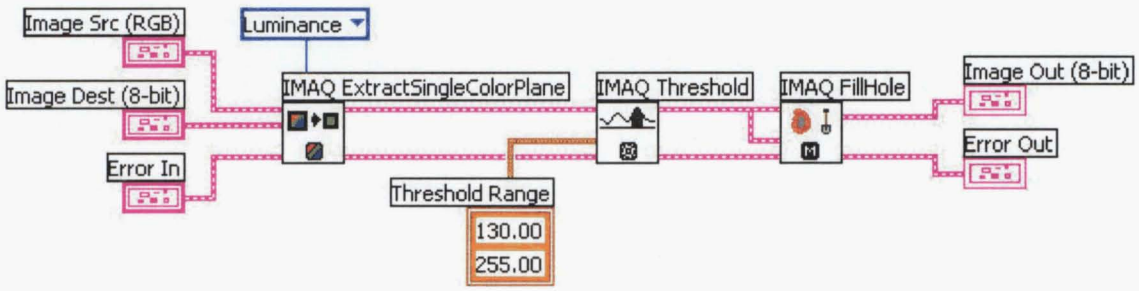

Figure 4-8: Image processing code for the experiment of July 29, 2002.

4.2.1.4 *Producing an Averaged Image*

Since we are dealing with 8-bit images, any pixel sum exceeding 255 is clipped to this value. To avoid overflow the 8-bit pixel arrays may be typecast to 32-bit integer arrays before calculating the average. Once the average has been calculated the result can be cast back to an 8-bit pixel array.

Using the findings of section *3.3.3.3 Determining the averaging period*, exactly six seconds of video were used to produce the averaged image. Since the Canon Elura records at 30 frames per second, this corresponds to 180 frames. The averages resulting from the front and side camera views are given in Figure 4-9.

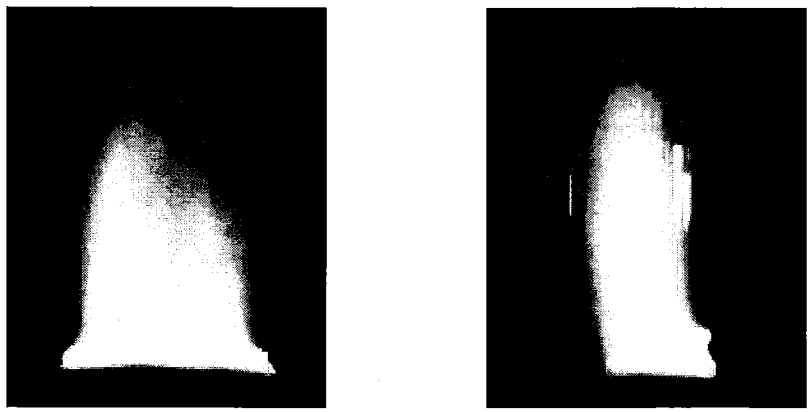

(a) Front (b) Side

Figure 4-9: Averaged images from July 29 experiment.

Notice that the side view contains light reflected from the sheet-metal wall of the room. It was not possible to separate the flame from such a bright background. Fortunately, this reflection did not appear to corrupt the shape of the reconstructed flame.

4.2.2 Flame reconstruction

4.2.2.1 *Producing a point cloud*

A random cloud of points was chosen for this reconstruction, although subsequent investigation suggests that a regular grid might have been better. Whatever the type of point cloud used, it is important to ensure that an adequate number of points are initialised in the reconstruction space.

Establishing Point Cloud Density

The example in Chapter 3 is taken from the July 29 experiment. Here the spacing of points was chosen to be at intervals of 5 pixels (28mm). It is necessary to verify that this estimate provides an acceptable sampling frequency.

For this purpose ROBOLAB's Butterworth Low Pass Filter was employed. Figure 3-12 shows a test pattern that repeats every 10 pixels, which is half our proposed sampling frequency of 5 pixels. In this example best results were obtained with cut-off distance $D_0 = 0.08$, and order $N = 3$. With image size 720×480, the distance from the centre to a corner is $\frac{1}{2}\sqrt{720^2 + 480^2} = 432.67$ pixels and hence $D_0 = 0.08 \times 432.67 = 34.61$ pixels. The order of the filter N, determines how frequencies are attenuated about the cut-off. Figure 4-10 shows that higher orders produce steeper slopes in the transfer function.

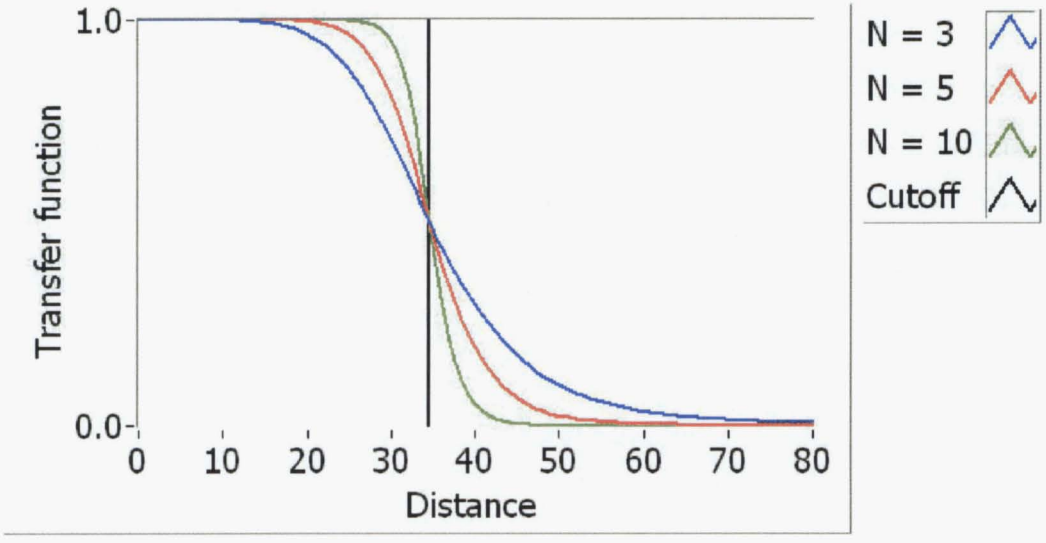

Figure 4-10: The effects of the order of the Butterworth filter.

The test pattern is not entirely removed in Figure 3-12b, which serves to illustrate that a compromise has occurred. On the one hand it is better to use lower orders to achieve a more gradual cut-off and hence reduce ringing effects, and on the other hand it is desirable to have an ideal filter that rejects all unwanted frequencies and admits all others. The test pattern was successfully removed using the parameters $D_0 = 0.10$ and $N = 6$, and $D_0 = 0.12$ and $N = 10$, however, these settings produced ringing effects in image space largely due to the higher orders used.

To better see the extent to which error was introduced by using a low pass filter, the high pass filter was obtained by inverting the mask of the low pass filter. Figure 4-11 shows the original image alongside the results of applying both low pass and high pass filters. Notice that the area containing high frequencies is very small. Based on this observation, it was decided not to apply a low pass filter to the averaged images before reconstruction, since any aliasing artefacts that might occur would occur over an insignificantly small area.

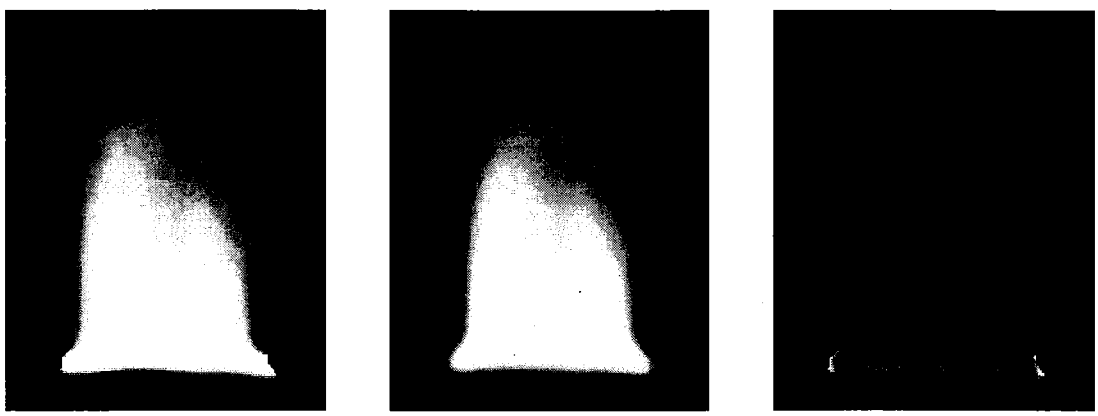

(a) Average image (b) Low pass filter (c) High pass filter

Figure 4-11: Using filters to establish the extent of error.

Establishing Point Cloud Boundaries

To be certain that the point cloud is established in a region that contains the entire flame, a suitable margin is added to all sides of the flame. The flame in Figure 4-12 has a base 600mm × 300mm. 100mm is added on all sides and the height of the flame is estimated to be no higher than 1200mm. This is acceptable for the front view, but the side view reveals the flame is leaning to the left, which is towards the front of the laboratory. Therefore, a margin of 200mm is used at the front. Figure 4-12 shows these boundaries. They are tilted slightly to compensate for the camera being off vertical. This is known because the burner, as indicated by the base of the flame, is horizontal and yet does not appear so.

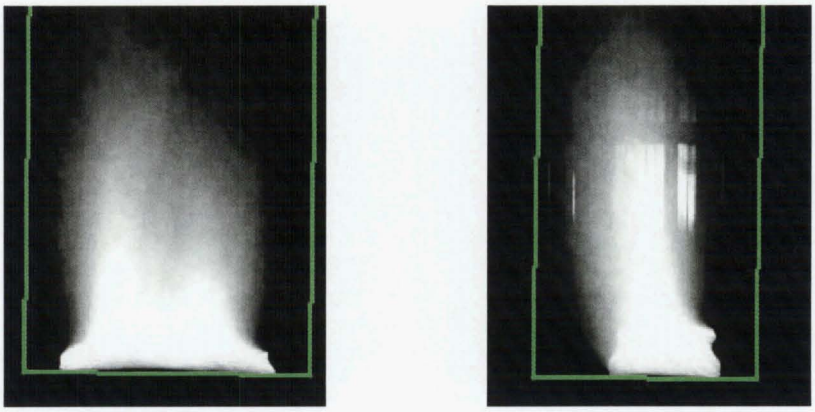

(a) Front view (b) Side view

Figure 4-12: Boundary of the reconstruction space.

Using a sampling rate that corresponds to regular grid intervals of 28mm, the number of points needed to fill this space is given by:

$$\text{Number of points required} = \text{width} \times \text{depth} \times \text{height} \div \text{interval}^3 \quad (4\text{-}1)$$

$$= 800 \times 600 \times 1200 \div 28^3 = 26{,}239$$

Therefore, we should fill this reconstruction space with at least 26,239 points to guarantee the proposed sampling rate. Figure 4-13 shows visualisations of a point cloud as a regular grid and as a set of random points. There are 26,239 points in the random set but, for simplicity, the number of points in the regular grid was decided in the following way:

Width / Interval = 800 / 28 = 28.57 $\cong$ 29

Depth / Interval = 600 / 28 = 21.43 $\cong$ 21

Height / Interval = 1200 / 28 = 42.86 $\cong$ 43

This yields a total of 26,187 points in the regular grid.

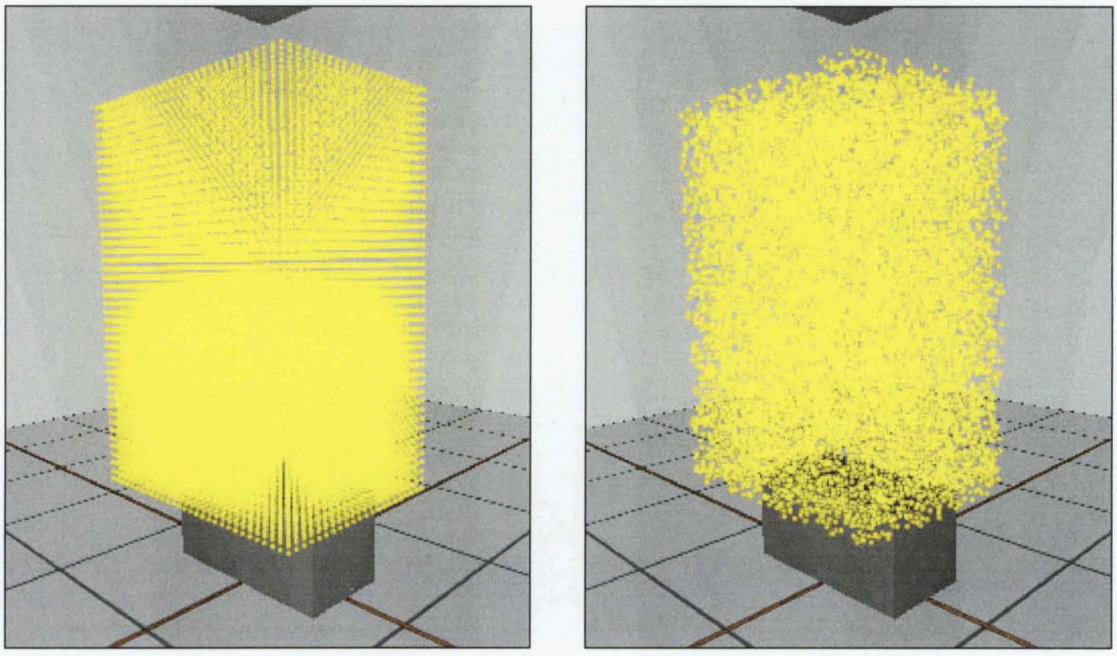

(a) Regular grid (b) Random points

Figure 4-13: Reconstruction space initialised with a suitable number of points.

Although in Chapter 3 we concluded that the choice between a regular grid and a random point set was arbitrary, Figure 4-13b indicates this may not be so. Figure 4-13b reveals that the cloud of random points does indeed have regions that are unsampled and appear as small "holes" visible around the edges of the cloud. It is reasonable to assume that similar such holes exist throughout the reconstruction space. Because of this observation, the regular grid of points was chosen for the reconstruction because it sets a lower bound on the sampling frequency.

4.2.2.2 *Minima reconstruction*

Six camera views were recorded for the July 29 experiment but the reconstruction was performed using just the front and side views. One reason for this is that, by the nature of minima reconstruction, adding projections further reduces flame probabilities and reduces the effective flame size. This would not pose a problem if all camera views were recorded simultaneously and exactly the same flame appeared in each. Registration errors involved in projections can also reduce the effective flame size. As these errors increase and the flame reconstruction degrades, the ability to calculate accurate shape factors also diminishes. This topic is discussed further in Chapter 6.

The two averaged images were projected back through the reconstruction space using the Minima Reconstruction technique as described in section *3.4.1.7*.

With a controlled flame such as the diffusion burner used in this experiment, we are able to improve the reconstruction by taking advantage of flame symmetry. The *Front* view can be flipped horizontally to get a *Back* view. Similarly, the *Side* (Right) view can be flipped horizontally to get a *Left* view. Projecting the Back and Left views in addition to the Front and Side views reduces the perspective error in the reconstruction. See Figure 4-14 for an illustration of this.

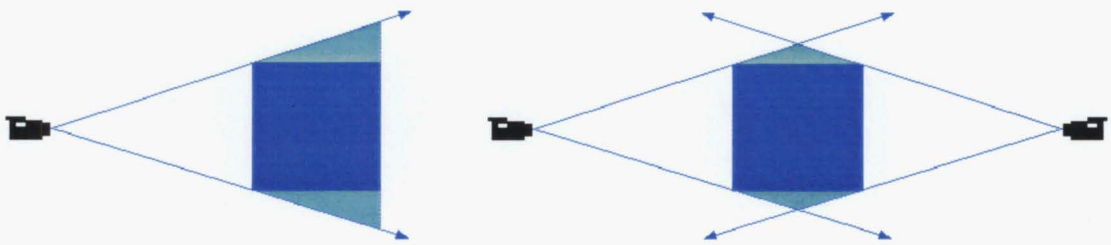

(a) One sided projection. (b) Two sided projection.

Figure 4-14: Two sided projections minimize error.

Figure 4-15 shows the point cloud resulting from Minima reconstruction. After reconstruction, there were 17,871 points remaining in the regular grid.

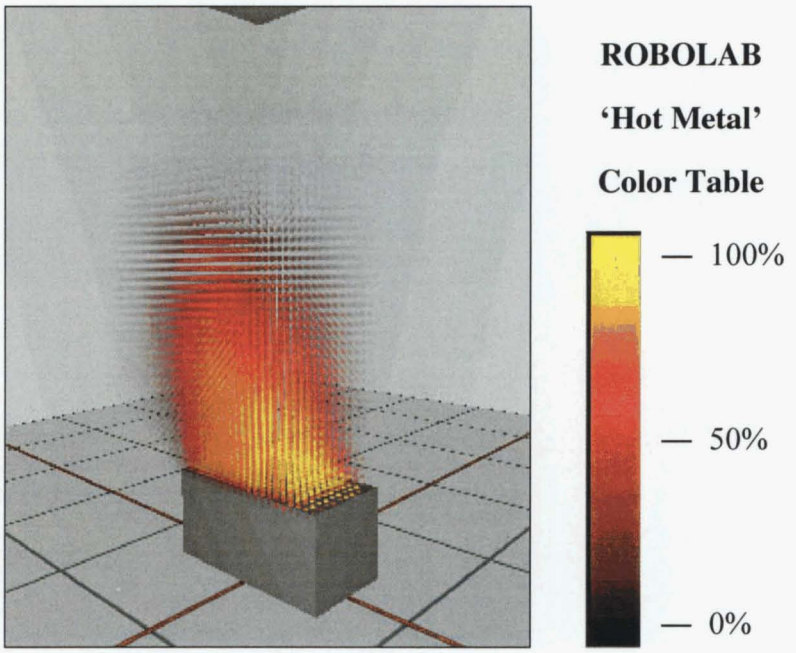

Figure 4-15: 3D flame probabilities assigned with Minima reconstruction.

4.2.2.3 *Fitting and Evaluating an RBF*

The FastRBF Toolbox was used to fit a radial basis function to the point cloud data and extract a surface of constant flame probability. Notes on the sequence of commands used can be found in Appendix D. Generally, it is recommended to remove (near) identical points from the data set since they cannot be handled by the RBF fitter. However, (near) identical points do not exist in a regular grid. The 25% surface was extracted and exported as a VRML file. This surface comprises 25,752 area triangles and is shown in Figure 4-16.

Figure 4-16: The 25% surface extracted from the regular point cloud.

This surface was evaluated with a resolution of 10, which yielded a mesh consisting of 13,039 points and 25,752 triangles.

4.2.3 Finding a relationship between recorded heat flux data and shape factors

Using flame surfaces extracted from the RBF, shape factors were calculated (section 3.4.3.2) for the same locations and orientations as the heat flux gauges used in the experiment. Recorded heat flux and calculated shape factors were correlated for five different flame surfaces. These five surfaces were extracted with threshold values equivalent to 95%, 75%, 50%, 25%, and 10%. The strength of these surfaces as a predictor of heat flux was measured using Pearson's linear correlation coefficient, *r* (see Figure 4-17).

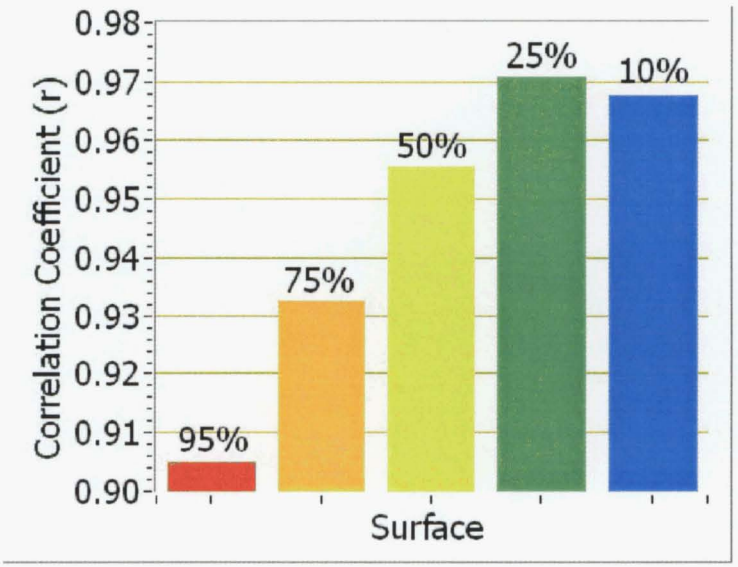

Figure 4-17: Comparing shape factor surfaces as predictors of heat flux.

Using the best linear fit, predictions for each surface were related to recorded data providing maximum and minimum absolute error, and mean square error. These statistics appear in Table 4-4.

Surface	Correlation Coefficient (r)	Max. Absolute Error	Min. Absolute Error	Mean Squared Error (MSE)
95%	0.90	2.9663	0.0103	0.7881
75%	0.93	2.4178	0.0227	0.5678
50%	0.96	2.0347	0.0165	0.3785
25%	0.97	1.8686	0.0032	0.2505
10%	0.97	2.1997	0.0129	0.2784

Table 4-4: Statistics used to choose best predicting surface.

From this table it is evident that the 25% surface is the best single surface to use for predicting heat flux because it has the greatest correlation coefficient, the least maximum and minimum absolute error, and the least MSE. A graph of recorded heat flux data against shape factors calculated from the 25% surface appears in Figure 4-18.

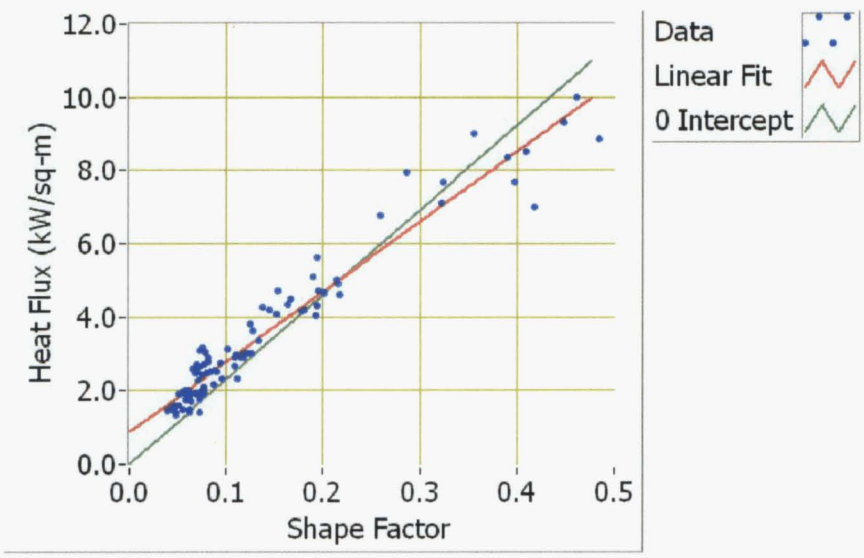

Figure 4-18: Heat flux versus Shape factor for the 25% surface.

Two linear trend lines have been fitted to this graph; one is forced through the origin and the other is not. Referring to the equation for heat flux, $Q = \sigma T^4 F$, it is reasonable to expect the line to pass through the origin since if there were no flame, $F = 0$ and $Q = 0$. This would suggest that the line with $y = 0$ intercept, should be used. The equation of this line is $I = 23.067F$ where the slope of the line substitutes for σT^4 in the equation.

Equation	R^2	Max Absolute Error	Min. Absolute Error	Mean Squared Error (MSE)
Linear Fit	0.9424	1.8686	0.0032	0.2505
0 intercept	0.8773	2.6562	0.0080	0.5336

Table 4-5: Comparing the linear fit with 0 intercept as predictors.

However, checking statistics for the zero intercept equation proves it to be an inferior predictor (see Table 4-5). Therefore, for the purpose of establishing an accurate thermal radiation field for this flame in this laboratory the line with zero intercept was not used. The line of best linear fit was therefore used as a predictor. This line has the equation:

$$Q = 19.114F + 0.8621 \qquad (4\text{-}2)$$

4.2.4 Determining the thermal radiation field

The process for determining the thermal radiation field is described in section *3.4.4*.

4.2.4.1 *Establishing Point Cloud Boundaries*

The first step is to initialise a cloud of points in the region surrounding the flame. Since shape factors are prone to error when calculated for a point close to the surface, points in the cloud were not generated within 200mm of the flame. Errors in shape factor

calculations are investigated in *4.3 Discussion.* The limits of the flame surface are given in Table 4-6:

	Maximum	Minimum
x	359.78	-352.85
y	855.01	0.00
z	297.11	-190.00

Table 4-6: The limits of the flame surface.

The boundaries of the point cloud were specified as given in Table 4-7. These values were chosen after looking at the recorded heat flux data, which suggests that heat flux values are less than 2 kW/m^2 outside this area. The heat flux surfaces we have chosen to find are for the values 15 kW/m^2, 10 kW/m^2 and 5 kW/m^2, which lie within the proposed point cloud. In this space, 30,000 points were generated at random locations.

	Maximum	Minimum
x	1750	-1750
y	3000	-300
z	1600	-1600

Table 4-7: The limits of the point cloud.

4.2.4.2 *Calculating Maximum Shape Factor*

Using the technique described in section 3.4.4.1, the maximum shape factor is determined for each point in the cloud surrounding the flame. This 3D field of shape factor values was then processed with FastRBF Toolbox. Near identical points are removed, and then an RBF was fitted using an accuracy of 0.05 and the `-errorbar` option. When evaluating the RBF, resolutions of 40, 35 and 30 were used for the 5, 10 and 15 kW/m^2 surfaces respectively. These values for the resolution were used to limit

the number of triangles in the resulting surfaces. Using these values the larger, 5 kW/m^2, surface has 7,522 triangles, the 10 kW/m^2, surface has 5,822 triangles, and the smaller 15 kW/m^2, surface has 3,774 triangles. These surfaces are visualised in Figure 4-19.

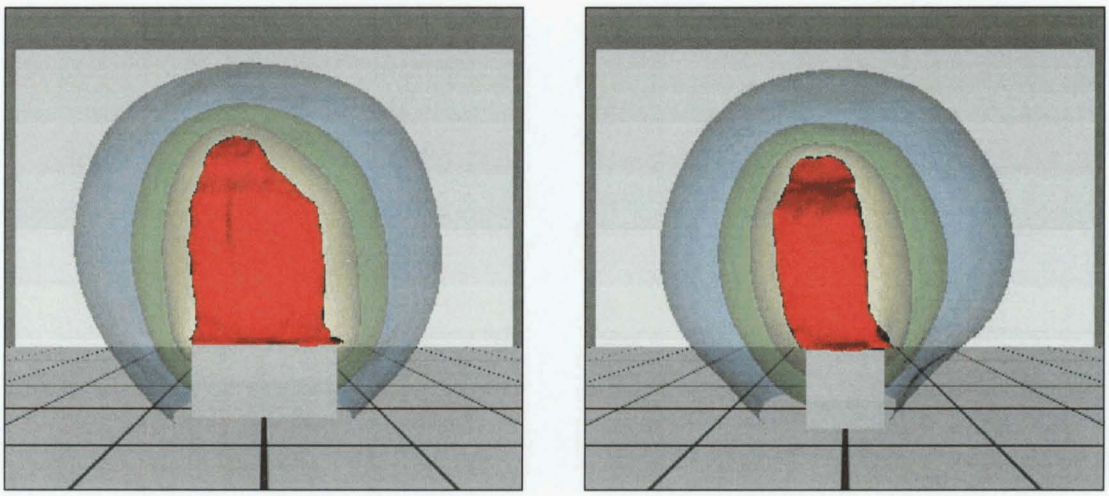

(a) Front view – 90°. (b) Side view – 0°.

Figure 4-19: Visualization of heat flux isosurfaces for 15, 10 and 5 kW/m^2.

4.3 Discussion

4.3.1 Maximum possible heat flux

If the shape factor F is set to 1 in equation (4-2), the maximum radiant heat flux from this fire becomes:

$$Q = 19.114 + 0.8621 = 19.98 \quad [\text{kW/m}^2] \tag{4-3}$$

The shape factor has value equal to 1 when it is on the emitting surface, therefore an object on the 25% surface should have an incident heat flux of 19.98 kW/m^2. This value is clearly a property of this particular flame and cannot be considered a transferable result.

This suggests that it was an error to assume emissivity, $\varepsilon = 1$. Therefore the discussion on emissivity, introduced in section *1.4.2*, needs to be extended.

4.3.2 Emissivity

4.3.2.1 *Bouguer's law*

Radiation that is emitted within a flame is attenuated along its path to the flame surface by absorption and scattering. A beam of radiation through a transparent carrier gas containing suspended soot has been found to attenuate exponentially according to Bouguer's law [42]:

$$i'_\lambda(S) = i'_\lambda(0)\exp(-K_\lambda S) \tag{4-4}$$

where

S = path length travelled through the attenuating medium,

$i'_\lambda(0)$ = the intensity of radiation entering the medium,

$i'_\lambda(S)$ = the intensity of radiation after travelling along path length, S,

K_λ = the extinction coefficient of the (homogeneous) medium.

4.3.2.2 *Optical Thickness and Mean Penetration Distance*

The exponent of equation (4-4), $\kappa_\lambda = K_\lambda S$, for a gas of uniform temperature, pressure and composition, is the *optical thickness* or *opacity* of the gas with path length *S*. Optical thickness is the measure of a given path length of gas to attenuate radiation of a given wavelength [42], and is closely related to radiation *mean penetration distance*, l_m.

$$\kappa_\lambda = \frac{S}{l_m} \tag{4-5}$$

The medium is optically thick if the mean penetration distance is small compared to the characteristic dimension of the medium, and it is optically thin when the mean penetration distance is much larger than the medium dimension. In the second case radiation can pass through the medium without significant absorption, and a volume element within the medium interacts directly with the medium boundary.

The extinction coefficient is composed of an absorption coefficient and a scattering coefficient:

$$K_\lambda = a_\lambda + \sigma_{S\lambda} \tag{4-6}$$

The Mie theory [42] tells us that scattering for soot is negligible compared with absorption. This is established by considering soot's particle size, optical constants, temperature, and the wavelengths of the associated radiation. Therefore, the extinction coefficient can be replaced by the absorption coefficient in equation (4-4). Further, the spectral emittance is given by [42]:

$$\varepsilon_\lambda = 1 - \exp(-a_\lambda L_e) \tag{4-7}$$

Here, L_e is the *mean beam length* of the volume, which is "*the required radius of a gas hemisphere such that it radiates a flux to the centre of its base equal to the average flux radiated to the area of interest by the actual gas volume*" [42].

Since the flame is assumed to be a *gray* emitter, we consider *total* emissivity and *total* absorptivity. In addition, we will write the extinction coefficient as simply K, and consider the mean beam length to be the diameter of a pool fire, D. Equation (4-7) then becomes [18]:

$$\varepsilon = 1 - \exp(-KD) \tag{4-8}$$

This shows that emissivity and optical thickness are closely related. After a flame has diameter greater than about 2 metres, it is regarded as optically thick since, no matter how much larger the flame becomes, the intensity of radiation at the surface cannot increase [4]. In this case the flame's emissivity $\varepsilon = 1$. However, a flame that is optically thin has emissivity $\varepsilon < 1$.

4.3.2.3 *Estimating emissivity for the July 29 experiment.*

Although the aspect ratio of the burner is not close to one, the equivalent diameter of the flame can be roughly approximated by:

$$D = \sqrt{\frac{4A}{\pi}} = \sqrt{\frac{4 \times 0.6 \times 0.3}{\pi}} = 0.4787\text{m} \tag{4-9}$$

A rough approximation for emissivity is also possible, by using equation (4-8) and using a, somewhat arbitrary, value for the extinction coefficient of $K = 1$.

$$\varepsilon = 1 - \exp(-0.4787) = 0.38 \tag{4-10}$$

The diffusion burner, with base dimensions 600mm × 300mm, therefore produces an optically thin flame with emissivity $\varepsilon < 1$.

4.3.3 Alternate methods of estimating heat flux

Rather than estimate the radiative properties of the flame by correlating recorded heat flux data with calculated shape factors, the emissive power of the flame could be estimated explicitly. For example, the total heat release of the fire is known to be 150 kW.

The Point Source model [41] provides a relation that gives the radiative fraction, as a function of diameter based on experimental data from a variety of fuel types, as:

$$\dot{Q}_r = \chi_r \dot{Q} = (0.21 - 0.0034\,D)\,\dot{Q} \tag{4-11}$$

Hence

$$\Rightarrow \quad \dot{Q}_r = (0.21 - 0.0034 \times 0.4787) \times 150 \;=\; 31.3\,\text{kW} \tag{4-12}$$

Since the area of the 25% surface, which was used for shape factor calculations, was calculated to be 1.405 m^2, this yields an average emissive power of:

$$\frac{31.3}{1.405} \;=\; 22.2\,\text{kW/m}^2 \tag{4-13}$$

This value is similar to that in equation (4-3), and could be used to estimate heat flux directly as shown in Figure 4-20. The line, $y = x$, is shown so that it is apparent that the estimates under-predict the recorded heat flux in most cases. It is preferable that estimates overestimate actual heat flux values when designing for safety, which makes this correlation unsuitable.

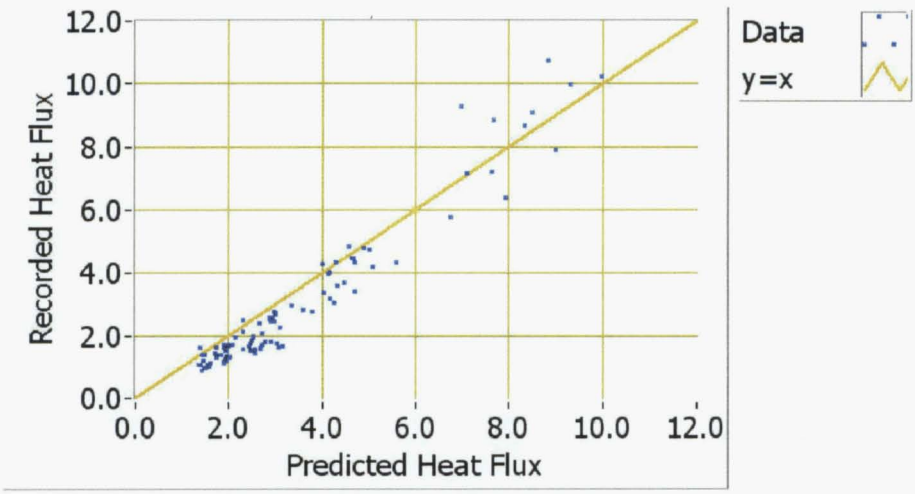

Figure 4-20: Predicting heat flux using an approximation for emissive power.

4.3.4 Temporally separate data

In the experiment conducted on July 29, video was recorded from six camera positions and heat flux data was recorded from 96 gauge locations. Ideally this information should be collected simultaneously using six cameras and 96 heat flux gauges so that all heat flux data refers to the fire that appears in all camera views. However, since we have only four heat flux gauges and a single camera, we are obliged to accept temporally separate data. Therefore, in order to obtain valid results it is essential that the size and location of the fire is kept constant. The size of the fire was accurately maintained at a constant heat release rate using an electronically regulated fuel supply. The location of the base of the flame is constant because the diffusion burner fixes it. However the body and tip of the flame can move due to air currents and eddies within the laboratory. Our task is, therefore, to minimise any air movement that may affect the flame by adjusting the openings of vents and doors, adjusting the speed of extractor fans, and limiting the ceiling temperature of the laboratory. The last measure was adopted after observations suggested the flame's behaviour was becoming significantly erratic as the ceiling temperature rose above about 65°C. When judgement determined that factors in the laboratory had disrupted the flame, data collection was suspended until stability was re-established. This usually meant shutting down the flame and boosting the extractor fans for 5 – 10 minutes.

4.3.5 Choosing camera height

The visible flame tip was estimated during the experiment to be approximately 1400mm above the base of the flame. Because of this, the cameras were placed at a height of 700mm. However, the height of the 25% flame surface from which shape factor calculations were made was about 865mm, which suggests that a camera height of about 450mm would have been more appropriate for centring the relevant portion of the flame in the field of view. Centring the flame in the field of view reduces perspective error during reconstruction.

4.3.6 Reducing image size

The image size of the Canon Elura is 720 x 480 pixels. Note that the dimensions of images are generally given as *width* × *height*, which is contrary to the convention of specifying array dimensions as *row* × *column*. A computer monitor with a standard resolution of 800 x 600 pixels can display an image that has width 720 and height 480, however little space is left for window frames, toolbars and access to controls on the LabVIEW Panel. Increasing the resolution of the screen to 1024 x 768 can remedy this, although it is difficult to select specific pixels with a mouse at this resolution. Reducing the size of movies by half makes them much easier to manage on the screen and, although this means discarding data, the loss in accuracy of subsequent shape factor estimates appears to be minimal. The computational expense of our implementation of the minima reconstruction technique depends on the size of the point cloud and not the image size, so it is worth noting that no computational savings are made by reducing the size of images.

When reducing the size of input images, it is important to preserve the aspect ratios. This is necessary for pixel calibration, which defines the correspondence between pixels and real-world units.

4.3.7 Convergence of Newton's method

Only a few iterations are required to achieve accuracy to within eight significant figures. For example, the details of Newton's Method for the projection of the front view of the July 29 experiment are given here.

The user provides the following information:

- The locations of points $\mathbf{P}_1'$ and $\mathbf{P}_2'$ in the image (see Figure 4.21). In screen (image) coordinates these points are $\mathbf{P}_{1S}' = (275, 441, 0)$ and $\mathbf{P}_{2S}' = (489, 446, 0)$, with their corresponding viewing coordinates being $\mathbf{P}_{1V}' = (-84.5, -201.5, 0)$ and $\mathbf{P}_{2V}' = (129.5, -206.5, 0)$.

- This image has dimensions 720×480.

- The locations of points $\mathbf{P}_1$ and $\mathbf{P}_2$ in world coordinates are $\mathbf{P}_{1W} = (-300, 0, 150)$ and $\mathbf{P}_{2W} = (300, 0, 150)$.

- The location of the camera in world coordinates, $\mathbf{C}_W = (0, 700, 2950)$.

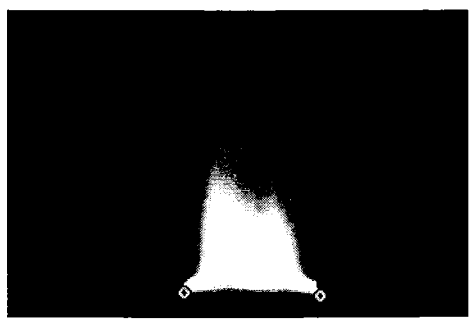

Figure 4-21: $\mathbf{P}_1'$ and $\mathbf{P}_2'$ located in the image.

From the given information the following are calculated and provided as input to Newton's Method:

- Viewing coordinates of the camera, $\mathbf{C}_W = (0, 0, -1008.66105034)$.

- World coordinates of points $\mathbf{P}_{1W}' = \begin{bmatrix} -106.70099703 \\ 451.03100693 \\ 1954.12402771 \end{bmatrix}$,

  and $\mathbf{P}_{2W}' = \begin{bmatrix} 107.28392929 \\ 449.67083165 \\ 1948.68332659 \end{bmatrix}$.

- Lengths $a = 218.50057208$, $b = 243.74679485$ and $c\ (or\ z_C) = 1008.66105034$.

- Approximate solution $\mathbf{x}^{(0)} = \begin{bmatrix} 0.29146613 \\ 700.00000000 \\ 1951.40367715 \end{bmatrix}$.

A solution is found that provides the location of the **VRP** in five iterations so that the error between successive approximations is less than 10^{-8} millimetres. Table 4-8 shows the decreasing error for the front and the side projections.

Iteration	$\xi^{(k)}$ Front	$\xi^{(k)}$ Side
1	$\xi^{(0)} = 49.25290253$	$\xi^{(0)} = 53.24973773$
2	$\xi^{(1)} = 5.90527184$	$\xi^{(1)} = 6.81191628$
3	$\xi^{(2)} = 0.08740278$	$\xi^{(2)} = 0.11524572$
4	$\xi^{(3)} = 0.0001916$	$\xi^{(3)} = 0.00003301$
5	$\xi^{(4)} = 0.00000000$	$\xi^{(4)} = 0.00000000$

Table 4-8: Decreasing error of Newton's Method.

4.3.8 Limitations of Minima Reconstruction Technique

The minima reconstruction technique does not reveal any information about the interior of the flame. Methods that use line-integral information, like as FBP and ART, can establish the presence of internal features. For example, the location of bone can be ascertained from medical data. Probability information cannot be resolved in the same way and therefore cannot provide internal detail. A consequence of this is that the minima reconstruction technique cannot reveal non-convex features present in the flame's surface. For example, consider the cup in Figure 4.22. No matter how carefully the cameras are placed about the cup of Figure 4.22a, the inevitable result of minima reconstruction is the cup shown in Figure 4.22b.

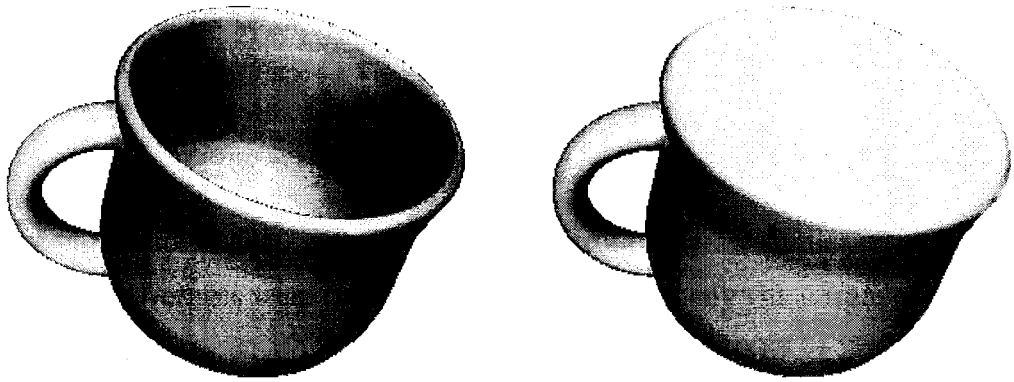

(a) Cup. (b) Result of minima reconstruction.

Figure 4-22: Non-convex features cannot be revealed using minima reconstruction.

4.3.9 Colour planes

The best colour plane to extract while processing the frames of a video can vary. For example, since the west wall of the University of Canterbury Fire Laboratory is painted green, and the video includes predominantly red and brown hues, it was found that the *RGB – Blue* plane provides best contrast between the flame and the background. Best results were obtained for another video, recorded with a different camera, by using the *HSL – Luminance* plane. Lighting conditions, camera parameters, backgrounds and flame performance can vary between videos despite attempts to control these things. Therefore, it cannot be assumed that extracting one particular colour plane will always produce best results. This limits the amount of automation that can be achieved while processing videos since an operator needs to perform trials and exercise judgement in order to optimise results.

4.3.10 Time for averaging

A controlled flame, such as this propane diffusion burner with its electronically regulated fuel supply, is stationary except for turbulence and some slight movement due to air currents and eddies in the laboratory. In this case similar results would likely be obtained if the averages were constructed from twice as many (360) frames. This is not the case for an uncontrolled flame such as an upholstered furniture fire. An upholstered furniture fire is continually changing size and position during a burn. For this reason it is apparent that one should not accumulate averages for any longer than is necessary at the risk of degrading the acquired information. Since it has been established that a

minimum of about six seconds is necessary, it is recommended that six seconds also be regarded as a maximum.

It has been mentioned that, with respect to a controlled flame, similar results would be obtained if the averages were constructed from twice as many video frames. One of the reasons these results would not be the same, is that the 100% region of the flame gradually diminishes. Figure 4-23 graphs the area in pixels of the 100% region against the number of frames used to construct the average. Recall that in Figure 3-8 the area of the 75%, 50% and 25% regions became stable around 180 frames (six seconds at 30 fps). Figure 4-23 shows that, rather than becoming stable, the 100% region continues to be eroded away. This is an argument for not exceeding a six-second average for a controlled flame, and suggests that one should be cautious about using the 100% region as a source of information.

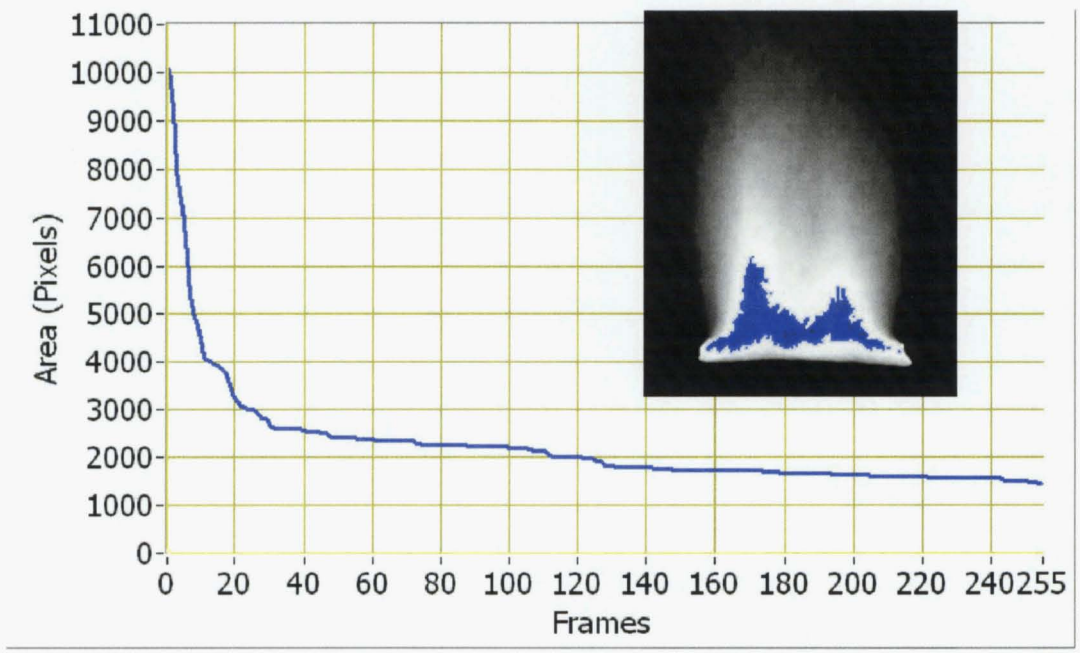

Figure 4-23: Diminishing area of the 100% flame region.

4.3.11 Accuracy in Shape Factor Calculations

Hankinson [7] examined the accuracy of his technique by comparing it with exact analytical solutions for a right circular cylinder and a vertical target at ground level and

aimed at the centre of the base of the cylinder. This arrangement is illustrated in Figure 2-1 and the shape factor is given by equation (4-18) [42]. Hankinson [7] used a cylinder of height 10m and diameter 4m for this study.

$$F = \frac{1}{\pi H}\tan^{-1}\frac{L}{\sqrt{H^2-1}} + \frac{L}{\pi}\left[\frac{X-2H}{H\sqrt{XY}}\tan^{-1}\sqrt{\frac{X(H-1)}{Y(H+1)}} - \frac{1}{H}\tan^{-1}\sqrt{\frac{(H-1)}{(H+1)}}\right] \quad (4\text{-}18)$$

where

$$L = \frac{l}{r}, \qquad H = \frac{h}{r}, \qquad X = (1+H)^2 + L^2, \quad Y = (1-H)^2 + L^2,$$

and

l = the length / height of the cylinder,

r = the radius of the cylinder,

h = the perpendicular distance from the target to the cylinder axis.

Hankinson [7] discovered that accuracy is dependent on the number of elements into which the surface is divided. In addition, to achieve a desired level of accuracy, the number of surface elements increases as the distance from the surface to the target decreases. This is because shape factor calculations are based on the equation for energy exchange between differential area elements. For a surface containing a given number of elements the relative size of an element increases as the distance to the target decreases. This means the solid angle $d\omega_S$ subtended by the surface element when viewed from the target also increases, until it can no longer be considered differentially small. In this case the area of the surface element dS_i must be considered to be finite, S_i. Then the angle θ_S and the distance r will be different for different positions on S_i.

To explore this issue further, a similar investigation was conducted involving a number of right circular cylinders of height 10 units and diameter 4 units. These cylinders were produced with surfaces containing varying numbers of triangles. Figure 4-24 illustrates two of these cylinders.

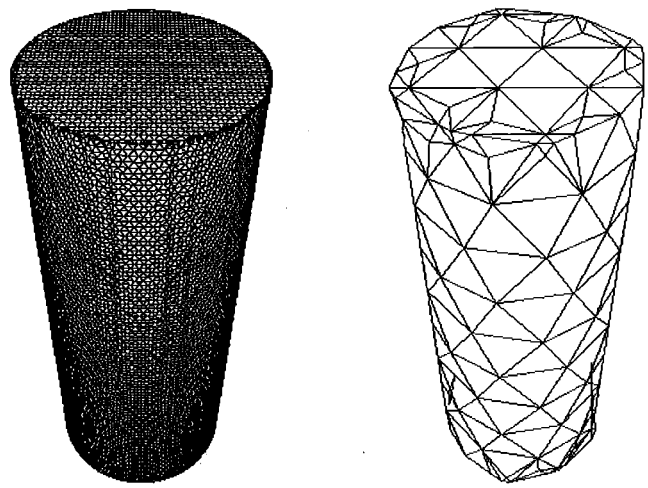

(a) 27,106 triangles. (b) 348 triangles.

Figure 4-24: Right circular cylinders of different surface resolutions.

Shape factors calculated from these surfaces were compared to the value given by equation (4-18). Figure 4-25 shows that accuracy is lost as the target approaches the surface and, as Hankinson [7] reported, increasing the number of surface elements allows the target to move closer to the surface while maintaining a given level of accuracy.

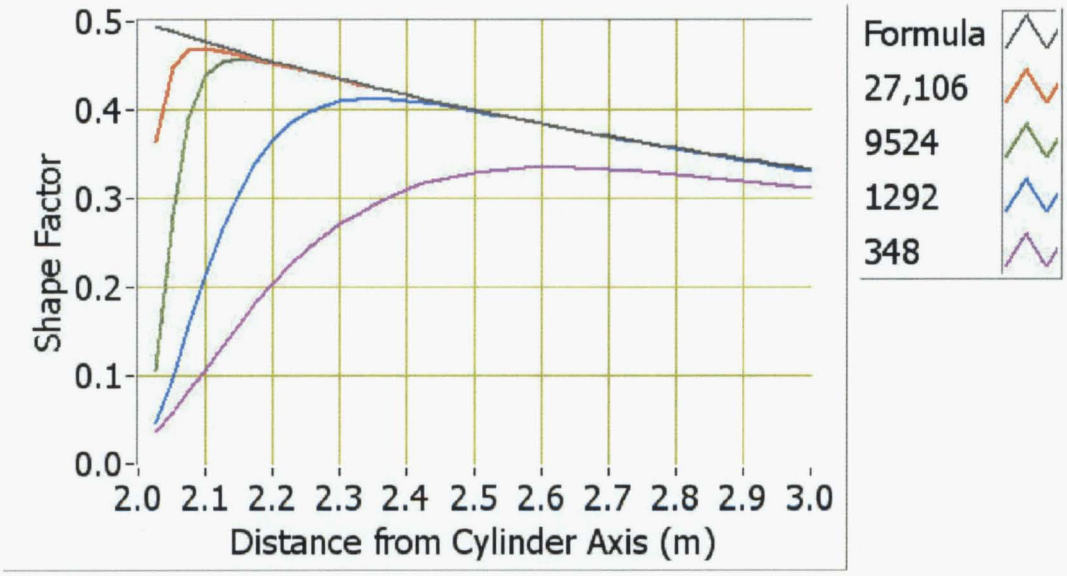

Figure 4-25: Investigating accuracy of shape factor calculations for a cylinder.

Accuracy of shape factors calculated from the surface containing 27,106 triangles remained within 1% of the analytical value until the target was 130mm from the surface, and shape factors calculated from the surface containing 9,524 triangles remained within 1% of the analytical value until the target was 167mm from the surface.

A comparison between results from this investigation and the surface extracted from the RBF was considered reasonable since the relative dimensions of the cylinder and the flame were roughly the same. That is considering the flame's height (refer to Table 4-6) and equivalent diameter.

Based on the equivalent diameter for the diffusion burner (0.479m) and the number of triangles in the extracted surface (25,752), no points in the thermal radiation field were established within 200mm of the flame surface. This was determined from the information for the cylinder with 9,524 triangles in this way:

$$167 \times \frac{0.479}{0.4} \approx 200\text{mm} \qquad (4\text{-}19)$$

Chapter 5

Application to Upholstered Furniture (Uncontrolled Flame)

In this chapter the techniques presented in Chapter 3 and developed further in Chapter 4 are applied to a burning upholstered chair. Issues encountered during this process are investigated and discussed.

5.1 Recording the Fire

In this experiment an upholstered chair was burnt. Although we had previously processed videos of upholstered furniture fires, this experiment was the first to provide us with recorded heat flux data. Heat flux data is required to accurately determine the thermal radiation field, and to further investigate the effects of emissivity. These issues are discussed at the end of the chapter. A coordinate system was established with its origin near the centre of the base of the chair. It is a right-handed coordinate system as described in Chapter 4. The dimensions of the chair were recorded along with its position relative to the coordinate system. The four points at the corners of the base of the chair were selected as possible reference points for the reconstruction. These four points and the origin of the coordinate system are illustrated in Figure 5-1. All measurements are given in millimetres.

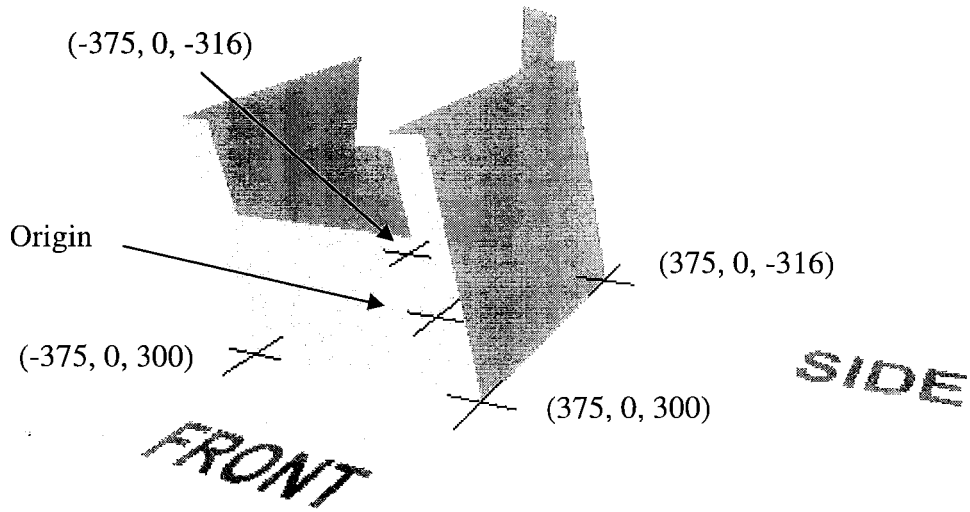

Figure 5-1: Origin of the coordinate system with reconstruction reference points.

5.1.1 Video

Video of this fire was simultaneously recorded on two cameras, a Sony Handycam and a Canon Elura. Since the heat release rate of the burning chair was assumed to be much greater than the heat release rate for the diffusion burner of earlier experiments, the cameras were placed outside the laboratory to ensure their safety. Views of the fire were therefore obtained through observation windows at the front and the side of the laboratory. Figure 5-2 illustrates the camera positions in terms of the coordinate system described previously.

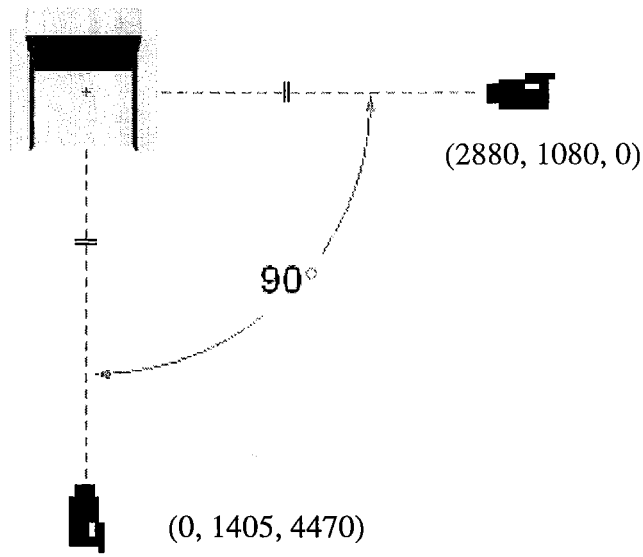

Figure 5-2: Camera locations.

The Canon Elura was placed at the front of the room and the Sony Handycam was placed to the (right) side. To get a clear view of the flame and to keep clear of equipment in the control room, the Sony Handycam had to be placed less than three metres from the origin of the coordinate system. At this distance the camera's field of view was not sufficient to capture the full height of the flame. Since the Sony camera has image dimensions 720 × 576 pixels, the camera was turned 90° so that the larger dimension became the height of the image therefore captured more of the flame.

The exposure of both cameras was set to automatic to prevent overexposure and blooming at the peak of the burn.

Unlike the controlled flame used in Chapter 4, the uncontrolled burning of the upholstered chair required that all data be recorded simultaneously. This eliminated all issues associated with having temporally separate data.

5.1.2 Heat Flux Data

Six heat flux gauges were used and their positions appear in the plan view of Figure 5-3. The origin of the coordinate system, introduced at the beginning of the chapter, was established at the intersection of the perpendicular line through the heat flux gauges. All measurements in Figure 5-3 are expressed in this coordinate system.

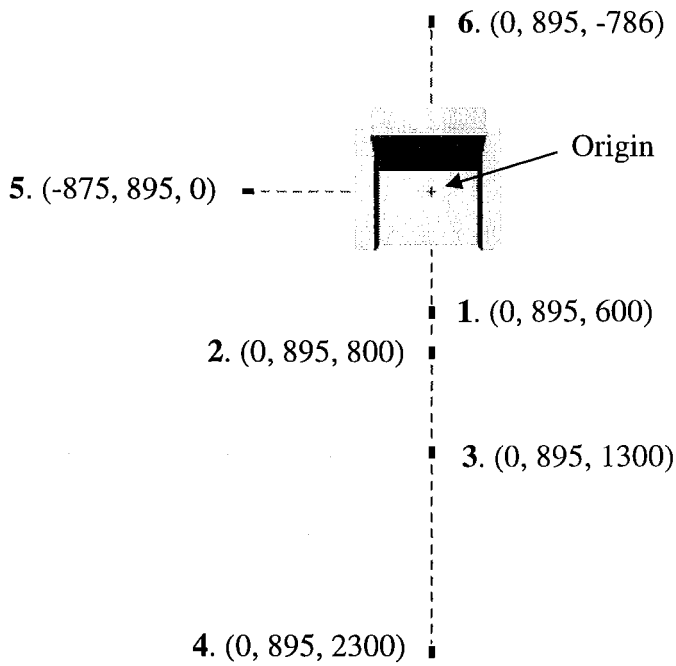

Figure 5-3: Location of heat flux gauges.

A heat flux value was sampled from each gauge at a rate of 1Hz. The first five minutes of video and heat flux data were used from this experiment since the significant features of the burn occurred during this time. These features are described and analysed in the following section.

5.2 Analysis

To help identify significant features of the burn, a graph of flame area versus time for each camera view was produced. This graph appears in Figure 5-4. Note that, since the cameras were at varying distances from the fire, the graphs should not be compared quantitatively. Data from a third camera is included in this graph although, for reasons discussed later, it was not used for reconstructions. The reason for including this view now is that it provides information about the progress of the fire that cannot be obtained from the other camera views. The third camera was at an angle of 219°, where 0° is the side view and 90° is the front view. The videos were referenced in conjunction with Figure 5-4 to explain its features. For example, the sharp increase in flame area, seen in the 219° view between about 1:50 and 1:55, was due to the fire coming through the back of the chair.

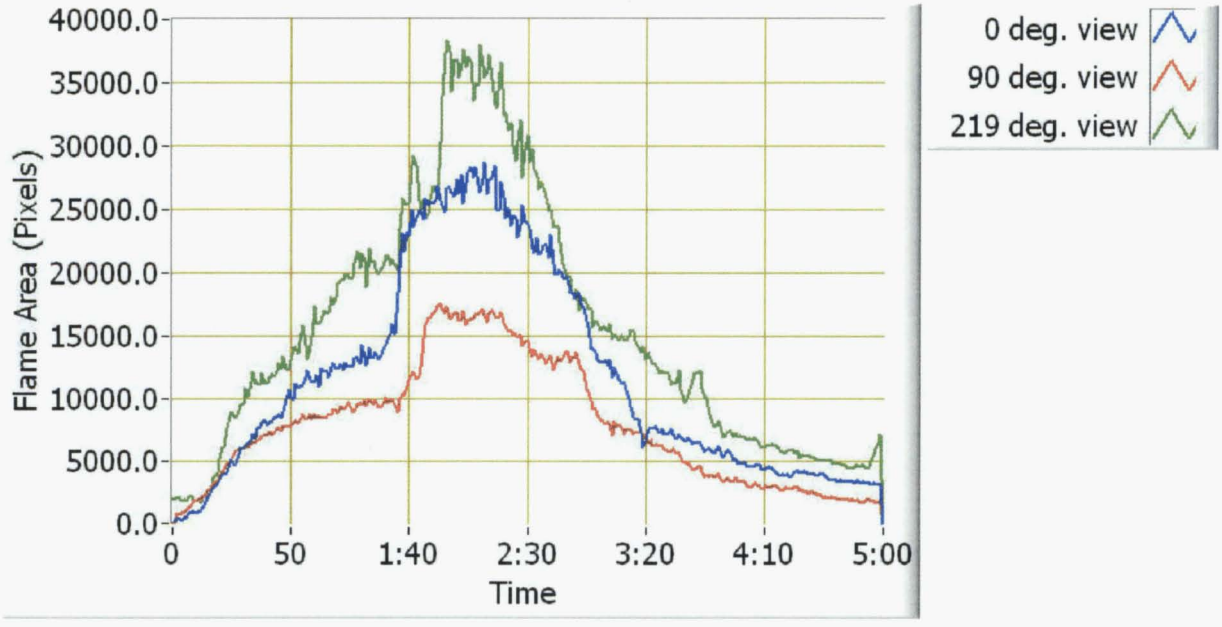

Figure 5-4: Flame area in three camera views.

Since occlusion was expected to be the key issue when reconstructing the flame, two periods of the burn were chosen for analysis. Based on the findings of Chapter 4, a six second video clip was extracted from each camera for both periods of interest. The first period, from 58 to 64 seconds after ignition, was selected because the arms of the chair had burnt out, but the back was still intact. This provided us with an opportunity to test the minima reconstruction technique on a case where occlusion (by the back of the chair) was significant. The second period, from 112 to 118 seconds after ignition, was selected because the entire chair was ablaze with only the wooden frame remaining visible. Here, the camera has a relatively clear view of the flame.

5.2.1 Image Analysis

Since automatic exposure was used for both cameras, the image processing techniques were similar to those employed for the automatically exposed video of Chapter 4. That is, the HSL-Luminace plane was extracted, a threshold was applied, and the image was repaired using the fill-holes algorithm. Figure 5-5 shows frames of video from the middle of the six-second video clips recorded approximately one minute after ignition. The view from the front is obstructed by equipment holding the heat flux gauges and the ignition burner in place, and to a much lesser extent by rods that hold thermocouples in

the plume of the flame. The frame of the chair's arm is the main obstruction in the side view.

(a) Side view. (b) Front view.

Figure 5-5: Frames from period 1 from side and front cameras.

Frames of video from the middle of each six-second video clip, taken approximately two minutes after ignition, are shown in Figure 5-6. Although the chair is entirely consumed by fire, it appears that a significant amount of the chair's frame remains to occlude the view of the flame.

(a) Side view. (b) Front view.

Figure 5-6: Frames from period 2 from side and front cameras.

5.2.2 Averaged Images

The Canon Elura records 30 frames per second (fps) and requires 180 frames to construct a six second average. The Sony, which records at 25 fps, requires only 150 frames. Image processing may leave some unwanted artefacts in the image (see Figure 5-7a). These are bright objects in the room that are included with the flame by the thresholding operation. These objects need to be removed from the averaged images. In a greyscale image it can be difficult to see the extent of the unwanted objects since dark greys often cannot be distinguished from black. It may be easier to convert the averaged images to 24-bit and fill from the edge with red. This allows the unwanted objects to be clearly seen. The result of doing this is shown in Figure 5-7b.

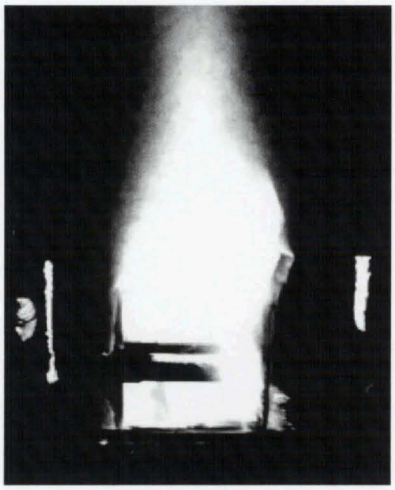

(a) Processed image.

(b) Background red.

Figure 5-7: Unwanted artefacts remaining after thresholding and averaging.

With the unwanted objects clearly visible, they can be easily removed in a drawing program using paint tool or a tool that allows a rectangular region of colour (red in this case) to be dragged out (see Figure 5-8a). The final step is to restore the red area to black using a fill tool (see Figure 5-8b).

(a) Unwanted areas painted out.

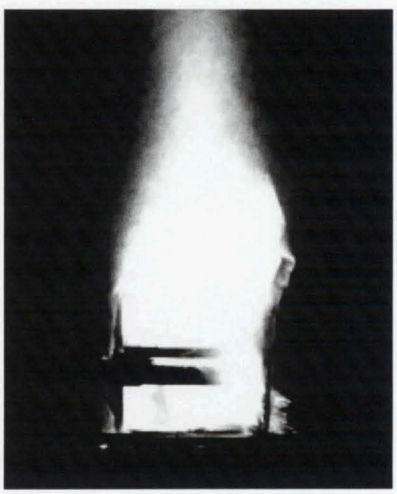

(b) Red area restored to black.

Figure 5-8: Removing unwanted artefacts.

Eliminating unwanted objects can also be achieved by specifying a mask during image processing that excludes anything outside the area of the flame. This technique requires first checking the video to establish the flame boundaries.

The averaged images from the front and the side views for the first reconstruction are given in Figure 5-9, and those for the second reconstruction appear in Figure 5-10.

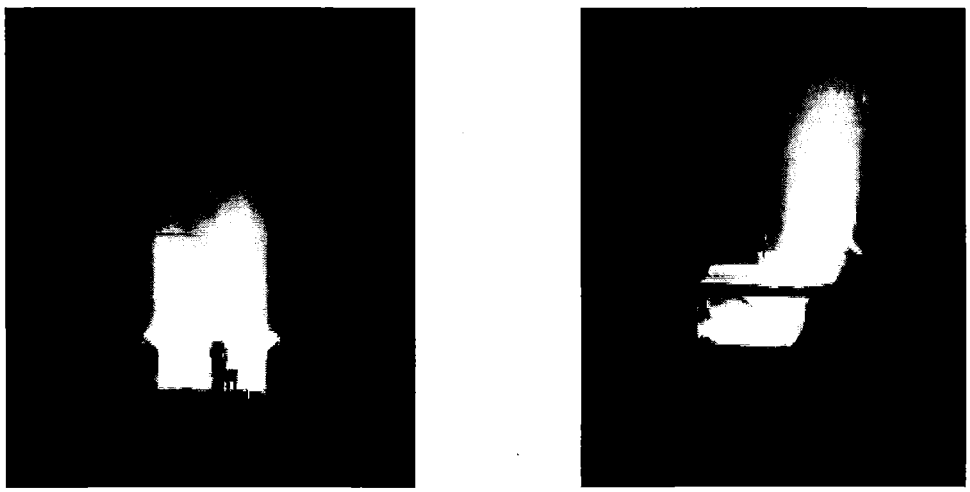

(a) Front view. (b) Side view.

Figure 5-9: Averaged images for the first reconstruction.

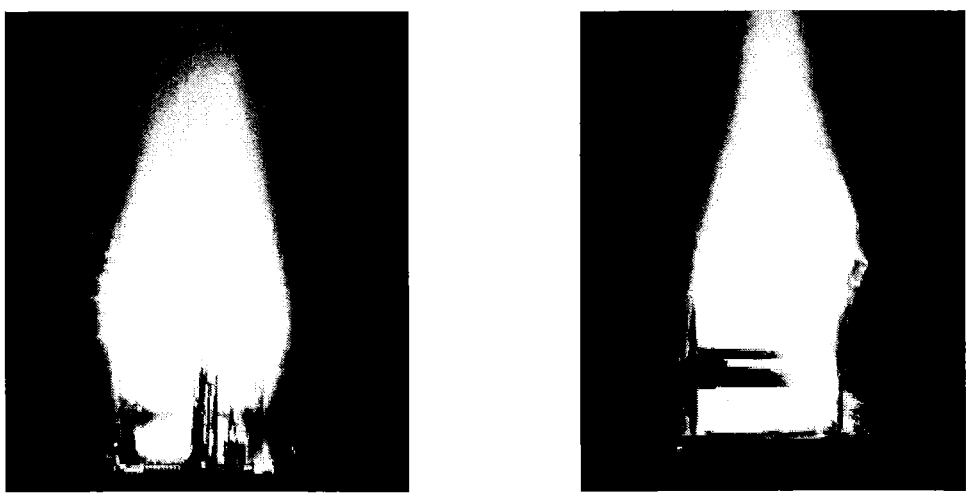

(a) Front view. (a) Side view.

Figure 5-10: Averaged images for the second reconstruction.

5.2.2.1 *Locating Reference Points*

With a flame generated from a diffusion burner, as used in Chapter 4, the top corners of the burner were convenient reference points because they were easily identified in the averaged images. However, in the case of an item of furniture, an averaged image presents no such clearly defined flame boundaries that can be used to reference the reconstruction. For this reason the location of reference points, $\mathbf{P}_1$ and $\mathbf{P}_2$, must be established by other means.

One way to determine the location of $\mathbf{P}_1$ and $\mathbf{P}_2$ in the averaged images is to use a frame from the beginning of the video, before the fire has started, when the chosen reference points are still identifiable. Figure 5-11 shows an image from the front view just before the chair was ignited. The image is very dark, particularly in the region near the base of the chair, and identifying reference points is not immediately possible.

Figure 5-11: Front view before ignition.

However, by extracting the HSV-Value plane and adjusting the curves, features in the region near the base of the chair become apparent (see Figure 5-12).

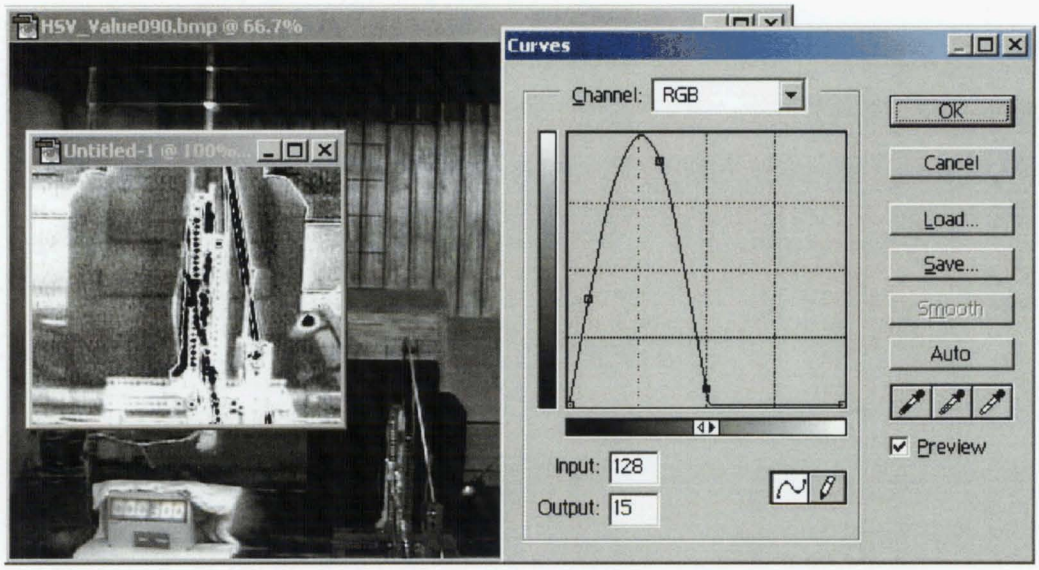

Figure 5-12: Revealing features at the base of the chair.

As a result of doing this, the locations of points $\mathbf{P}_1$ and $\mathbf{P}_2$ in the averaged image were determined to be (276, 456) and (419, 456) respectively. These coordinates adhere to standard image convention where x increases from left to right, and y increases from top to bottom. The points $\mathbf{P}_1$ and $\mathbf{P}_2$ correspond to (-375, 0, 300) and (375, 0, 300) respectively in 3D space as shown in Figure 5-1 at the beginning of the chapter.

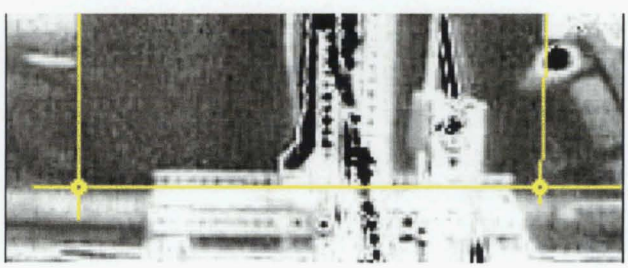

Figure 5-13: Determining reference points at the front of the chair.

The same method was used to find reference points in the side view. These were (168, 639) and (390, 639), which corresponded to the 3D points (375, 0, 300) and (375, 0, -316) respectively.

5.2.2.2 *Construct a Point cloud*

Boundaries for establishing a point cloud in the region of the flame were determined from the calibrated averaged images. Averages from the second period of interest were used because the flame was larger at this time. Using points $\mathbf{P}_1$ and $\mathbf{P}_2$ in the front view, a horizontal separation of $419-276=143$ pixels can be equated to a distance of $375-(-375)=750$ mm. This means 1 pixel = 5.24mm. The flame has a width spanning approximately 250 pixels centred about the origin of the coordinate system. The corresponding distance in the x-direction is $250 \times 5.24 = 1310$mm, or ±655mm. Adding a margin to this, the extent of the point cloud boundary in the x-direction was set to be ±700mm. Similarly, using the side view, the extent of the flame in the z-direction was also set to ±700mm. In the vertical direction, however, neither view could capture the flame tips due to the limited field of view of the cameras. Since the front view indicates the flames tips are higher than about 2250mm, and the side view indicates the flame tips are higher than about 1750mm, the upper limit of the point cloud was fixed at 2500mm above the base of the chair. As the upholstered chair burns and the melted foam drips to form a pool on the platform beneath the chair, flame can exist to a lower bound of approximately –100mm in the y-direction. The point cloud boundaries chosen for reconstructing the flame are listed in Table 5-1 (all values are expressed in millimetres).

	Maximum	**Minimum**
X	700.0	-700.0
Y	2500.0	-100.0
Z	700.0	-700.0

Table 5-1: Point cloud boundaries for flame reconstruction.

5.2.2.3 *Minima reconstruction*

By the method established in Chapter 4, the number of points required to avoid aliasing would have been decided thus:

Width / Interval	=	1400 / 28	= 50.00	≅ 50
Depth / Interval	=	1400 / 28	= 50.00	≅ 50
Height / Interval	=	2600 / 28	= 92.86	≅ 93

This suggests a total of $50 \times 50 \times 93 = 232{,}500$ points. A cloud with this many points would be computationally intensive. Our license for the FastRBF Toolbox allows us to deal with a maximum of 100,000 points and there is no guarantee that, after the projections, fewer than this amount would remain. Therefore, it was decided to proceed with an initial cloud of 40,000 points, while remaining alert to potential errors. For the first period of interest, which was approximately 1 minute after ignition, there remained 6,633 points in the cloud after projecting the averaged images and removing points having zero value. These points are shown in Figure 5-14a.

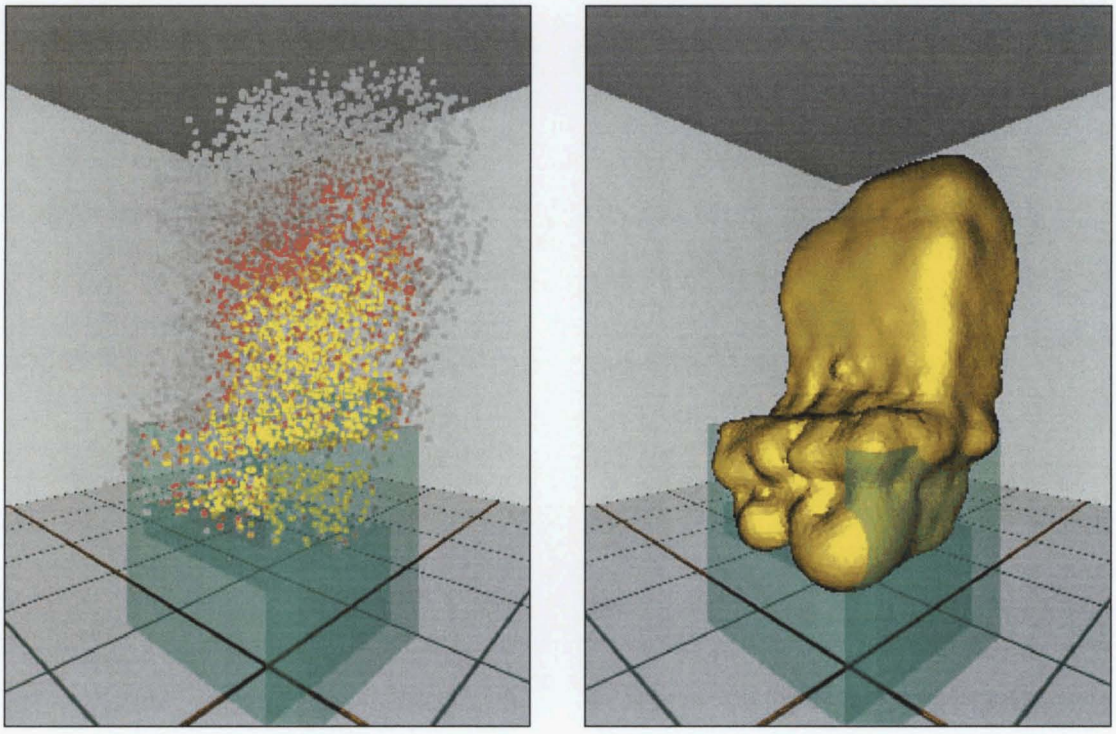

(a) Point cloud for 1st reconstruction. (b) 25% surface for 1st reconstruction.

Figure 5-14: Reconstruction for the first period of interest.

For the second period of interest 12,724 points remained in the cloud after projections were completed. These points appear in Figure 5-15a.

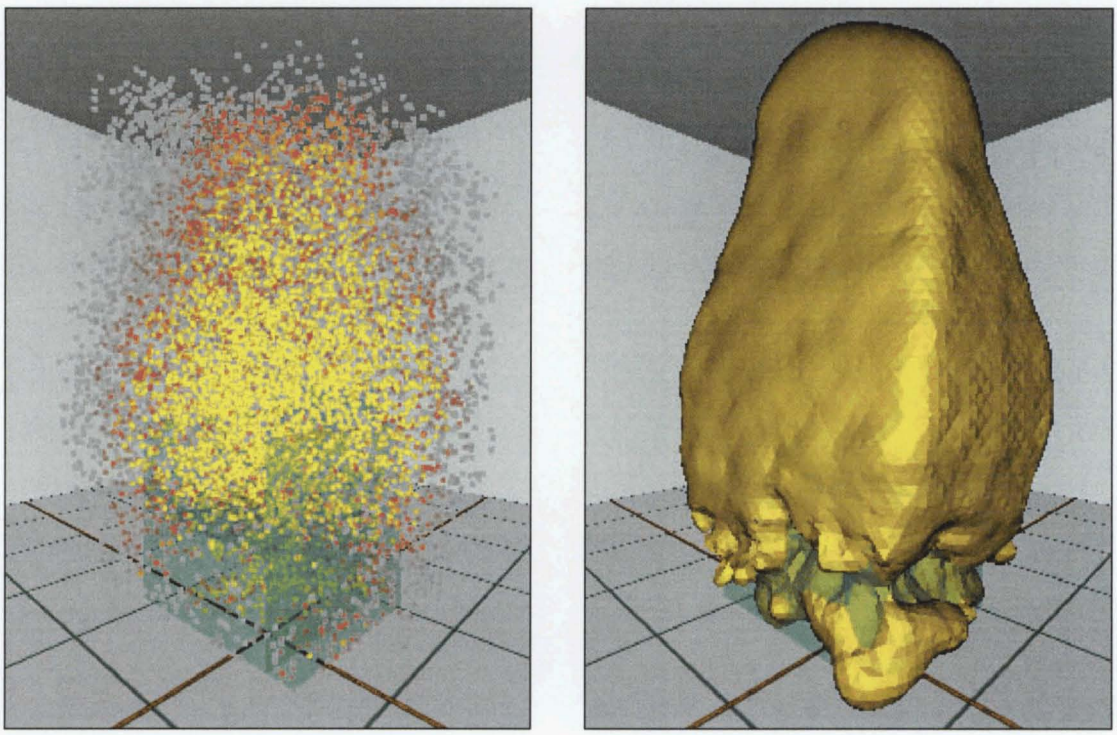

(a) Point cloud for 2nd reconstruction. (b) 25% surface for 2nd reconstruction.

Figure 5-15: Reconstruction for second period of interest.

5.2.2.4 *Fit and Evaluate a Radial Basis Function*

The sequence of commands used for fitting and evaluating an RBF were the same as those used in Chapter 4. Chapter 4 revealed that the 25% surface was the best single surface to use for predicting heat flux because it had the greatest correlation with recorded heat flux data. Based on this result, 25% surfaces were extracted from the RBFs for each reconstruction. These surfaces are shown in Figure 5-14b and Figure 5-15b respectively.

5.2.3 Find a Relationship between Recorded Heat Flux Data and Shape Factors

We have two reconstructions; one approximately one minute after ignition and the other approximately two minutes after ignition. Heat flux data is available at 6 locations for

each reconstruction. We will begin by considering just the first reconstruction. Since the averaged image is produced from six seconds of video, between 58 and 64 seconds after ignition, the heat flux data is also averaged over a six-second period. As in earlier experiments, heat flux values are sampled at one-second intervals and may be considered as an average of the heat flux recorded at the gauge during the previous second. Therefore, the heat flux values used were sampled from 59 to 64 (inclusive) seconds after ignition. The raw data for the first reconstruction is given in Table 5-2.

Time (s)	HF#1	HF#2	HF#3	HF#4	HF#5	HF#6
59	10.744510	6.957830	2.528744	1.094488	6.964559	12.132033
60	10.865722	7.195204	2.884805	1.153579	7.141327	13.142134
61	12.406126	8.028537	3.122684	1.331862	8.267590	12.606780
62	11.931379	7.851769	3.063088	1.213175	8.979711	13.379507
63	11.815217	7.907325	2.944401	1.213175	7.616074	13.440113
64	12.825318	8.503285	3.181775	1.391458	8.449408	14.329002
Average HF	11.764712	7.740658	2.954249	1.232956	7.903111	13.171595

Table 5-2: Raw heat flux data and averages for the first reconstruction.

The speed of shape factor calculations depends upon the number of triangles in the extracted flame surface. As the number of triangles increases, the speed of calculations decreases and the accuracy of shape factor calculations increases. Since results are preferred quickly and accurately, a compromise must be made. To check that accuracy was being maintained, two surfaces were extracted from the RBF that was fitted to the flame point cloud. For both isosurfaces all arguments were the same except the `resolution`, which adjusts the number and size of triangles in the surface. One surface was produced with 66,930 triangles and another with 16,774 triangles. Shape factors were calculated from these surfaces at the gauge positions and orientations used in the experiment. The results appear in rows one and two of Table 5-3.

	HF#1	HF#2	HF#3	HF#4	HF#5	HF#6
66,930 faces	0.4900	0.3385	0.1534	0.0538	0.3450	0.6077
16,774 faces	0.4885	0.3371	0.1527	0.0535	0.3432	0.6062
16,774 occlusion	0.4883	0.3369	0.1522	0.0531	0.3429	0.5618

Table 5-3: Shape factors calculated for the first reconstruction.

By inspection, the results do not seem to change much. Expressing the difference between rows 1 and 2 as a percentage of the value in row 1 gives the percentage error introduced by reducing the number of triangles from 66,930 to 16,774. The percentage error for the six gauges in both reconstructions was averaged and the result found to be 0.53%. This was considered to be a negligible loss of accuracy; so all subsequent shape factor calculations were made using the surface with 16,774 triangles.

At the time of the first reconstruction the fire had not burnt through the back of the chair. Therefore one would expect shape factors calculated at positions behind the chair to be overestimated unless occlusion is taken into account. For this reason, a model of parts of the chair that occluded the flame was produced (see Figure 5-16b for a comparison with the whole chair of Figure 5-16a). If the view of a triangle on the surface of the flame was blocked by a triangle in the model of the chair, then that triangle from the flame surface does not contribute to the shape factor. See Figure 5-16c for an illustration of the flame surface with the parts of the chair used to account for occlusion. Figure 5-16c shows that the arms of the chair have been removed giving a clear view of the flame from the front and the sides. The back of the chair blocks parts of the flame from the heat flux gauge #6. Notice that perspective error has allowed the flame to extend behind the back of the chair. This might suggest that attempts to account for occlusion would not be so effective, however using occlusion improves the linear correlation coefficient, between recorded heat flux and shape factor estimates,

from $r = 0.9951$ to $r = 0.9985$. This does not provide a significant improvement in this case, however the technique could in other cases.

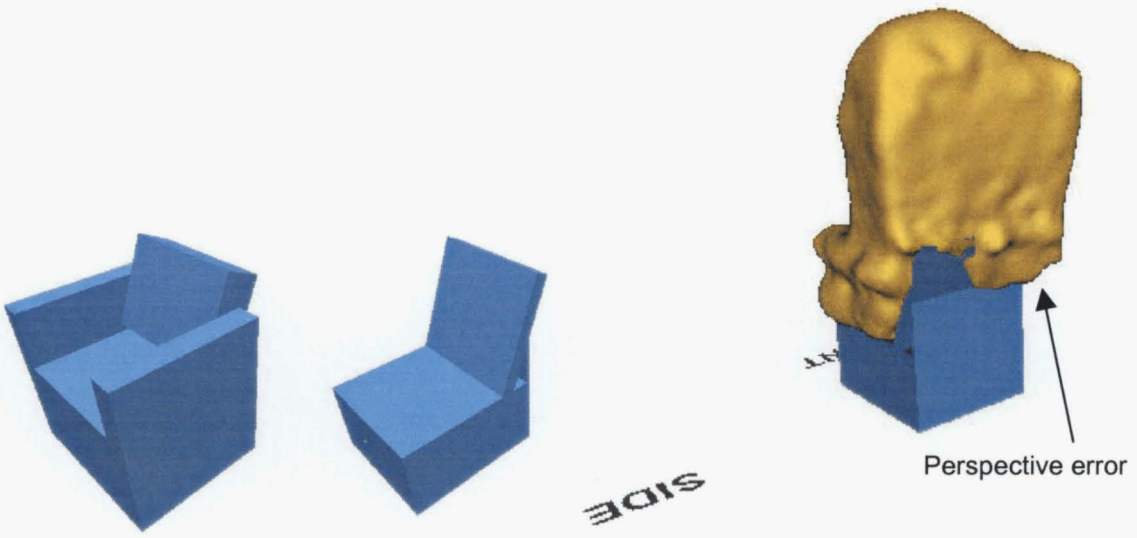

(a) Whole chair. (b) Parts that occlude. (c) Flame surface showing occlusion.

Figure 5-16: Illustrating how occlusion was catered for in shape factor calculations.

A graph of recorded heat flux data against shape factors calculated from the 25% surface is given in Figure 5-17 for the first reconstruction. The gauge positions are marked next to the data points.

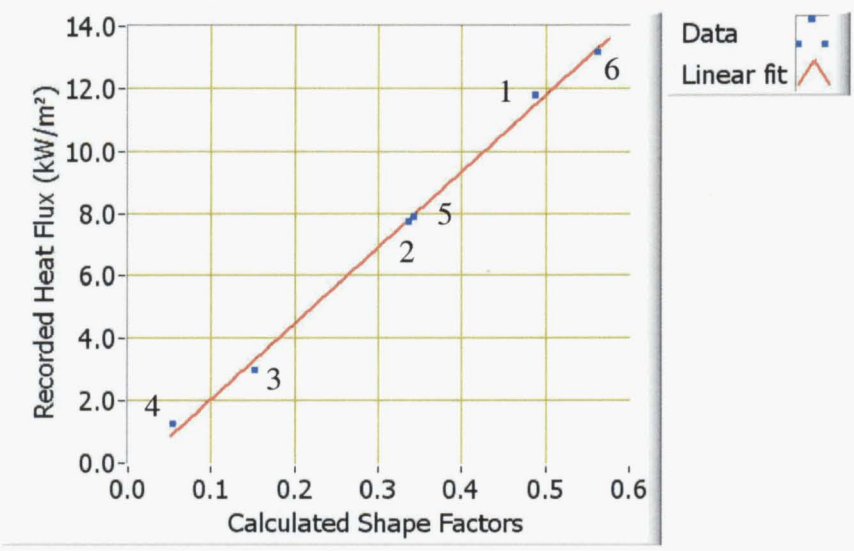

Figure 5-17: Heat flux versus shape factor for the first reconstruction.

The equation of the line of best fit is

$$Q = 24.275F - 0.3682, \tag{5-1}$$

which has a linear correlation coefficient of $r = 0.9985$.

The graph using data from the second reconstruction is given in Figure 5-18. Occlusion was not included in shape factor estimates from the second reconstruction because of the complexity of the task. If the geometry of the chair's frame was specified and used in calculations, perhaps an improvement could be obtained.

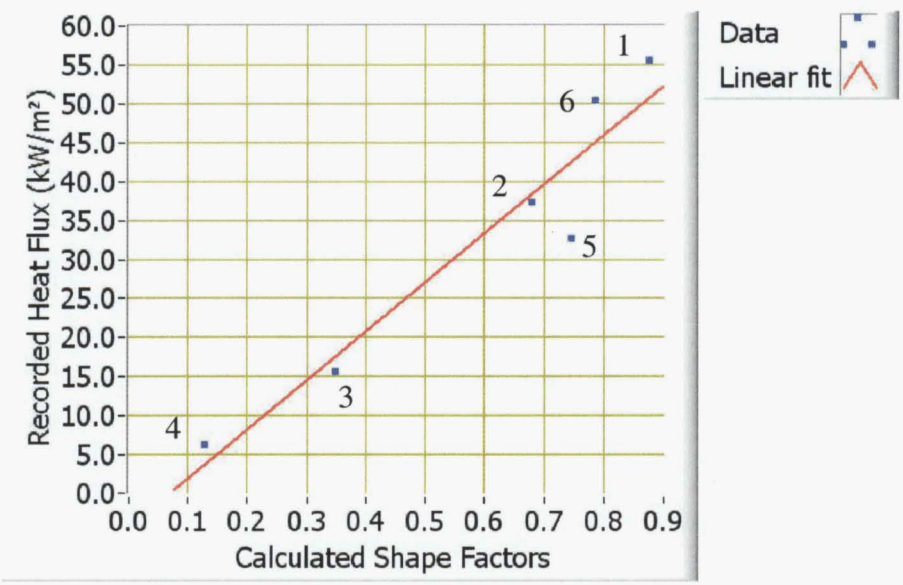

Figure 5-18: Heat flux versus shape factor for the second reconstruction.

For the second reconstruction, the equation for the line of best fit is

$$Q = 62.777F - 4.3912, \tag{5-2}$$

which has a linear correlation coefficient of $r = 0.9551$.

Whereas Figure 5-17 demonstrates a strong linear relationship, Figure 5-18 shows one data point to be significantly out of line. This data point was recorded at gauge position **#5** (-875, 895, 0). This is an unusual result when one considers that gauge **#5** is 500mm to the right of the chair, and the data point it most closely resembles is that of gauge **#2**, which is 500mm in front of the chair. These two data points were very close together in Figure 5-17 and, considering that the flame from second reconstruction appears more symmetrical (compare Figure 5-14b to Figure 5-15b), one might reasonably expect that this closeness would not diminish. This might be explained by error introduced to the reconstruction by perspective projections, since information in a perspective projection expands with increasing distance from the camera. When projected from the camera on the right side, the result is a flame that is larger than it ought to be on the left side where gauge **#5** was positioned. Figure 5-19 illustrates this by truncating the reconstructed flame at the height of the heat flux gauges. It is reasonable to expect the larger reconstructed flame on the left side to produce a higher shape factor than would be suggested by a recorded heat flux value. Perspective error would be greater for the side projection than the front projection since the side camera is closer to the flame. The side camera is 2.88m from the flame and the front camera is 4.47m from the flame.

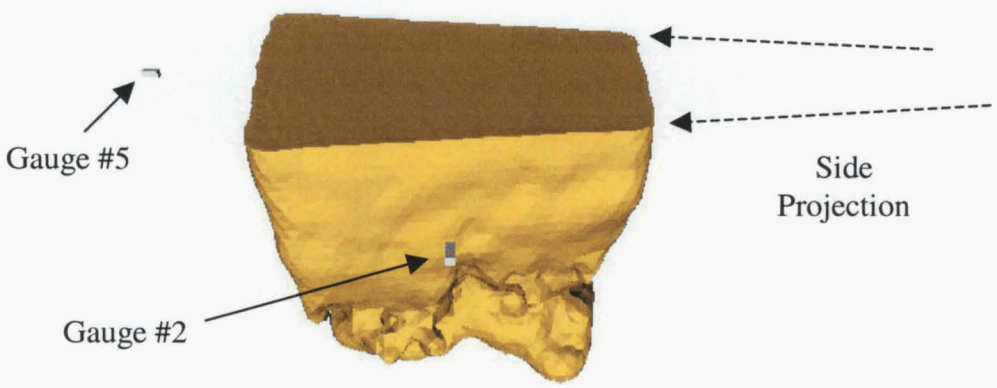

Figure 5-19: Perspective error producing high shape factors.

5.2.4 Determine the Thermal Radiation Field

5.2.4.1 *First Reconstruction – One minute after ignition*

Determining the thermal radiation field involves finding heat flux values at any point surrounding the flame. The method for doing this has been described in Chapter 3. A

cloud of points was generated randomly in a region that was bounded in each direction by the values in Table 5-4.

	Maximum	Minimum
x	1500	-1500
y	3000	-500
z	1500	-1500

Table 5-4: Bounds of the point cloud used to define the thermal radiation field.

The boundaries for the point cloud given in Table 5-4 were chosen by referring to the recorded heat flux data of Table 5-2. The maximum reading at gauge #3 was 3.18 kW/m^2. Since we are not interested in finding an isosurface with a value less than 5 kW/m^2, there is no need to extend the point cloud beyond gauge #3. Gauge #3 is at horizontal distance 1300mm from the origin of the coordinate system therefore, adding a margin for error, the bounds of the point cloud were set to be at a horizontal distance of 1500mm.

4800 points were generated randomly in this space. No points were allowed within at least 100mm of the flame surface to guard against errors in shape factor calculations.

The orientation of the gauge that yields maximum shape factor was found for each point and the magnitude of that shape factor was assigned to the point. Surface points, with shape factor = 1, were then added. These surface points allow the RBF to correctly interpolate the region between the flame surface and the point cloud. In Chapter 4, 10% of the size of the initial point cloud has been added as surface points. In this case, an inspection of the point cloud revealed some areas of the flame surface to be unsampled. For this reason 25% of the initial cloud size were added as surface points. That is, 1200 points were appended to the initial cloud of 4,800 points giving a final cloud of 6,000 points. Figure 5-20 illustrates the resulting point cloud including surface points.

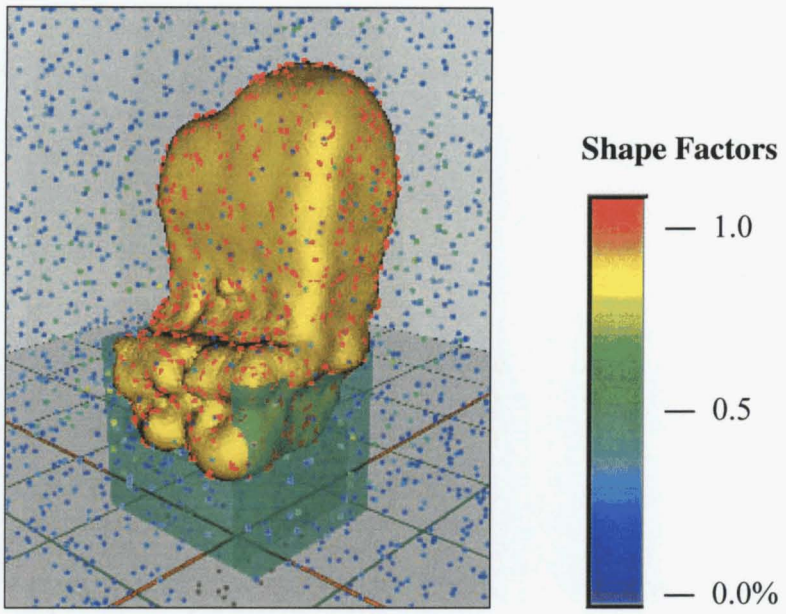

Figure 5-20: Surface points added to the shape factor data.

An RBF was fitted to the point cloud of shape factors using an accuracy of 0.05. This radial basis function describes the thermal radiation field in the region surrounding the fire. To visualize the thermal radiation field isosurfaces with values 20, 10 and 5 kW/m^2 were extracted from the RBF. Threshold values for these surfaces were derived from equation (5-1) in this way:

$$Q = 24.275F - 0.3682 \tag{5-3}$$

$$\Rightarrow \quad F = {}^{(Q+0.3682)}\!/_{24.275} \tag{5-4}$$

Heat Flux (kW/m^2)	Shape Factor (F)	(1-F)
5	0.2211	0.7789
10	0.4271	0.5729
20	0.8391	0.1609

Table 5-5: Determining the threshold value prior to surface extraction.

Because our data had been modified to adopt the FastRBF Toolbox convention of having larger values outside and smaller values inside the selected surface, the threshold value 1-*F* was used (see sample values in Table 5-5). In order to limit the number of triangles in the surfaces, and thereby improve the frame rate of the visualization, the resolution was adjusted during extraction. Data for the resulting surfaces is given in Table 5-6, and the surfaces are shown in Figure 5-21.

Surface	Resolution	Triangles
20 kW/m^2	23	15,646
10 kW/m^2	32	15,716
5 kW/m^2	41	15,776

Table 5-6: Information on extracted surfaces.

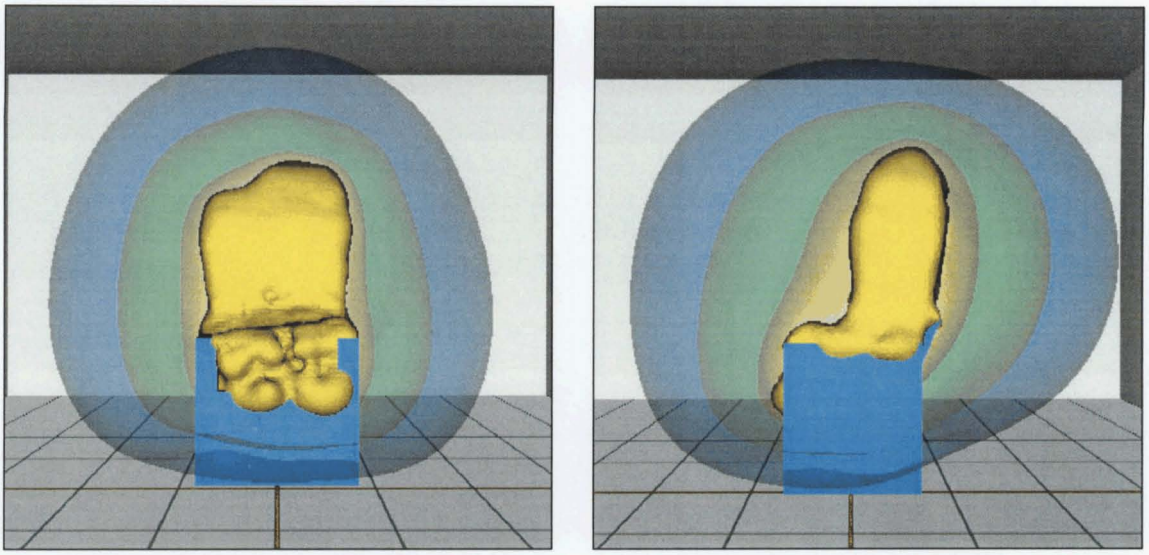

(a) Front view. (b) Side view.

Figure 5-21: 5, 10 and 20 kW/m^2 heat flux isosurfaces – 1 minute after ignition.

5.2.4.2 *Second Reconstruction – Two minutes after ignition*

The same procedure was followed for finding heat flux surfaces for the second reconstruction two minutes after ignition. Since the flame was larger, the boundaries of the point cloud surrounding the flame were extended to the values given in Table 5-7.

	Maximum	Minimum
x	3000	-3000
y	4000	-500
z	3000	-3000

Table 5-7: Bounds of the point cloud used to define the thermal radiation field.

In the first reconstruction 4,800 points filled a volume of 3m × 3.5m × 3m = 31.5m^3. To achieve the same density of points for this reconstruction, a volume of 6m × 4.5m × 6m = 162.0m^3 requires 162.0 × 4,800 / 31.5 = 24,685 ≅ 25,000. Therefore 25,000 points were randomly generated in this space and maximum shape factors were

calculated for each. The number of surface points added to the point cloud was increased to 2000 for this surface so that an RBF was fitted to the resulting cloud of 27,000 points.

Occlusion by the chair's frame was not accounted for as it was judged likely to introduce as many errors as it corrected. Calculations proceeded much quicker without using occlusion. For example, finding the maximum shape factor for 27,000 points without occlusion took approximately as long as finding the maximum shape factor for 6,000 points using occlusion. Computation time was about 24 hours in each case using a 807 MHz, x86 processor with 500 MB physical memory.

The heat release rate of this flame, two minutes after ignition, is greater than it was one minute after ignition. Therefore the isosurfaces chosen for extraction were different. The extracted surfaces corresponded to heat flux values of 20, 35 and 55 kW/m^2. These surfaces are shown in Figure 5-22.

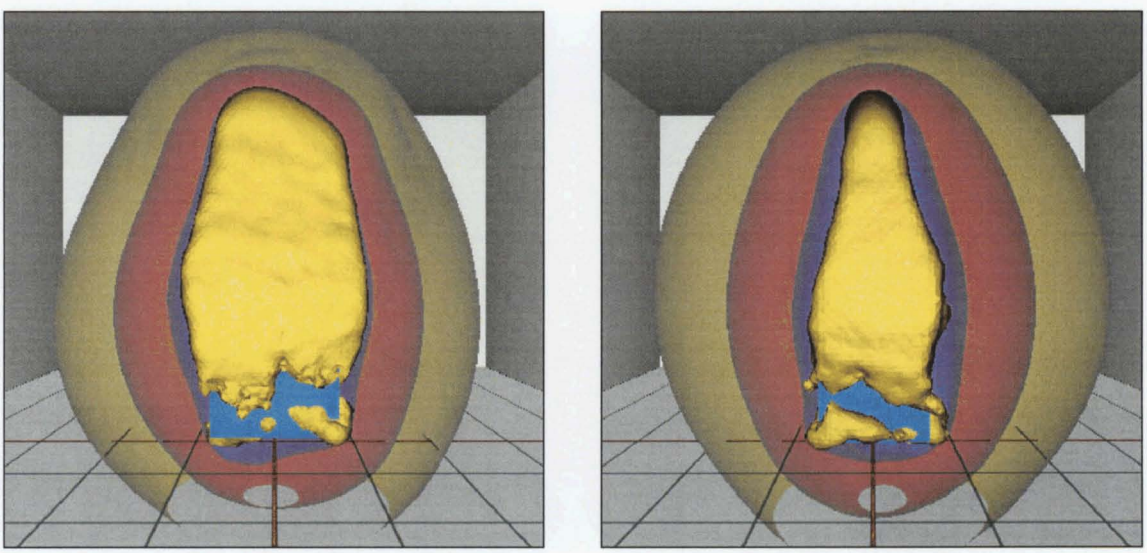

(a) Front view. (b) Side view.

Figure 5-22: 20, 35 and 55 kW/m2 heat flux isosurfaces – 2 minutes after ignition.

5.3 Discussion

5.3.1 Advantage of using RBFs to define surfaces

When some object obstructs the camera's view of the flame, as the frame of the chair's arm did in Figure 5-9b, the result can adversely affect the reconstruction. When Figure 5-9b is projected, the point cloud is "cut in two" as points with zero value are removed. The result is a discontinuity in the spatial data that marching cubes, for example, would represent as two distinct surfaces. However, an RBF can interpolate unsampled regions based on information contained in given data values. The result tends to minimise the effects of objects that occlude the flame. Notice in Figure 5-14b, how little the reconstructed surface has been affected by the projection of Figure 5-9b. This constitutes a significant advantage when reconstructing flames.

5.3.2 Maximum possible heat flux

If the shape factor F is set to 1 in equations (5-1) and (5-2), the maximum radiant heat flux from these fires becomes:

$$Q = 24.275 - 0.3682 = 23.91 \quad [\mathrm{kW/m^2}] \tag{5-5}$$

$$Q = 62.777 - 4.3912 = 58.39 \quad [\mathrm{kW/m^2}] \tag{5-6}$$

When comparing these results with that of section *4.3.1*, it is clear that none of these equations are transferable, and adds to the evidence for including emissivity into calculations.

5.3.3 Accurately Registering Projections

Reconstructions of the flame were visualized with a model of the chair to help provide a context. Figures 5-20 and 5-21 are two examples of this. Upon close inspection of some initial reconstructions, it was clear that the reconstructed flame was not exactly where it should be relative to the chair. One cause for this was that the model of the chair was constructed with planar surfaces and right angles, whereas the chair that was burnt had experienced some deformation. Other causes were due to inaccuracies in

specified coordinates for reference points and camera positions. Another potential error arises from deciding which part of the camera ought to be considered as the centre of projection. Care should be taken when recording this data to ensure inaccuracies are kept to a minimum. Since the cameras used in this experiment were not specifically designed and built for photogrammetry, errors due to the lens position and alignment should be expected [28].

5.3.4 Video Compression

Care should be taken when choosing video codecs. Frames extracted from a video that was compressed using Cinepak, yielded "blocky" images that were particularly noticeable after applying a threshold. As a result of this observation, all information was derived from frames of videos that were uncompressed, since any form of lossy compression discards valuable information.

5.3.5 Reducing Unwanted Objects during Thresholding

Unwanted artefacts appear largely due to two causes. First, there are objects that occlude the flame, such as measurement equipment and the frame of the burning furniture. Second, there are objects that are included by the threshold operation as part of the flame when they are not, such as the ceiling light present in the 219° views. Bright and/or reflective things cause most problems. Some surfaces and objects may benefit by being covered by dark, non-reflective screens or non-flammable drapes. Objects that are not essential to the experiment may be removed.

5.3.6 Synchronising Multiple Cameras

Recording a fire simultaneously with more than one camera requires some kind of synchronising strategy. Over the course of our experiments three synchronising strategies have been employed:

1. None – This is the case when one camera is used to record multiple views at different times as on July 29.

2. Approximate – Starting cameras from a verbal countdown or an occurrence, perhaps a hand signal, in the laboratory that is visible from both camera positions. This allows the cameras to be synchronised to within a second, which is acceptable when constructing averages from six seconds of video.

3. Frame accuracy – To synchronise cameras for the chair burn that features in this chapter, we used a photographic flash unit. Using cameras with a frame rate of one twenty-fifth (0.04) second and one thirtieth ($0.0\dot{3}$) second, with a flash unit set to one fiftieth (0.02) second, a single frame of each video could be illuminated. This allowed us to synchronise the two videos to at least one thirtieth of a second.

Chapter 6

Conclusions and Future Work

6.1 Conclusions

Two essential quantities must be specified in order to determine heat flux; they are the emissive power of the flame surface, and the shape factor between the flame and the target. The accuracy of heat flux predictions depends on the accuracy of these two constituents. To determine the shape factor it is necessary to define the geometry of the flame surface, and to have a method for obtaining the shape factor for that geometry.

This study provides a technique that can define multiple, irregular flame geometries. The technique involves image-processing videos of a fire recorded from different viewing positions. A 3D reconstruction of the flame is produced from which shape factor calculations are made using Hankinson's method. Then, based on estimates for the emissive power of the flame, heat flux values can be determined for any target location and orientation surrounding the flame. From this information is determined the thermal radiation field surrounding the flame, which can be used to decide whether or not an adjacent object is in danger.

The recorded heat flux data was graphed against calculated shape factors and the line of best fit was obtained. The slope of this line represents the emissive power of the flame, and values for Pearson's linear correlation coefficient were found to range between

0.955 and 0.998. This tells us that the shape factors are a very good predictor of heat flux. Since the shape factors were calculated from our definition of the flame geometry, the results suggest that our definition was also very good.

Usually the line of best fit, obtained by graphing recorded heat flux data against calculated shape factors, has the form $y = mx + c$. That is, there is a constant term c that shifts the line from the origin. The constant term is not apparent in the equation for heat flux, $Q = \varepsilon \sigma T^4 F$, and is peculiar to the empirical relationship between the recorded heat flux data against calculated shape factors. When attempting to predict heat flux by using an estimate of the emissive power $\varepsilon \sigma T^4$, rather than from a graph, the result will be of the form $y = mx$. This may not predict as well as an equation that includes an empirical constant (see Figure 4-18 and Table 4-5). This is an issue when extending the application of this work to real fires outside the laboratory, which is a focus for future work.

6.2 Future Work

This work becomes most useful to fire engineers when it can be taken out of the laboratory and applied to derive useful information from videos of real fires that have been recorded using unknown camera settings. To take the method out of the laboratory requires little or no dependence on a controlled environment or on data from other sources, such as heat flux gauges. Work should continue to improve heat flux predictions, although the objective should be to do this in less controlled situations. This is discussed further in section *6.2.1*. Improving heat flux predictions depends on improving the definition of the flame geometry and finding reliable ways to estimate the emissive power of the flame.

6.2.1 Image Processing as a Self-Contained Analysis Tool

In the laboratory one is able to control many aspects of the fire and arrange to collect all data required to achieve the objectives of the experiment. Therefore, if image processing the video cannot derive the required information, it can be acquired from other sources such as heat flux sensors, thermocouples, a furniture calorimeter, or geometric data obtained from measurements. The challenge, then, is to maximise the amount of reliable information that can be derived from video. One of the ways information can be derived from images is to make use of correlations that can be linked to image data. For example, the radiative fraction used in the Point Source model [41] is correlated to flame diameter, which can be estimated from calibrated images of the flame using equation (1-1).

6.2.2 Estimating Emissive Power

In section *2.1.3*, Shokri and Beyler [41] observed that the major uncertainty in their work was in the definition of the emissive power and not in the shape factor. They were modelling pool fires as a right circular cylinder. We have shown in section *5.2.3* that using our method for defining flame geometry significantly improves shape factor estimates so that emissive power is, now more than ever, a limiting factor when attempting to determine heat flux. Whatever method is used to estimate emissive

power, it will need to be based on empirical knowledge derived from experiments involving a range of different fuels (see section *1.2.2*).

One approach that might prove useful was employed in section *4.3.3*. In section *4.3.3* a value for the emissive power of the flame was obtained using an estimate for the radiative fraction from the Point Source model, the total energy output of the fire, and the surface area of the flame. This relation can be written:

$$E = \frac{\chi_r \cdot HRR}{A_{Surface}} \qquad [\mathrm{W/m^2}] \qquad (6\text{-}1)$$

Although the correlation for radiative fraction was based on data from pool fire experiments, and the equivalent diameter is meant for pool fires with a length to width ratio of approximately 1, the results looked promising (see Figure 4-20).

In the example of section *4.3.3*, the heat release rate of the flame was known since it had been set to 150 kW by the electronically regulated fuel supply. When the heat release rate (HRR) of a fire is not known it must be derived from the image data. One way to do this would be to find a correlation between the flame volume and the HRR. Then, using the volume obtained from the 3D flame reconstruction, the heat flux could be estimated.

Another method might be to estimate the effective flame temperature at the surface of the flame, and estimate emissivity from equation (4-8) based on some acceptable value for the total extinction coefficient that can be applied to a range of different fuels.

6.2.3 Camera Parameters

During reconstruction we assumed that the axes of the viewing coordinate system were orthogonal and the camera was located somewhere along the z-axis. This assumption allows certain errors to go unchecked. Since photogrammetric measurements are required, the camera should be calibrated by measuring the focal length, principal point position and lens distortion [30]. Here, the principal point is defined as "that point on

the image plane which is at the base of the perpendicular from the 'centre of the lens' or more correctly, from the rear nodal point" [28]. For most cameras, except those that have been specifically designed and built for photogrammetry, there is no requirement for the manufacturers to be meticulous regarding lens position and alignment [30]. Therefore, all cameras used for this work should be calibrated.

6.2.4 Finding the Camera Position

Our technique for defining flame geometry relies on establishing a coordinate system and using it to define camera positions and reference points. Measuring distances accurately with reference to some arbitrarily placed origin is difficult and can introduce errors that cause projections to be badly registered. Perhaps a better way would be to determine the camera position from reference points in the image rather than by measurement. A set of reference points, whose relative positions are precisely known, would be required in the vicinity of the flame. These points may be represented by some feature already present in the scene, or they could be introduced. At least three of these points would need to be clearly visible in each camera view. The problem of locating the camera is then similar to that of *tracking* in Augmented Reality (AR) applications. Some work would be required to investigate the accuracy of this method as it applies to flame reconstruction problems.

6.2.5 Recording the Video

Often in image processing applications, lighting issues confound the acquisition of consistent and accurate information. It is relatively easy to record a controlled flame since its location and size are constant, allowing the camera to be adjusted to give the preferred result. An uncontrolled flame, however, changes position and size during a burn, which can have significant effects on an image. Some investigation is required to determine whether it is better to allow the camera to automatically adjust the exposure, or to fix certain camera parameters such as aperture and shutter speed.

The advantage of fixing camera parameters is that every frame of the video is recorded in a consistent way. However, the increasing size of an uncontrolled flame can lead to overexposure, which can manifest as blooming.

Using a camera in automatic mode prevents overexposure but does not record image data in a consistent way. For example, when the flame occupies a small part of the image, and the exposure settings are based mainly on the intensity of the background, making the flame appear bright by comparison (see Figure 6-1a). At the peak of the fire the exposure settings are based mainly on the intensity of the flame, while lower intensities are no longer perceptible (see Figure 6-1b). This can cause problems when trying to ascertain the height of the flame, for example, since the flame tips have effectively disappeared. To be consistent, the same range of flame intensities should be recorded throughout the burn. A method is required that can achieve this and provide consistent results from a range of cameras.

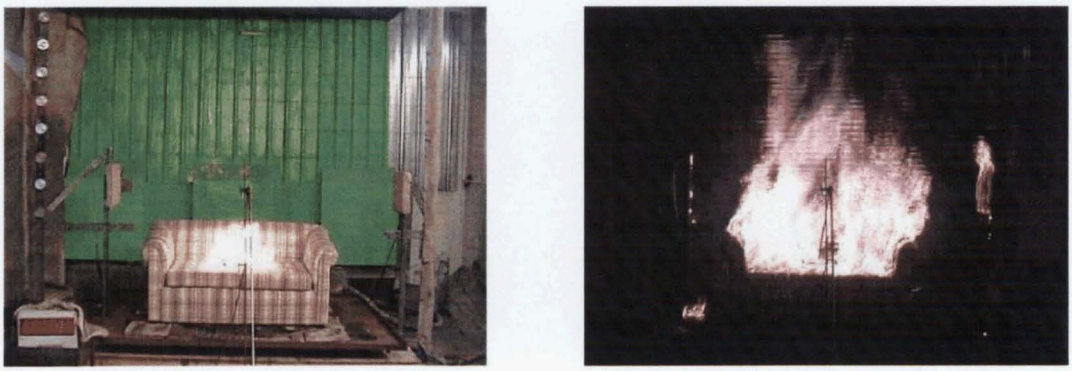

(a) Beginning of the fire. (b) Peak of fire.

Figure 6-1: Automatic exposure and its effects.

Acknowledgements

I have thoroughly enjoyed this work and attribute this largely to the excellent support given to me by all who have been involved in the project. Much of this credit goes to my supervisors, Dr. Alan McKinnon and Dr. Keith Unsworth. Their good judgement and good humour combined with their exceptional and wide-ranging skills have been invaluable and very much appreciated. I was very fortunate that my research coincided with a visit to Lincoln University by Fulbright Scholar, Professor Chris Rogers. In the six months he was here his remarkable enthusiasm and perception paved the way for the entire project. Our collaborators on this project were Dr. Charley Fleischmann and Michael Spearpoint of the Fire Engineering section at the University of Canterbury, Civil Engineering Department. Their generosity with laboratory facilities, expert advice, and good sense has been crucial to the work. Thanks also to the academic, technical and administrative staff, and to my fellow graduate students of the Applied Management and Computing Division at Lincoln University who happily lent assistance when it was required.

References

[1] Beale, J. (2002) TRV900 Light Intensity Transfer Function. Web site: http://www.bealecorner.com/trv900/tech/transfer.html

[2] Carr, J., Beatson, R., Cherrie, J., Mitchell, T., Fright, W., McCallum, B., and Evans, T. 2001. Reconstruction and Representation of 3D Objects with Radial Basis Functions. ACM SIGGRAPH 2001, Los Angeles, CA, pp67-76, 12-117 August 2001. Web site: http://aranz.com/download/modelling/papers/siggraph01.pdf

[3] FarField Technology (2002) FastRBF Toolbox, Command Line Interface.

[4] Fleischmann, C. (2002-2003) Personal Communication. Senior Lecturer in Fire Engineering, University of Canterbury.

[5] Foley, J. and Van Dam, A. (1982) Fundamentals of Interactive Computer Graphics. Addison-Wesley.

[6] Halliday, D., Resnick, R. and Walker, J. (1993) Fundamentals of Physics, Fourth Edition. John Wiley & Sons, Inc.

[7] Hankinson, G. (1986) Fire Safety Science: Proceedings of the First International Symposium . A Method for Calculating the Configuration Factor between a Flame and a Receiving Target for a Wide Range of Flame Geometries Relevant to Large Scale Fires. New York: Hemisphere Publishing Corporation. Grant, Cecile E. and Patrick J. Pagni, eds.

[8] Heskestad, G (1983) Luminous Heights of Turbulent Diffusion Flames. Fire Safety Journal, Vol. 5, pp103-108.

[9] Hottel, H. C. and Sarofim, A. F (1967). Radiative Transfer. McGraw-Hill, New York.

[10] Hottel, H. C.(1959) Certain Laws Governing Diffusive Burning of Liquids. Fire Res. Abstr. Rev. 1, pp.41-44.

[11] http://academic.mu.edu/phys/matthysd/web226/L0207.htm

[12] http://ees2.geo.rpi.edu/gis/lectures/week5_lecture.htm

[13] http://ironbark.bendigo.latrobe.edu.au/~fran/int32gp/wk09/lctr17.html

[14] http://www.aim-dtp.net/aim/calibration/introduction/introduction.htm

[15] http://www.alligatortech.com/DAA/filter_tutor.htm#Aliasing

[16] http://www.bealecorner.com/trv900/tech/transfer.html

[17] http://www.botzilla.com/photo/G1expose.html

[18] http://www.che.utah.edu/~wciro/my_research/framesets_poolfires/POOLFIRES.pdf

[19] http://www.computerworld.com/softwaretopics/software/multimedia/story/0,10801,62778,00.html

[20] http://www.damtp.cam.ac.uk/user/fdl/people/sd/digimage/document/cameras.htm

[21] http://www.doctorfire.com/flametmp.html

[22] http://www.dpreview.com/learn/Glossary/

[23] http://www.efunda.com/designstandards/sensors/methods/DSP_nyquist.cfm

[24] http://www.fire.org.nz/engineer/fe_buildings/design/design.htm

[25] http://www.inrialpes.fr/movi/people/Triggs/isprs96/isprs96.html

[26] http://www.interfire.org/features/tempertures_flames.htm

[27] http://www.mesa3d.org/

[28] http://www.optical-metrology-centre.com/Downloads/Papers/Photogrammetric%20Record%201998%20Principal%20Point.pdf

[29] http://www.ph.tn.tudelft.nl/Courses/FIP/noframes/fip.html

[30] http://www.racurs.ru/pdf/lite_e.pdf

[31] http://www.roperscientific.com/library.shtml
http://www.roperscientific.com/library_enc_dynamic.shtml

[32] http://www.roperscientific.de/CCD%20primer.html

[33] http://www.sensorsmag.com/articles/0199/flu0199/main.shtml

[34] Karlsson, B. and Quintiere, J. (2000) Enclosure Fire Dynamics. CRC Press.

[35] Markstein, G. H. (1976) Radiative Energy Transfer from Turbulent Diffusion Flames. Combustion and Flame, 27, pp. 51-63.

[36] McCaffrey, B. J. (1979) Purely Buoyant Diffusion Flames: Some Experimental Results. Gaithersburg MD, NBSIR.

[37] Mueller, K., Yagel, R. and Wheller, J. A Fast and Accurate Projection Algorithm for 3D Cone-Beam Reconstruction with the Algebraic Reconstruction Technique (ART). SPIE Medical Imaging Conference, San Diego, Feb. 21-27, 1998.

[38] Neider, J., Davis, T., Woo, M. (1993) OpenGL Programming Guide. Release 1, Silicon Graphics Inc.

[39] Rein, R. G. Jr., Sliepsevich, C. M. and Welker, J. R. (1970) Radiation View Factors for Tilted Cylinders. Fire and Flammability, Vol. 1.

[40] Rogers, C. (2002-2003) Personal Communication. Professor of Mechanical Engineering, Tufts University.

[41] SFPE Task Group on Engineering Practices (1999) Assessing Flame Radiation to External Targets from Pool Fires. Society of Fire Protection Engineers.

[42] Siegel, Robert and Howell, John R. (1981) Thermal Radiation Heat Transfer, Second Edition. Hemisphere Publishing Corporation, USA.

[43] Wong, C. R. (2001) Contribution of Upholstered Furniture to Residential Fire Fatalities in New Zealand. School of Engineering, University of Canterbury.

[44] Thomas, P. H. (1963) The Size of Flames from Natural Fires, The Ninth Symposium (International) on Combustion. The Combustion Institute, Pittsburgh, Pennsylvania 844:859.

Appendix A

VRML File Format

Enhancing the VRML output of FastRBF Toolbox

The VRML file exported from fastrbf is very basic. It contains the geometry and a viewpoint but no background or appearance information. Adding a few extra lines of code can enhance the visualisation.

An example of the difference is shown in Figure A-1.

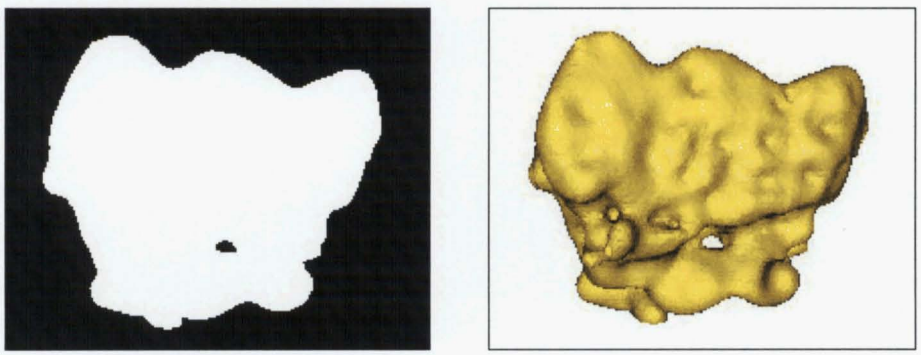

(a) Raw VRML output (b) VRML output modified

Figure A-1: Adding code to gain more from the VRML output.

The relevant sections of code for these examples are listed in Figure A-2 so that the modifications are clearly visible. Note that any text following the hash symbol, #, is ignored as a comment.

```
#VRML V2.0 utf8
Background {
  skyColor [1 1 1 ] # white
  skyAngle [1.309, 1.571 ]
  groundColor [1 1 1 ]   # white
  groundAngle [1.309, 1.571 ]
  }
Viewpoint {
  orientation 0 0 1 0
  position 88 342 5000
  description "default"
}
Shape {
  Appearance Appearance {
    material
      DEF MatWnd Material {
      DiffuseColor 1.0 0.8 0
#     transparency 0.6
       }
    }
    geometry IndexedFaceSet {
    #
    # 14251 points:
    #
      coord Coordinate {
      point [
        911.497 607.365 -169.929,
          :
```

Figure A-2: Enhancing VRML code output by FastRBF.

Appendix B

Estimating Temperature from Probability using McCaffrey's Plume Equation

McCaffrey's Work

Dr McCaffrey made extensive measurements of temperatures in turbulent diffusion flames. He divided the fire plume into three regions [26]:

1. A continuous flame region, which begins slightly above the base of the flame and has a constant temperature slightly below 900°C.
2. An intermittent flame region, which is above the solid flame region and has continuously decreasing temperatures as one moves up the plume. The visible flame tips correspond to a temperature of about 320°C.
3. A thermal plume region, which is beyond the visible flame tips and has temperature dropping continually with increasing height.

Using experimental data and dimensional analysis McCaffrey arrived at an equation for the centreline plume temperature rise:

$$\Delta T_0 = \left(\frac{\kappa}{0.9 \cdot \sqrt{2g}} \right)^2 \left(\frac{z}{\dot{Q}^{2/5}} \right)^{2\eta-1} \cdot T_\infty , \qquad \text{(B-1)}$$

where

κ and η vary depending on the three regions (see Table B-1)

g is 9.81 (ms^{-2})

z is the height (m) above the base of the flame

$\dot{Q}$ is the total energy release rate [kW]

T_∞ is 293°K

Region	**$z/Q^{2/5}$ $m/kW^{2/5}$**	η	κ
Continuous	<0.08	½	6.8 $m^{1/2}/s$
Intermittent	0.08–0.2	0	1.9 $m/(kW^{1/5}s)$
Plume	>0.2	-1/3	1.1 $m^{4/4}/(kW^{1/3}s)$

Table B-1: The constants in McCaffrey's Plume Equations

The burner was 300mm square and sat 750mm above the floor under a passive hood in a large laboratory [36]. Although McCaffrey used natural gas (methane) and we used propane, it assumed that plume properties are independent of fuel and only dependent on energy release rate, $\dot{Q}$ [34].

Correlating centreline probabilities with temperature

Experiment

The goal is to relate probability to height, along the centerline of the plume, so it can then be related to temperature using McCaffrey's equation. An experiment was conducted using a 300mm square burner (as McCaffrey did) under a passive hood in the laboratory. The top of our burner was 300mm above the floor. A frame from the video of the 150kW frame appears in Figure B-1. Two minutes of video was recorded for

both a 100kW flame and a 150kW flame. Since a generally applicable result is required data was taken from four averaged images. Each average was produced from six seconds of video. Two averages were taken from the video of the 100kW flame, and two from the 150kW flame. The averages were extracted from different periods of each video.

Figure B-1: 150kW flame used in determining centreline probabilities.

Analysis

Each of the averaged images requires calibration. Videos of both the 100kW and the 150kW flame were recorded from the same camera position, so calibration is the same for all images. To calibrate an image, it was loaded into Microsoft Paint and zoomed to Large Size. At the base of the flame the Select tool was used to drag a line from one side of the front of the burner to the other (see Figure B-2). When doing this, the coordinates where the Select tool was initially clicked appear in the Status bar. To the right of these coordinates is shown another set of numbers indicating the extent of the rectangle dragged out by the Select tool. The horizontal distance was 67 pixels, which corresponds to 300mm in real world units. Therefore, one pixel is equivalent to $0.3\text{m}/67 = 0.004478\text{m}$. Since the pixels are assumed to be square, this is also the

vertical calibration. Although the burner cannot be seen in the averaged image, the base of the flame clearly indicates its extent (as Figure B-1 shows).

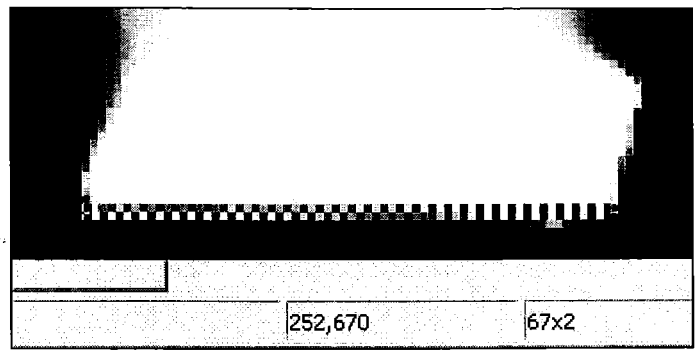

Figure B-2: Calibrating the averaged images.

The centre of the base of the flame is also required and is determined in a similar way (see Figure B-3).

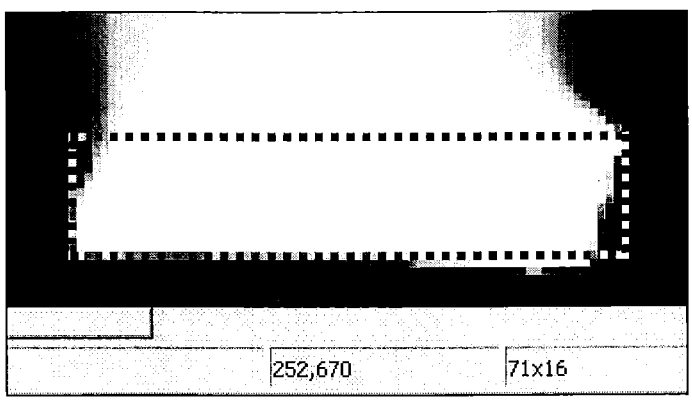

Figure B-3: Establish the centre of the base of the flame.

In this case the rectangle is dragged from one corner of the diffusion burner to the corner that is diagonally opposite. The extent of the rectangle is shown to be 71×16. The centre of the base of the flame is at the intersection of the diagonals of this rectangle, and has coordinates given by:

$$(252 + 7\tfrac{1}{2}, 670 - 1\tfrac{1}{2}) \approx (288, 662) \qquad \text{(B-2)}$$

Therefore the centreline of the plume begins at image coordinates $(288, 662)$ and extends vertically upwards, with each pixel equivalent to 4.478mm (see Figure B-4). To obtain more reliable data, the probabilities are taken to be the average of pixels on the centreline and those from columns on either side. The centreline is column 288 so, for each row, columns 287 to 289 are averaged before finding the probability. For example, Table B-2 gives the centreline data for rows 439 to 443, together with adjacent pixels.

	Col. 287	**Col. 288 Centreline**	**Col. 289**	**Probability**	**Height (m)**	**McCaffrey's Temperature**
Row 439	182	185	188	0.725490	0.9986	651.27°C
Row 440	189	186	188	0.735948	0.9941	656.02°C
Row 441	189	188	188	0.738562	0.9896	660.82°C
Row 442	192	194	188	0.750327	0.9852	665.68°C
Row 443	194	194	194	0.760784	0.9807	670.60°C

Table B-2: Sample data with probabilities, height and temperature.

As a sample calculation, consider the probability for pixel row 440:

$$\text{Probability} = \left(\frac{189+186+188}{3}\right) \div 255 = 0.7359 \qquad \text{(B-3)}$$

The height is determined from the pixels' row number, and the row number of the centre of the base of the flame. Using row 440 again as an example:

$$\text{Height} \qquad (662-440)\times 0.004478 = 0.9941\text{m} \qquad \text{(B-4)}$$

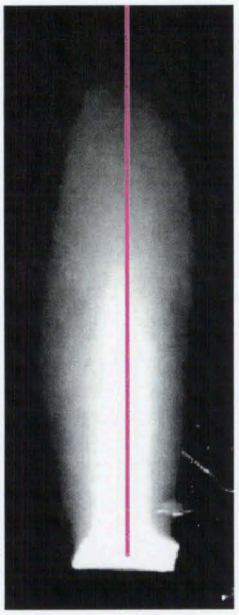

Figure B-4: Centreline.

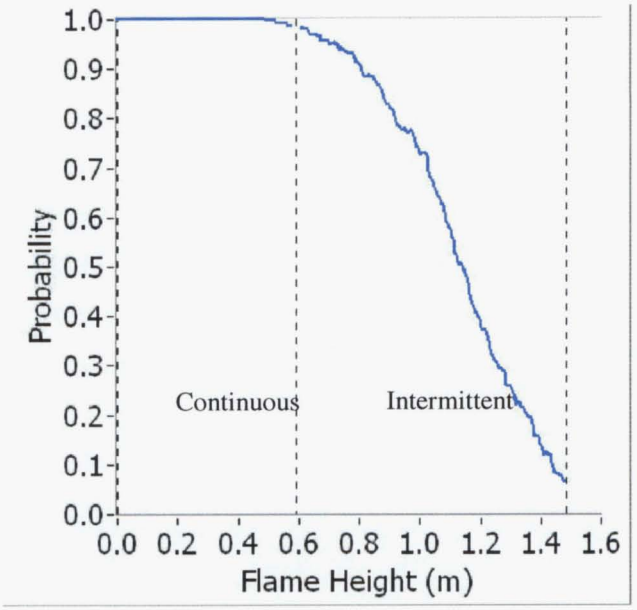

Figure B-5: Probabilities along the centreline.

Since the link between probabilities and temperature is height, McCaffrey's equation must be evaluated for the heights that have been determined for each pixel row. For example, consider row 440:

The first step is to determine which region of the flame this height corresponds to.

$$\text{Height } z = 0.9941 \quad \Rightarrow \quad {}^{0.9941}\!/_{150^{0.4}} = 0.1340 \tag{B-5}$$

0.1340 is greater than 0.08 and less than 0.2, so this is the intermittent region of the flame where $\eta = -1/3$ and $\kappa = 1.1$.Now using (B.1):

$$\Delta T_0 = \left(\frac{1.1}{0.9 \cdot \sqrt{2 \cdot 9.81}} \right)^2 (0.133966)^{2\cdot(-1/3)-1} \cdot 293 = 636.02^{\circ}C \tag{B-6}$$

That is, an actual temperature of 656.02°C, or 929.02°K.

Figure B-6 graphs McCaffrey's predictions for a 150kW flame to a height of 2 metres.

Figure B-7 shows the boundaries of McCaffrey's regions added to a picture of the laboratory that includes an image of the 150kW flame. The flame image is a six second average that has been modified so that probabilities greater than 98% are white,

probabilities between 4% and 98% are grey, and probabilities less than 4% have been discarded.

The graph in Figure B-6 shows the heights that bound McCaffrey's regions. The continuous region begins at height zero, which corresponds to a y-value (row) in the image of 662. The transition between the continuous region and the intermittent region occurs at height 0.595m. Using image calibration information established earlier, we could determine the corresponding y-value: $662 - 0.595/0.004478 \approx 662 - 133 = 529$. Similarly, the transition between the intermittent region and the plume occurs at height 1.485m, which corresponds to an image y-value of 330.

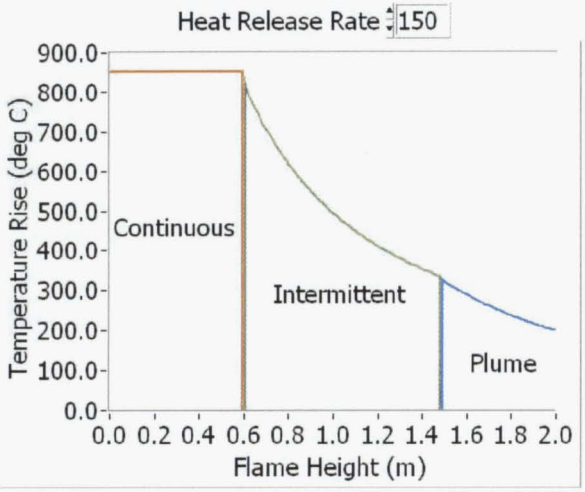

Figure B-6: McCaffrey's predictions.

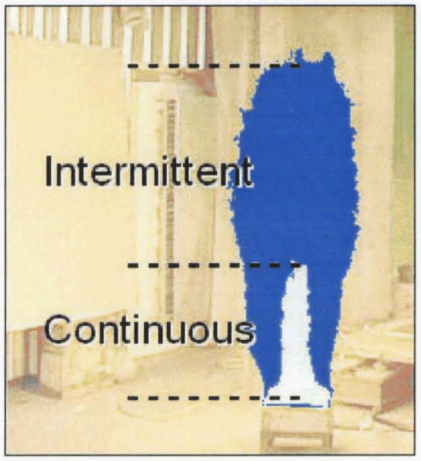

Figure B-7: McCaffrey's regions.

The data from the centrelines of the four averaged images, two from the 100kW flame and two from the 150kW flame, are graphed in Figure B-8. Although the 100kW flame data is blue and the 150kW data is green, the 5th order polynomial shown in red has been fitted to both data sets. The two data sets were coloured differently to because it is interesting to note that the fitted polynomial overestimates the temperature for the larger flame, and underestimates for the smaller flame. Note that this equation applies to the intermittent region only. The equation for the polynomial that gives temperature as a function of probability is:

$$T(p) = 6140.8p^5 - 12938p^4 + 9724.2p^3 - 2990.1p^2 + 584.51p + 327.43 \qquad \text{(B-7)}$$

The temperature rise given by McCaffrey's equation for the 100% flame region is 852.5°C. Since the continuous region of the flame extends for over half a metre, there were many data points with values (1.0m, 852.5°C). After considering whether or not to remove the 408 duplicate data points, they were retained because their presence almost forces the fitted polynomial to interpolate the point (1.0m, 852.5°C). For example, consider T(1.0):

$$T(1.0) = 6140.8 - 12938 + 9724.2 - 2990.1 + 584.51 + 327.43 = 848.84^{\circ}C \qquad \text{(B-8)}$$

This equation gives a temperature rise at probability $p = 0$ of T(0) = 327.43°C. This corresponds to an actual temperature of 347°C at the flame tips and is very similar to results obtained by McCaffrey, Cox and Chitty, and Yuan and Cox who all estimated this temperature to be about 340°C [26].

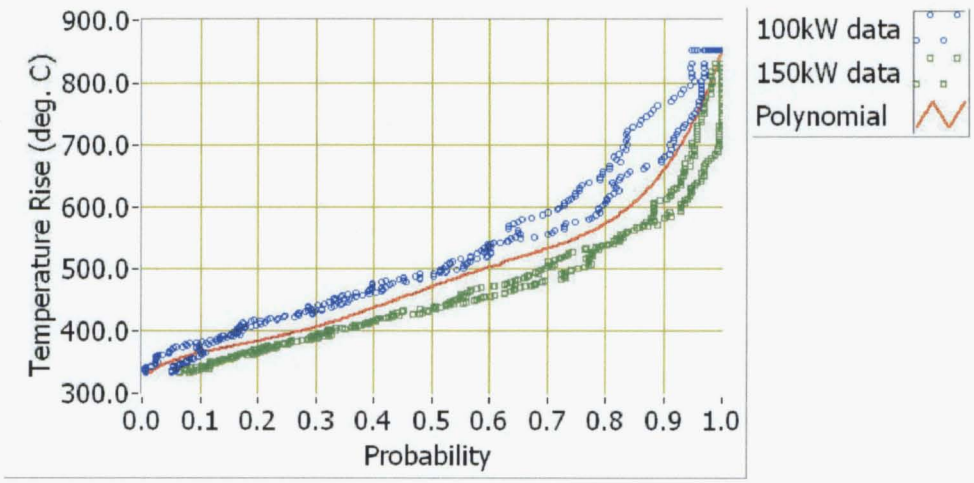

Figure B-8: McCaffrey's temperature predictions vs. probability.

Appendix C

Experimental Data

Controlled flame (Diffusion burner)

The heat source was a propane diffusion burner with dimensions 600mm × 300mm. The supply of fuel was electronically regulated to produce a constant heat release rate of 150kW. See section *4.1.3.1 Gauge Positions* for a description of experiment's layout.

Direction	Gauge Pos.	Heat Flux	Shape Factor
North - 0°	1	7.65	0.3234
	2	4.18	0.1440
	3	2.45	0.0795
	4	1.61	0.0503
	5	6.75	0.2589
	6	4.26	0.1370
	7	2.79	0.0809
	8	1.88	0.0523
	9	4.06	0.1521
	10	3.10	0.1009
	11	1.95	0.0680
	12	1.34	0.0475
	13	2.71	0.0771
	14	2.57	0.0650
	15	1.89	0.0508
	16	1.43	0.0390

Direction	Gauge Pos.	Heat Flux	Shape Factor
NNE – 22.5°	1	9.00	0.3549
	2	4.48	0.1656
	3	2.32	0.0951
	4	1.47	0.0616
	5	7.94	0.2865
	6	4.70	0.1527
	7	2.72	0.0933
	8	1.80	0.0618
	9	4.32	0.1627
	10	2.96	0.1094
	11	2.10	0.0760
	12	1.47	0.0543
	13	3.04	0.0781
	14	2.46	0.0679
	15	1.97	0.0547
	16	1.52	0.0431
NE - 45°	1	8.35	0.3895
	2	4.01	0.1924
	3	2.31	0.1116
	4	1.39	0.0721
	5	7.12	0.3216
	6	4.12	0.1783
	7	2.66	0.1086
	8	1.73	0.0716
	9	4.17	0.1811
	10	2.98	0.1253
	11	2.15	0.0869
	12	1.41	0.0619
	13	2.90	0.0813
	14	2.42	0.0745
	15	2.02	0.0609
	16	1.54	0.0482
East - 90°	1	8.86	0.4835
	2	4.58	0.2167
	3	2.94	0.1167
	4	1.91	0.0719
	5	6.97	0.4173
	6	4.28	0.1943
	7	2.90	0.1091
	8	1.91	0.0690
	9	5.60	0.1939
	10	3.80	0.1250
	11	2.50	0.0831
	12	1.74	0.0578
	13	3.15	0.0755
	14	2.69	0.0697
	15	1.94	0.0565
	16	1.49	0.0443

Direction	Gauge Pos.	Heat Flux	Shape Factor
ESE – 112.5°	1	9.98	0.4605
	2	5.01	0.2140
	3	3.01	0.1205
	4	2.00	0.0763
	5	8.50	0.4088
	6	4.71	0.1957
	7	2.88	0.1147
	8	1.98	0.0742
	9	5.10	0.1894
	10	3.61	0.1272
	11	2.53	0.0875
	12	1.85	0.0620
	13	3.06	0.0724
	14	2.55	0.0696
	15	2.01	0.0582
	16	1.58	0.0465
SE - 135°	1	9.30	0.4473
	2	4.89	0.2152
	3	3.00	0.1213
	4	1.91	0.0768
	5	7.68	0.3976
	6	4.65	0.2004
	7	2.89	0.1170
	8	1.89	0.0754
	9	4.67	0.2014
	10	3.34	0.1327
	11	2.52	0.0901
	12	1.71	0.0634
	13	2.67	0.0730
	14	2.30	0.0714
	15	1.96	0.0597
	16	1.40	0.0476

Uncontrolled flame (Upholstered chair)

Time after ignition	Gauge Pos.	Heat Flux	Shape Factor
1 minute	1	11.76	0.4883
	2	7.74	0.3369
	3	2.95	0.1522
	4	1.23	0.0531
	5	7.90	0.3429
	6	13.17	0.5618
2 minutes	1	55.47	0.8751
	2	37.17	0.6799
	3	15.64	0.3485
	4	6.35	0.1285
	5	32.63	0.7469
	6	50.28	0.7873

Appendix D

Using the FastRBF Toolbox

ARANZ file format

The point cloud data must be converted to the ARANZ file format for processing by the FastRBF Toolbox. An ARANZ file begins with the header `%ARANZ-1.0`, where the two numbers are the major and minor versions of the ARANZ format. The rest of the file is in sections identified by a string in the form [*section-name*]. Appearing in this order the sections are:

- [comment] – optional,
- [index] – describes the data stored in the file. Each line of description has an *Identifier* that may begin with a letter or underscore, a *Type* (Integer, Double, Boolean or Character), and *Array Sizes* (columns and rows).
- [ascii] or [binary] – to indicate whether the data is in text or binary form.

```
%ARANZ-1.0

[comment]
100kW diffusion burner - July 29, 2002.

[index]
Location Double 3 2841;
Value Double 2841;

[ascii]
-6.786474E+1      1.180351E+2 4.061986E+2
2.499602E+2 9.291600E+1 -2.974246E+2
6.594329E+2 4.762531E+1 5.283364E+2

      :

4.677234E+2 4.976273E+2 1.741028E+2
3.882353E-1
1.176471E-2
9.921569E-1
```

Figure D-1: Example of ARANZ file format.

In the example file of Figure D-1, there are 2841 points in the cloud. First, the *Location* of each point is given. In accordance with the index description, each location appears as three (x, y and z) double type values written in decimal scientific notation. Following the location of every point is the *Value* associated with each point. The data arrays for each item need not be formatted like this example. They can be flattened, concatenated and written to the file as elements separated by white space (normally a line feed).

Remove (near) identical points

It is a good idea to filter the point cloud with the *unique* function. This removes any coincident points. This is wise because the RBF fitter cannot handle points that are identical, or very nearly identical (relative to the scale of the data). In the process, the ascii `.txt` file is converted into a binary `.p3d` file.

- **`fastrbf unique flame.txt flame.p3d`**

Fitting an RBF

Given a set of N points x_i and values f_i, the process of finding an interpolating RBF, s, such that $s(x_i) = f_i$, $i = 1, 2, \ldots, N$ is called *fitting*. The library employs fast approximation methods to fit RBF's so absolute equality is never achieved. Here is an example of the command line to fit an RBF

- **`fastrbf fit -accuracy=0.05 -errorbar flame.p3d flame.rbf`**

The *fitting accuracy* is the maximum absolute error between a data point's value and the fitted RBF evaluated at that point. It is written:

$$\max_{i=1,\ldots,N} |s(x_i) - f_i| \tag{D-1}$$

There is bound to be some component of 'noise' inherent in the point cloud. The magnitude or frequency of this noise is not known, although it is assumed to be of higher frequency than the essential flame shape that we wish to characterize. Smoothing can be introduced at the fitting stage by not forcing the RBF to approximate the noisy raw data too closely. This can be achieved by judicious choice of the *-accuracy* argument. This type of smoothing is referred to as *smoothest restricted range approximation*. This method assumes the existence of a range of values at each data point within which the true function lies. The range of values is analogous to the error bars associated with experimental data. The RBF fitted is then the smoothest that lies within the specified tolerance at each data point. With RBF values in the range [0, 1] and an accuracy argument of 0.05, the 'error bars' at each data point are ±5%.

Evaluating an RBF

An RBF is also evaluated using fast approximation methods so the true RBF value is not achieved. If the values a_i approximate those of the RBF at the points x_i, then the evaluation accuracy is

$$\max_{i=1,\ldots,N} |s(x_i) - a_i| \qquad \text{(D-2)}$$

The default evaluation accuracy is 100^{th} the fitting accuracy. If this is not satisfactory the user can set it explicitly using the *–accuracy* argument.

- **`fastrbf isosurf -resolution=10 -threshold=0.75 -normals flame.rbf flame75.msh`**

When the threshold level is set at 0.75, the extracted surface can be defined as the set of all points x_i in 3D space where $s(x_i) = 0.75$. This infinite set of points is sampled at intervals determined by the *–resolution* parameter. This parameter can be used to control the relative size and number of triangles in the extracted surface. Increasing the resolution decreases the number of triangles and increases their size. However, care should be taken that coarse mesh resolutions do not produce aliasing in the surface.

Exporting as VRML

To view the extracted isosurface, it can be exported as a variety of file formats including a VRML 2.0 file. VRML is a standardized format to exchange 3D data over the web and is widely supported, so for this reason it is recommended. Some sort of Web3D viewer is required such as Cortona VRML Client by Parallel Graphics. Cortona works as a VRML plug-in for popular Interenet browsers (Internet Explorer and Netscape Navigator)[6] and office applications (Microsoft Powerpoint, Microsoft Word, etc). If the point coordinates and the indices, which link the points to define triangles, are required for another application they can be easily filtered from the VRML text file, although the Wavefront Object (.OBJ) file may be easier for this. Here is an example of the export command.

- **`fastrbf export -vrml flame75.msh flame75.wrl`**

[6] It is also available for Mac and Mac OS X.

Appendix E

Gardon Heat Flux Gauges

Gardon heat flux gauges are cylinder type gauges and comprise a pair of thermocouples in which the elements are separated by a thin layer of thermal resistance material (see Figure E-1). Under a temperature gradient, the two thermocouples will be at different temperatures. The differential temperature between the top and bottom of the resistance layer produces a differential voltage, which is proportional to the heat flux through the material. This differential voltage, in millivolts (mV), is the quantity recorded in our experiments.

As previously noted, if there is no thermal gradient across a gauge, no heat flux will be measured. This is especially important in long-duration tests in which a gauge may heat up to a uniform temperature and needs to be actively cooled. For this reason we water-cooled the gauges taking care to shield the copper tubing, that carries the water, from the flame.

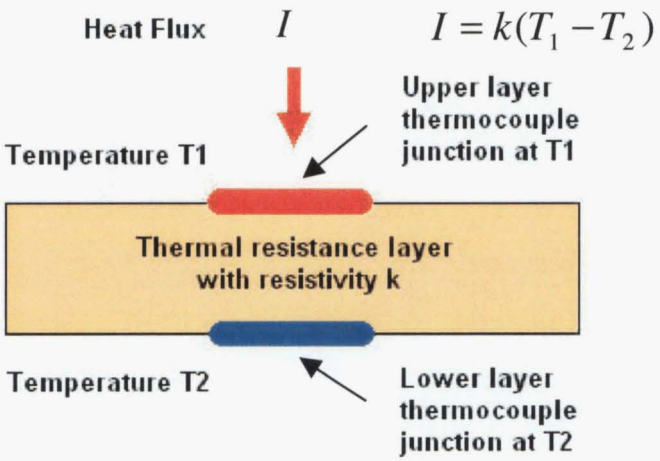

Figure E-1: Heat flux gauge.

Appendix F

Visualisation Issues

During this work, visualisations have been produced using VRML and by calling the OSMesa graphics library directly from LabVIEW.

The FastRBF Toolbox can export files in VRML 2.0 format. These text files can be used to take a quick look at the results (see Appendix A), or they can be further embellished with colour, lighting, scene geometry, and text labels to obtain a more complete visualisation as in Figure 5-23. VRML files can be viewed using a browser such as Netscape or Internet Explorer, and a plug-in viewer such as *Cortona VRML Client* or *Cosmo Player*. Both of these VRML viewers provide the option of choosing a renderer. For this study the OpenGL renderer was used because it appeared to be better than DirectX and at least as good as the R98 renderer.

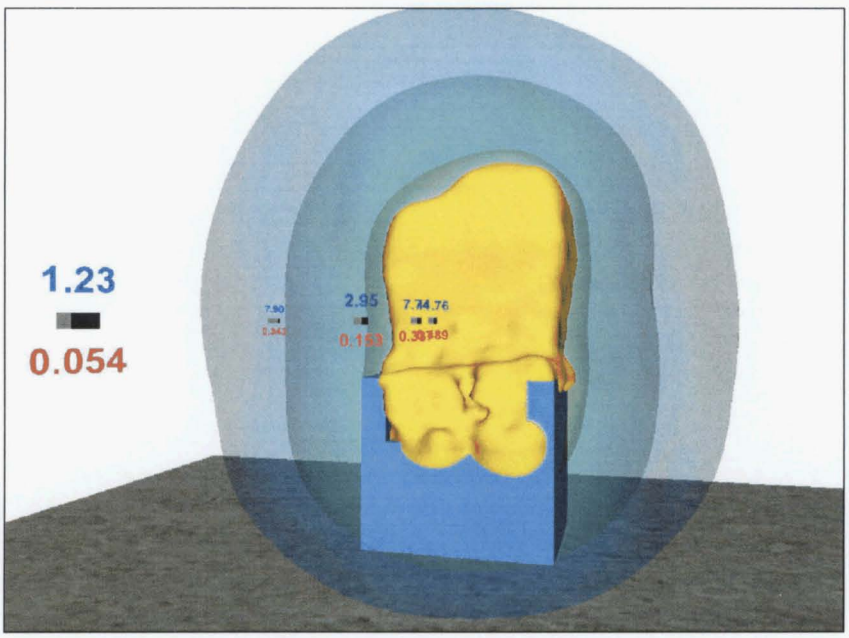

Figure F-1: A VRML visualisation.

However, calling a graphics library directly from LabVIEW produced most of the pictures in this document. The library used is a special off-screen rendering interface called OSMesa. It is unique in that it has no dependencies on any operating system or window system [27]. Mesa is a 3D graphics library with an API that is very similar to that of OpenGL and utilises the OpenGL command syntax or state machine. OSMesa allows 3D images to be rendered into a user-allocated block of memory rather than an on-screen window. Apart from being portable, another advantage with using OSMesa is that the block of memory can be linked to a LabVIEW *picture*. This enables the image to be embedded in a LabVIEW front panel (see Figure 5-24) rather than appearing in a separate window.

Another advantage with using OSmesa is that the image contained in the block of memory can be obtained, using *glReadPixels* with the *GL_RGB* format, and then written to disk in a variety of formats including BMP and JPG. As images are rendered and obtained with this technique, they may be used to build movies. While not allowing interaction, movies offer a visualisation that overcomes most performance issues while also being portable, since they do not require installing LabVIEW, the OSMesa library, or any other associated components.

A significant disadvantage is, however, that OSMesa does not use a graphics card during rendering, which leaves the CPU to handle the task. Consequently, frame rates are low particularly when, for example, multiple surfaces with transparency might involve more than 100,000 triangles in a scene. The visualisation appearing in Figure 5-24 shows a point cloud after minima reconstruction has been completed. This represents the points with opacity proportional to the probability of the flame being at that location. The result is effective because the outer points having lower probability are more transparent and do not obstruct a view of the interior of the cloud. Unfortunately, this is only possible if each point is a separate OpenGL model, which is an inefficient arrangement that further slows things down.

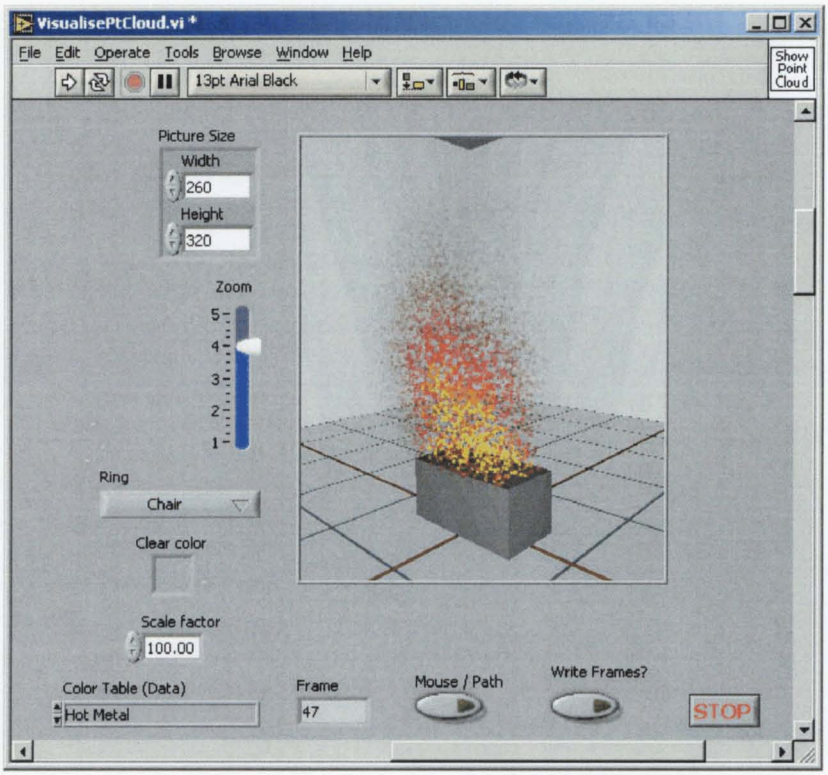

Figure F-2: OSMesa allows rendering to be embedded in a LabVIEW Panel.